NASA Contractor Report 3470

Helicopter Rotor Trailing Edge Noise

Robert H. Schlinker and Roy K. Amiet
United Technologies Research Center
East Hartford, Connecticut

Prepared for
Langley Research Center
under Contract NAS1-15730

National Aeronautics
and Space Administration

**Scientific and Technical
Information Branch**

1981

TABLE OF CONTENTS

TABLE OF CONTENTS (Cont'd)

SUMMARY

An experimental and analytical study was conducted to assess the importance of trailing edge noise as a helicopter rotor broadband noise source. As part of this objective, it was desired to develop a generalized noise prediction in which the helicopter operating conditions, rotor geometry, and rotor boundary layer details were specified.

Since existing full-scale rotor data are contaminated with many operative helicopter noise mechanisms, assessing the importance of trailing edge noise required conducting an experiment in which the mechanism could be isolated. This resulted in a two phase study in which the first objective was to investigate the noise from an isolated two-dimensional airfoil in an acoustic wind tunnel with a low turbulence level. The experiment was conducted at close to full-scale helicopter rotor Reynolds numbers using a main rotor blade section to ensure that the airfoil turbulent boundary layer characteristics simulated realistic operating conditions. Both boundary layer data and acoustic data were obtained for use in developing a scaling law for trailing edge noise predictions. The experiment also provided a test case for a first principles trailing edge noise theory developed as part of the study.

Results obtained from the isolated airfoil study were extended to the rotating frame coordinate system to develop a helicopter rotor trailing edge noise prediction. The prediction procedure was tested against selected full-scale helicopter data. Comparisons of the calculated sound pressure levels with the experimental data provided as assessment of the trailing edge noise contribution to the total helicopter noise spectrum.

Conclusions resulting from this study can be grouped into two categories. In the case of full-scale rotor noise, it was demonstrated that trailing edge noise contributes significantly to the total helicopter noise spectrum at high frequencies. This noise mechanism is expected to control the minimum rotor noise level. A knowledge of the helicopter altitude, speed, angular position, rotor tip speed, blade number, rotor chord and span, and local boundary layer thickness are sufficient to predict the rotor trailing edge noise contribution.

In the case of noise radiation from a local blade segment the acoustic directivity pattern is predicted by the first principles trailing edge noise theory. Noise dependence on local section Mach number varies as Mach number to the fifth power in agreement with the scaling law and the fundamental theory. Finally, acoustic spectra from a local blade segment can be predicted using a scaling law which includes the Mach number, boundary layer thickness, and observer position. Spectrum shape and sound pressure level are also predicted by the first principles theory but the analysis does not predict the Strouhal value identifying the spectrum peak. Accurate predictions require using measured surface pressure data obtained near the airfoil trailing edge.

INTRODUCTION

Background

The noise level at a given angle relative to a helicopter and within a specified frequency band represents the sum of contributions of a number of separate noise mechanisms. The relative importance of these mechanisms depends upon the rotor geometry, aerodynamic characteristics (e.g., tip speed, blade pitch), and operating mode of the helicopter (hover, forward flight, vertical ascent or descent). Some of the mechanisms apply primarily to the main rotor, some apply to both the main rotor and the tail rotor, and in the more complex situation, interactions occur linking the wakes of one rotor blade with noise generation by another blade. The simultaneous occurrence of the different mechanisms has always complicated both data interpretation and attempts to assess the accuracy of theory developed to treat each mechanism.

The list of possible rotor noise mechanisms is lengthy and is often debated among specialists in helicopter noise research. George (ref. 1) provided a comprehensive list of helicopter noise mechanisms. The list can be subdivided into periodic and random noise sources both of which are important over the range of helicopter operating conditions. In the absence of impulsive noise (ref. 2), George notes that random (or broadband) noise can be the primary noise source. For the case of hover, Munch et al. (ref. 3) demonstrated using a 2 Hz bandwidth frequency analysis, that broadband noise was the prime contributor to PNL for five different rotor systems over a wide range of thrust parameters (thrust coefficient divided by solidity). Study of helicopter rotor broadband noise is, therefore, relevant.

One of the sources of helicopter rotor broadband noise is the rotor turbulent boundary layer, in particular, its interaction with the blade trailing edge. Although there is little dispute that this is an operative mechanism in the case of airframe noise, questions exist as to its spectrum shape and absolute level on helicopter main and tail rotors. Unfortunately, full-scale helicopter rotor data contains other broadband noise sources making it difficult to assess the importance of trailing edge noise. The additional mechanisms include incident turbulence, stalled airfoil noise, and engine noise. The objective of the present study was, therefore, to isolate the trailing edge noise mechanism and obtain a quantitative understanding of this noise source as a function of the relevant parameters.

Previous Investigations

Experimental Studies - Direct experimental studies of helicopter rotor trailing edge noise are presently not available. Previous research on this noise mechanism was limited to low Mach number two-dimensional isolated airfoil tests, full-scale airframe tests, and blown flap noise studies. Although these studies did not simulate helicopter rotor operating conditions, they are applicable to understanding the trailing edge noise mechanism.

Previous attempts, such as that of Paterson et al. (ref. 4) to measure trailing edge noise from a NACA 0012 two-dimensional isolated airfoil were unsuccessful. The airfoil, which was tested in the UTRC open jet acoustic wind tunnel, could not be detected above the facility background noise. To overcome the background noise sources Schlinker (ref. 5) employed a directional microphone system to detect the airfoil. Measurements demonstrated that the trailing edge was the dominant source region for airfoil self noise generation. Spectrum peak amplitudes were found to vary with approximately a fifth power velocity scaling. Comparisons of the measured spectra showed reasonable agreement with an existing scaling law prediction developed by Fink (refs. 6 and 7) for airframe trailing edge noise.

Heller and Dobrzynski (ref. 8) circumvented the background noise problem by using an aerodynamically clean glider to experimentally investigate trailing edge noise. Measured far field acoustic spectra peaked near a Strouhal number of 0.02 with the length scale based boundary layer displacement thickness. Predictions of the radiated noise from the measured surface pressure characteristics were found to be satisfactory.

Yu and Joshi (ref. 9) reported the results of a study using space-time correlations to extract isolated airfoil turbulent boundary layer noise spectra from facility background noise. The coherent part of the broadband noise generation was found to be localized at the airfoil trailing edge in agreement with the measurements of Schlinker. Correlation studies concluded that the passage of large scale eddies in the boundary layer over the airfoil trailing edge generated the noise. This conclusion was important to selecting the characteristic length scale needed in the acoustic scaling law developed in the present study. A further discussion is given in the section titled Airfoil Boundary Layer Characteristics.

The investigation by Brooks and Hodgson (ref. 10) used a cross-spectrum approach to extract the trailing edge noise for an isolated airfoil. Sound pressure level dependence on directivity and Mach number were in close agreement with the theoretical analysis of Howe (ref. 11).

Trailing edge noise data has also been obtained from experiments in which the turbulent flow over a trailing edge is provided by a wall jet (refs. 12, 13, and 14) blowing over the edge of a flat plate. In addition, numerous airframe noise studies have provided trailing edge noise data. These programs, defined as "clean airframe" noise studies, provided fly-over noise measurements for clean wing and tail surfaces. A summary of the various investigations and the resulting conclusions is available in the publications of Fink (refs. 6 and 7). The data in reference 13 formed the basis of a semi-empirical trailing edge noise prediction procedure which is now part of the NASA ANOPP Program.

Theoretical Studies - Because trailing edge noise is produced by turbulence (which can be represented by quadrupoles) moving past a sharp trailing edge, one analytical approach to the problem is to use the Lighthill acoustic analogy (ref. 15). Thus, quadrupole sound sources are placed near the edge of a flat plate which produces amplification of the sound if the trailing edge is in the near field of the quadrupole. This formulation describes the type of model used in the study of Ffowcs Williams and Hall (ref. 16). Subsequently, Crighton and Leppington (ref. 17), Crighton (ref. 18) and Howe (refs. 19-21) used this approach in developing trailing edge noise analytical models.

An alternate approach which corresponds to the method employed here, is to work directly with the airfoil surface pressures. Since surface dipoles are generally more efficient sound radiators than volume quadrupoles, one need only consider the quadrupoles to the extent that they induce surface dipoles. These dipoles are the source of the amplification mentioned in the above paragraph. This approach was used by Chase (refs. 22 and 23) and Chandiramani (Ref. 24) for the case of zero ambient mean Mach number.

The technique of using the convecting surface pressures was generalized by Amiet (refs. 25 and 26) to include an ambient mean flow. Application of the Kutta condition produced downstream shed vorticity and also determined the magnitude of the induced sound. Brooks and Hodgson (ref. 10) also used the convecting surface pressure technique for their comparisons with experiment and found good agreement between theory and experiment. If properly treated, the first model using Lighthill's analogy and the second model using airfoil surface pressures should produce identical results, at least to lowest order because the surface pressures are determined by the volume quadrupoles.

Present Study

Objectives - The overall objective of the present study was to assess the importance of trailing edge noise as a helicopter rotor broadband noise source.

As part of this objective it was desired to develop a generalized noise prediction in which the altitude, speed, angular position of the helicopter, rotor tip speed, and rotor boundary layer details were specified. Hover was to be included as a special case.

Since existing full-scale and model scale rotor data are contaminated with other operative helicopter noise mechanisms assessing the importance of the turbulent boundary layer broadband noise necessitated conducting an experiment in which this mechanism could be isolated. This resulted in a two-phase program in which the first objective was to investigate the noise from an isolated two-dimensional airfoil in an acoustic wind tunnel with low incident turbulence levels. This simulation technique is shown in figure 1. In addition to obtaining acoustic data, the isolated airfoil study was required to provide turbulent boundary layer information at the airfoil trailing edge. The aerodynamic and acoustic data from the experimental study were then used to develop scaling relationships for trailing edge noise radiation from a two-dimensional airfoil segment. This effort was aided by the empirical formulation of Fink (ref. 6) and a separate analytical formulation developed as part of the present study. Both the scaling law and fundamental theoretical approach were compared with the several isolated airfoil studies to assess the accuracy of each approach.

The objective of the second phase of the study was to extend the stationary two-dimensional isolated airfoil results to the rotating frame case to provide full-scale rotor broadband noise predictions. Based on the generalized noise prediction procedure, the importance of trailing edge noise could then be assessed. This objective was achieved by comparing rotor trailing edge noise predictions with the total noise spectrum measured during a full-scale helicopter flyover when all noise mechanisms are present.

Approach - The first phase of the study was conducted using an untwisted segment of a helicopter main rotor. The isolated airfoil section was mounted between parallel sideplates (to provide two-dimensional flow) and tested in an acoustic wind tunnel (see fig. 2). Freestream Mach number was varied from $M = 0.1$ to 0.55 providing Reynolds numbers close to full-scale values. Noise and mean velocity profiles at the airfoil trailing edge were measured for a range of test conditions. A directional microphone was used to separate trailing edge noise from other facility background noise sources. Directivity information was acquired by locating the directional microphone system at different viewing angles relative to the airfoil. Geometric angle of attack was varied over a range of $\alpha = 0°$ to 12° to determine the effect of this parameter on the boundary layer development and the resulting noise radiation.

Test results were analyzed to determine scaling law relationships for trailing edge noise radiated in the overhead plane of the two-dimensional

isolated airfoil. Included in the scaling law evaluation was the previous boundary layer noise data reported by Schlinker (ref. 5) and the data of Brooks and Hodgson (ref. 10). These different experimental results provided a data base with widely varying freestream Mach number (M = 0.1 to 0.55), airfoil chord (c = 21 cm to 61 cm), and airfoil profiles to test the generality of the scaling law.

During the second phase of the study results of the two-dimensional isolated airfoil investigation were extended to the rotating blade case to provide predictions for the full-scale flyover conditions. The transformation from stationary coordinates to rotating coordinates assumed that spanwise segments of the rotor blade, shown in figure 1, radiate boundary layer trailing edge noise with the same spectrum and directivity as an isolated airfoil. The local relative velocity of the rotor blade segment determined the boundary layer details and the resulting absolute noise levels and spectrum shape. The generalized boundary layer details employed in the noise prediction were determined by flat plate boundary layer theory.

LIST OF SYMBOLS

A, B, C, D	Transmitted acoustic rays; see figure 14
AMP	Decrease in directional microphone response due to scattering by turbulence
a	Apparent source to shear layer separation distance in flow plane; see Appendix C
b	Semichord = c/2
b_1	Apparent source-to-shear layer separation distance in vertical plane; see equation (C.12)
c_o	Sound speed
c	Airfoil chord
D	Directional microphone reflector aperture diameter
$D(\theta_e,\phi)$	Directivity factor defined by equation (26)
$\bar{D}(\theta_e,\phi)$	Normalized directivity factor defined by equation (32b)
$DIFF(\tilde{\omega})$	Difference between airfoil surface pressure spectra and flat plate surface pressure spectra
d	Focal point microphone diameter
E	Fresnel integral combination defined by equation (9)
F_1	Function describing scaling law spectrum; see equation (67)
$F(\tilde{\omega})$	Spectrum function defined by equation (22b)
f	Frequency
f_{max}	Frequency parameter defining scaling law spectrum peak; see equation (67)
G	Directional microphone gain; see equation (A.1)
g	Normalized airfoil response function; see equation (11)
H	Directional sensitivity of reflector
h	Source-shear layer separation distance; see figure 13
$\hat{i}, \hat{j}, \hat{k}$	Unit vectors in x, y, z directions, respectively
i	$\sqrt{-1}$
K	Constant in trailing edge noise theory; see equation (74)
K_1	Constant in scaling law for trailing edge noise; see equation (68)
K_x	ω/U
K_y	$\omega y/c_o\sigma$

k_x, k_y	Wavenumbers for x and y dimensions
ℓ	Effective lift function defined by equation (13a)
l_y	Spanwise length scale of surface pressure; see equation (19)
M	Freestream Mach number
$\underline{M}_a$	Spanwise flow Mach number
M_c	Turbulence convection Mach number
$\underline{M}_{ch}$	Chordwise flow Mach number
$\underline{M}_f$	Flight Mach number in rotor plane
$\underline{M}_r$	Mach number of source relative to fluid
$\underline{M}_s$	Mach number of flow relative to rotor hub
$\underline{M}_t$	Tip Mach number
$\underline{M}_z$	Axial flow Mach number
OASPL	Overall sound pressure level
$\underline{OS}$, OS	Vector and unit vector from retarded source position to observer
P_o	Magnitude of pressure wavenumber component
p_i	Surface pressure jump induced by edge
p_s	Sum of p_i and p_t
p_t	Surface pressure incident on edge
$\overline{p^2}_{DM}$	Mean-square of focal point microphone sound pressure level
$\overline{p_o^2}$	Mean-square of omnidirectional microphone sound pressure level
q	Dynamic pressure of freestream
R	Acoustic source to reflector distance for on-axis source
R_c	Reflector radius of curvature
R_l	Acoustic source to reflector distance for off-axis source
Re	Reynolds number
Re_{cr}	Critical Reynolds number for transition to turbulence
RPM	Revolutions per minute
$R_{qq}(\lambda,y)$	Fourier transform of surface pressure wavenumber spectrum; see equation (16)
$\bar{R}_{qq}(x,y)$	Fourier transform of R_{qq}; see equation (17)
r, r_o	Source to observer distance
r_e	Radius of microphone array in retarded source coordinate system
r_i	Focal point microphone distance from reflector surface

S_H	Designates apparent source in horizontal plane; see figure 47
St	Strouhal number
S_V	Designates apparent source in vertical plane; see figure 47
$SPL_{1/3}$	1/3 octave band sound pressure level
$S_{pp}(\underline{x},\omega)$	Sound spectrum
$S_{pp}(x,\omega,\gamma)$	Instantaneous sound spectrum as a function of azimuthal angle
$S_{qq}(\omega,y)$, $S'_{qq}(\omega,y)$	Surface pressure spectrum for a flat plant and an airfoil
s	Airfoil span
s_1	Distance along ray path between source and shear layer
T	Boundary layer trip thickness; also airfoil trailing edge thickness
T_e	Propagation time of sound to reach observer
t	Time
t_1	Distance along ray path between apparent source, S_V, and shear layer
U, U_o	Freestream velocity
U_c	Convection velocity of surface pressure pattern
U/U_o	Local velocity in boundary layer normalized by freestream velocity
ΔW	Diffraction pattern half-width
$\underline{x},x,y,z$	Cartesian coordinates (also, x is the distance defining the off-axis source position; see figure 12)
$\underline{x}_1$	Coordinate system defined by equation (48)
$\underline{x}_2$	$\underline{x}_1$ coordinate system rotated about z_1 by γ
$\underline{x}_3$	$\underline{x}_2$ coordinate system rotated about y_2 by γ
$\underline{x}_o$	Observer position in $\underline{x}$ coordinate system
$\underline{x}_p$	Source position defined by equation (46)
$\underline{x}_s$	Retarded coordinates of rotor hub
y_1	Sideline distance
α	Angle of airfoil out of flow plane; also geometric angle of attack
β	$\sqrt{1-M^2}$
γ	Azimuthal angle of rotor; also intermittency parameter
δ	Boundary layer thickness
δ^*	Boundary layer displacement thickness
ε	Small parameter

ζ	Parameter defined by equation (7)
ζ_o	Specific value of ζ given by equation (15)
ζ_1	$[(1-M\cos\theta_t)^2 - \cos^2\theta_t]^{1/2}$
η	Diffraction parameter - π Df sin ϕ_o/c_o; also, nondimensional parameter controlling reflector response to off-axis sources
$\boldsymbol{\theta}$	Parameter defined by equation (15)
θ	Observer angle defined in figure 26
θ'	Observer angle for rotor problem defined in figure 27
θ_c	Propagation angle of acoustic ray inside open jet (see figure 13)
θ_e	Angle defining retarded source position
θ_m	Propagation angle of acoustic ray in the absence of flow (see figure 13)
θ_t	Propagation angle of transmitted acoustic ray outside open jet (see figure 13)
λ	Wavenumber given by equation (5)
μ	Parameter defined by equation (7)
ν	Kinematic viscosity of air
ρ_o	Density of air
$\tilde{\omega}$	Nondimensional frequency, $\tilde{\omega} = \omega\delta^*/U$

THEORETICAL FORMULATION OF THE TRAILING EDGE NOISE MECHANISM

Noise Model for Isolated Airfoil in Rectilinear Motion

The foundation for the trailing edge noise model developed in the present study is described in references 25 and 26. The model assumes a frozen surface pressure pattern which convects downstream at a Mach number M_c past the trailing edge. Upon approaching the trailing edge the pressure jump across the airfoil is forced to zero to satisfy the Kutta condition. This gives rise to an induced pressure field which propagates away from the trailing edge region.

The surface pressure jump, Δp_t, due to the convecting turbulence is decomposed into spatial Fourier components of the form

$$\Delta p_t(x,y) = P_0 e^{-i(\lambda x + k_y y)} \tag{1}$$

where the time dependence exp ($i\omega t$) has been removed. Here x is the chordwise coordinate, y the spanwize, and z the normal. The airfoil lies in the z = 0 plane and x = 0 designates the trailing edge. The parameter λ is related to the chordwise gust convection speed U_c by

$$\lambda = \omega/U_c \tag{2}$$

Satisfying the Kutta condition at the trailing edge then gives rise to an induced surface pressure jump given by equations (12) and (32) of reference 27 which is

$$\Delta p_i(x,y,z=0) = -\frac{1}{\pi}\int_0^\infty \sqrt{\frac{r}{\xi}}\ \Delta p_t(\xi,y)\, e^{-i(\zeta+\mu M)(r+\xi)}\, \frac{d\xi}{r+\xi} \tag{3}$$

Here r (= -x) represents the distance between a point, x, on the airfoil and the trailing edge.

Also

$$\zeta^2 \equiv \mu^2 - k_y^2/\beta^2 \tag{4}$$

$$\mu \equiv MK_x/\beta^2 \tag{5}$$

$$\beta^2 \equiv 1 - M^2 \tag{6}$$

$$K_x \equiv \omega/U \tag{7}$$

where M is the freestream Mach number. This equation was derived for a semi-infinite flat plate airfoil with a trailing edge but no leading edge. A correction for the leading edge could be added to the solution in an iterative scheme as described in reference 27, but this will not be needed here.

Equation (3) was given in reference 27 for an airfoil surface pressure rather than a surface pressure jump. However, since the problem treated in reference 27 is antisymmetrical above and below the airfoil, the results apply as well to a pressure jump. For the present problem writing the equation in terms of a surface pressure jump is necessary since the problem is not antisymmetrical. Far upstream of the trailing edge the surface pressure is produced by volume quadrupoles and induced surface dipoles which double the pressure on the side containing the turbulent eddy and cancel it on the other side. Downstream of the trailing edge the pressure is produced by the frozen quadrupoles resulting in a pressure field whose magnitude is one-half of the pressure upstream.

Reference 26 mistakenly says that the pressure is forced to zero by the Kutta condition at the trailing edge, but it is really the pressure jump that is being forced to zero. This misstatement has caused some confusion to readers. The equations in reference 26 are for the pressure jump, however, and the predictions therein are not affected by this misstatement.

Substituting the assumed incident surface pressure (or surface pressure jump) given by equation (1) into equation (3) gives for the induced pressure jump.

$$\Delta p_i(x, y, z = 0) = -P_0 \, e^{i(\lambda r - k_y y)} \left\{ 1 - (1+i) E^* \left[r(\lambda + \mu M + \zeta) \right] \right\} \tag{8}$$

where

$$E(x) \equiv \frac{1}{\sqrt{2\pi}} \int_0^x e^{it} \frac{dt}{\sqrt{t}} \tag{9}$$

is a combination of Fresnel integrals, and the star on E represents the complex conjugate.

The total surface pressure jump is the sum of incident and induced pressure jumps. The surface loading is equated to a dipole strength which is used to calculate the noise generated. In the original derivation given in reference 25, the incident pressure jump was erroneously omitted in calculating the noise; reference 26 gives the corrected results, including the incident pressure jump. However, equation (1) is not an ideal representation of the incident pressure, as noted in reference 26, since it discontinuously arises at the leading edge of the airfoil, rather than growing gradually with the growth of the boundary layer. This would give rise to an erroneous leading edge term in the noise calculation. Thus, equation (1) will be modified slightly with an exponential convergence factor, $\exp(\varepsilon\lambda x)$, so that the incident pressure at the trailing edge ($x = 0$) is unchanged from equation (1), but is small at the leading edge ($x = -c$). This will be the case if

$$\epsilon \lambda c >> 1 \tag{10a}$$

Also, ϵ will drop out of the result if

$$\epsilon << 1 \tag{10b}$$

Thus, the total surface pressure jump is taken to be

$$\Delta p_s = P_0 e^{-i(\lambda x + k_y y)} \left\{ e^{\epsilon \lambda x} - 1 + (1+i) E^* \left[r(\lambda + \mu M + \zeta) \right] \right\} \tag{11}$$

$$\equiv P_0 g(x, Kx, \lambda, ky) \qquad -c < x < 0$$

The last identity defines the normalized response function, g.

For an airfoil in rectilinear motion the far-field sound can be calculated in the same manner as described in reference 28 for leading edge noise. This was the method used for trailing edge noise described in references 25 and 26. The normalization of g in reference 28 differs from that in equation (11) above by the factor $2 \pi \rho_0 b U_c$. Also, the factor U in equation (18) of reference 28 should be U_c for a surface pressure convecting at other than the freestream velocity. Taking account of this factor, equation (15) of reference 28 for the far-field sound spectrum of an airfoil in rectilinear motion becomes

$$S_{pp}(x, \omega) = \left(\frac{K_x M z b}{2 \pi \sigma^2} \right)^2 \frac{\pi s}{2 U_c} \left| \mathcal{L}(x, K_x, \lambda, K_y) \right|^2 \Phi_{qq}(\lambda, K_y) \tag{12}$$

where

$$|\mathcal{L}| \equiv \left| \int_{-c}^{0} g(x_0, K_x, \lambda, K_y) \, e^{-i \mu x_0 (M - x/\sigma)} \, \frac{dx_0}{b} \right| \tag{13a}$$

$$K_y \equiv \omega y / c_0 \sigma \tag{13b}$$

$$\sigma^2 \equiv x^2 + \beta^2 (y^2 + z^2) \tag{13c}$$

s is the airfoil span and Φ_{qq} is the wavenumber spectrum of the airfoil surface pressure produced by the turbulence. The function $\mathcal{L}$ can be thought of as an "effective lift". For an observer directly above the retarded source position ($x = \beta z$, $y = 0$), all points on the airfoil will be at equal retarded distances

from the observer. For this case the exponential phase factor in equation (13a) drops out and $\mathcal{L}$ becomes the normalized lift.

Substitution of equation (11) for g into equation (13a) and assuming equation (10) holds gives for $\mathcal{L}$

$$|\mathcal{L}| = \frac{1}{\Theta} \left| e^{i2\Theta} \left[1 - (1+i)E^*(2(\bar{\lambda} + \bar{\mu}M + \zeta_0))\right] \right.$$
$$\left. + \sqrt{\frac{\lambda + \mu M + \zeta_0}{\mu x/\sigma + \zeta_0}} \; (1+i)E^*(2(\mu x/\sigma + \zeta_0)) \right| \tag{14}$$

where

$$\Theta \equiv \bar{\lambda} + \bar{\mu}(M - x/\sigma)$$
$$\zeta_0 \equiv \zeta\Big|_{k_y = K_y} = \mu\sqrt{x^2 + \beta^2 z^2}\,/\sigma \tag{15}$$

and where the bar over λ, μ and ζ indicates normalization by the semichord b.

The only remaining unknown in equation (12) is the surface pressure spectrum Φ_{qq} of the turbulence. Since the wavenumber spectrum Φ_{qq} and the cross-correlation function R_{qq} are Fourier transforms of one another

$$\Phi_{qq}(\lambda, K_y) = \frac{1}{2\pi}\int_{-\infty}^{\infty} R_{qq}(\lambda, y_o)\, e^{-iK_y y_o}\, dy_o \tag{16}$$

The quantity $R_{qq}(\lambda, y)$ can be related to the cross-spectrum that would be measured by two probes separated by a distance y. Because the turbulence is assumed to be frozen and convects at a speed U_c, it can be described by a correlation function $\bar{R}_{qq}(x - U_c t, y)$. For fixed $t = t_o$, the function $\bar{R}_{qq}(x - U_c t, y)$ represents a spatial cross correlation while for fixed $x = x_o$ the function represents a timewise cross correlation, i.e., the cross-correlation function obtained from two fixed surface probes as the fluid convects by. The Fourier transform of the first case with respect to x gives the wavenumber spectrum R_{qq} while the Fourier transform of the second case with respect to time gives the frequency spectrum S_{qq}. The two are related by the factor U_c as noted below

$$R_{qq}(\lambda, y) = \frac{1}{2\pi}\int_{-\infty}^{\infty} \bar{R}_{qq}(x - U_c t, y)\, e^{-i\lambda x}\, dx$$
$$= \frac{U_c}{2\pi}\int_{-\infty}^{\infty} R_{qq}(U_c(\tau - t), y)\, e^{-i\omega\tau}\, d\tau \tag{17}$$
$$= U_c\, S_{qq}(\omega, y)$$

For an observer in the y = 0 plane, $K_y = 0$ and equations (16) and (17) give

$$\Phi_{qq}(\lambda,0) = \frac{U_c}{\pi}\int_0^\infty S_{qq}(\omega, y_o)\, dy_o \tag{18}$$

where the fact that $S_{qq}(\omega,y)$ is symmetric about y = 0 was used. The spanwise correlation function $l_y(\omega)$ can then be defined as

$$\ell_y(\omega) \equiv \frac{1}{S_{qq}(\omega,0)} \int_0^\infty S_{qq}(\omega, y_o)\, dy_o \tag{19}$$

For $y \neq 0$, equation (18) would contain a factor exp $(-i\, K_y\, y_o)$ under the integral, and equation (19) could not be used to replace this integral. However, here $\Phi_{qq}(K_x,K_y)$ will be assumed to be independent of K_y; i.e., the assumption is made that

$$\Phi_{qq}(\lambda, K_y) \approx \Phi_{qq}(\lambda,0) \tag{20}$$

Then equation (12) becomes

$$S_{pp}(\underline{x},\omega) = \left(\frac{K_x M z b}{2\pi\sigma^2}\right)^2 \frac{s}{2} \left|\mathcal{L}(x,K_x,\lambda,K_y)\right|^2 \ell_y(\omega)\, S_{qq}(\omega,0) \tag{21}$$

The assumption given by equation (20) does not eliminate the angle ϕ from the directivity prediction. It is only a statement of the details of the boundary layer surface pressure distribution, and although this distribution affects the directivity of the noise generated, it is believed that the other factors such as spanwise correlation length, which are retained in the analysis, are more important.

As in references 25 and 26, $S_{qq}(\omega,o)$ will be approximated using measurements for flat plate boundary layers. Thus, the surface pressure spectrum data of Willmarth and Roos (ref. 29) (also presented as fig. 7-39 of ref. 30) for a turbulent boundary layer flow of density ρ_o and freestream speed U can be approximated by the expression

$$S_{qq}(\omega,0) = \left(\frac{1}{2}\rho_o U^2\right)^2 \frac{\delta^*}{U}\, 2\times 10^{-5}\, F(\varpi) \tag{22a}$$

$$F(\varpi) \equiv (1 + \varpi + 0.217\varpi^2 + 0.00562\varpi^4)^{-1} \tag{22b}$$

$$\int_{-\infty}^{\infty} F(\varpi)\, d\varpi \approx 3.22 \tag{22c}$$

where $\aleph = K_x \delta^*$ and δ^* is the turbulent boundary layer displacement thickness given approximately by (ref. 31)

$$\delta^*/c = 0.047\, Re^{-0.2} \tag{23}$$

and Re_c is the Reynolds based on chord. The spanwise correlation length can be found by graphical integration of the curve for B given in figure 13 of reference 32. This gives the value

$$\ell_y(\omega) \approx 2.1\, U_c/\omega \tag{24}$$

where U_c is the convection velocity of the turbulence. In general U_c is a function of frequency, but will here be set equal to the average value

$$U_c = 0.8\, U \tag{25}$$

It is realized that the expressions given by equations (20) to (25) are approximations which can lead to errors. This is especially true since they are intended for infinite flat plate boundary layers whereas for the present case there is a trailing edge which can affect the flow in the immediate vicinity. Difference between flat plate surface pressure spectra (in the absence of a trailing edge) and isolated airfoil surface pressure spectra are discussed in the section titled Trailing Edge Noise Predictions. Experimental measurements are used to quantify the differences between these configurations and predict the far field acoustic spectra for the isolated airfoil and helicopter rotor blade configurations investigated in the present study.

Equations (13) to (25) are the basis for the theoretical prediction method presented herein. (A semi-empirical prediction is given later.) It is interesting to examine certain of these expressions in limiting cases for comparison with work done previously. Because K_y is set equal to zero in $\Phi_{pp}(K_x,K_y)$, the only remaining factors contributing to the directivity function $D(\theta,\phi)$ are

$$D(\theta_e,\phi) = \left(\frac{z r_e}{\sigma^2}\right)^2 |\mathcal{L}|^2 \tag{26}$$

where θ is the angle between the downstream x axis and the source observer line and ϕ is the angle between the xy plane and the plane containing the x axis and the observer (see figure 3). Thus,

$$\begin{aligned} x &= r \cos\theta \\ y &= r \sin\theta \cos\phi = y_e \\ z &= r \sin\theta \sin\phi = z_e \end{aligned} \tag{27}$$

The retarded coordinates r_e and θ_e are identified by the subscript e and can be shown to be (see e.g., reference 39)

$$x = r_e (M + \cos \theta_e)$$

$$\sigma = r_e (1 + M \cos \theta_e) \tag{28}$$

For the case of large chord (or high frequency)

$$\lambda b \gg 1$$

$$K_x b \gg 1 \tag{29}$$

$$\mu b \gg 1$$

and using the relation

$$E^*(x) \xrightarrow[x \to \infty]{} \frac{1-i}{2} \tag{30}$$

equation (14) becomes

$$|\mathcal{L}| \to \frac{1}{\mathfrak{D}} \sqrt{\frac{\lambda + \mu M + \zeta_0}{\mu x/\sigma + \zeta_0}} \tag{31}$$

In the y = 0 ($\phi = \pi/2$) plane $\zeta_0 = \mu$ so that from equations (26), (27), (28), and (31)

$$\bar{D}(\theta_e, \pi/2) \to 2 \sin^2 (\theta_e/2) (1 + M \cos \theta_e)^{-1} \left[1 + (M - M_c) \cos \theta_e\right]^{-2} \tag{32a}$$

where

$$\bar{D}(\theta_e, \phi) \equiv D(\theta_e, \phi) / D\left(\frac{\pi}{2}, \frac{\pi}{2}\right) \tag{32b}$$

A result equivalent to this has been obtained by other investigations. For example, Howe (ref. 11) obtains equation (32) but with one additional factor since he allows the shed vorticity to convect downstream at a speed unequal to the stream speed. If these two speeds are equated, as is assumed here, Howe's result is the same as equation (32). Goldstein (ref. 42) also obtains a directivity expression for trailing edge noise, but in the presence of a shear layer. If equation (3.44) of Goldstein's paper is corrected for shear layer refraction in the manner described by Amiet (ref. 34), the result is identical to equation (32) above. The details of this comparison with Goldstein's results for both leading and trailing edge noise is to be published in J. Sound and Vibration. Additional discussions of Goldstein's analysis are given in the section titled "Experimental Assessment of Trailing Edge Noise Radiation From a Two-Dimensional Airfoil Section."

For low frequency or small chord/wavelength

$$\bar{D}(\theta_e, \phi) = \left(\frac{z r_e \bar{\lambda}}{\sigma^2 \mathfrak{D}}\right)^2 \tag{33}$$

Thus, for an observer in the y = 0 plane

$$\bar{D}\left(\theta_e, \frac{\pi}{2}\right) = \frac{\sin^2\theta_e}{(1+M\cos\theta_e)^2\left[1+(M-M_c)\cos\theta_e\right]^2} \tag{34}$$

This gives a compact dipole like behavior in that the directivity varies as $\sin^2\theta_e$ rather than $\sin^2\theta_e/2$ as in equation (32). Equation (34) is not precisely the directivity of a dipole which would be

$$\bar{D}\left(\theta_e, \frac{\pi}{2}\right) = \frac{\sin^2\theta_e}{(1+M\cos\theta_e)^4} \tag{35}$$

The reason for this difference is that the assumptions given by equation (10), which was used in deriving equation (11), no longer hold for very low frequency. This could be rectified by retaining in equation (14) the exponential term from equation (11). However, this is not considered necessary as trailing edge noise is basically a high frequency phenomenon localized near the trailing edge. As frequency decreases causing the wavelength to approach the chord length it becomes improper to describe the noise as coming from a small region near the trailing edge because the leading edge gives a contribution. Thus, at low frequency it becomes less meaningful to consider trailing edge noise as a discrete mechanism. Verification of the high frequency characteristics of trailing edge noise is provided by the good agreement between the directivity pattern of equation 32 and the measurements obtained in the present study (see subsections titled Directivity Assessment and Comparisons with Previous Investigators).

Rotating Blade Noise Prediction

Equation (21), together with the associated equations for ℓ and S_{pp}, gives the far-field trailing edge noise of an airfoil in rectilinear motion. This formulation must now be transformed to the rotating frame to provide a propeller or helicopter rotor trailing edge noise prediction. The method employed assumes that the spectrum of a given blade segment is, at any particular instant, given by equation (21). This "instantaneous spectrum" varies as the rotor moves about the azimuth. To find the final spectrum, this "instantaneous spectrum" is averaged around the azimuth, together with a weighting factor which accounts for retarded time effects. This is the method used in references 35-37, and is a standard technique discussed further by Bendat and Piersol (ref. 38).

The present formulation for trailing edge noise is somewhat simpler in comparison to studies in references 35-37. In the previous studies, the problem of rotor-turbulence interaction was modeled analytically, and this involved treating blade-blade force correlations since more than one blade could intersect a given eddy. For trailing edge noise, the mechanism for producing blade-blade correlation is absent and the noise from several blades is determined by the noise from a single blade multiplied by the blade number.

The present analysis will, thus, be concerned with calculating the average spectrum produced by a single blade segment. Figure 4 shows the geometry of the problem. The origin of the x, y, z axis is fixed to the rotor hub with z being the rotor axis. The axial component of flow is in the negative z direction. The observer is assumed to be in the x-z plane at a distance r from the hub and at an angle θ' with the z axis. The nonaxial component of flow $\underline{M}_f$, is at an angle ψ to the y axis, pointing inward as shown. The observer is fixed relative to the rotor hub, and the x, y, z coordinate system.

The blade segment is assumed to be a flat plate making an angle α with the x-y or azimuthal plane where

$$\cot\alpha = \frac{M_t + M_f \cos(\gamma+\psi)}{M_z} \tag{36}$$

where M_t = azimuthal Mach number of the blade (relative to the fixed observer, not the fluid). Equation (36) assumes that the airfoil is aligned with the flow, implying zero steady loading. Because of the skewed inflow, there will be a spanwise component $\underline{M}_a$ of flow over the blade where

$$\underline{M}_a = -M_f \sin(\gamma+\psi)(\hat{i}\sin\gamma + \hat{j}\cos\gamma) \tag{37}$$

The chordwise component $\underline{M}_{ch}$ of flow Mach number is

$$\underline{M}_{ch} = \left[M_t + M_f \cos(\gamma+\psi)\right](-\hat{i}\sin\gamma + \hat{j}\cos\gamma) + \hat{k}\, M_z \tag{38}$$

The expression given by equation (21) for the far-field sound of an airfoil in rectilinear motion is written in terms of the present airfoil position. In order to be able to apply this relation to the rotating airfoil segment, the equivalent of the present position must be calculated for the airfoil segment. This "present position" is the position of the airfoil segment relative to the fluid if it were to move along a rectilinear path after sound generation until that sound reached the observer. An alternative method would be to calculate the retarded source position and rewrite equation (21) in terms of the retarded source position. Both methods should be of equal difficulty and should give the same results; the former will be used here since it is the method used in the previous references.

Both methods begin with a calculation of the retarded source position of the airfoil segment (or the rotor hub since distances on the order of the acoustic source size are not important when calculating the source position for a far-field observer). If at time t = 0 a marker is placed in the fluid and a burst of sound is emitted, at time $t = T_e$, when the observer hears the sound burst, the marker will move to position $\underline{x}_s$. The observer is at

$$\underline{X}_o = r(\hat{\imath} \sin\theta' + \hat{k} \cos\theta') \tag{39}$$

which corresponds to a distance r_e from the retarded source point $\underline{x}_s$. Thus,

$$r_e^2 = (r \sin\theta' - x_s)^2 + y_s^2 + (r \cos\theta' - z_s)^2 \tag{40}$$

Also,

$$T_e = r_e / c_o \tag{41}$$

Since $\underline{M}_f$ and $\underline{M}_z$ are given by

$$\underline{M}_z = -M_z \hat{k}$$

$$\underline{M}_f = -M_f(\hat{\imath} \sin\psi + \hat{\jmath} \cos\psi) \tag{42}$$

the retarded source coordinates are

$$x_s = -T_e c_o M_f \sin\psi = -M_f r_e \sin\psi$$

$$y_s = -M_f r_e \cos\psi \tag{43}$$

$$z_s = -M_z r_e$$

Substitution of equation (43) into equation (40) leads to the following result for r_e

$$r_e = \frac{r}{1 - M_s^2} \left[M_s \cos\Theta + \sqrt{1 - M_s^2 \sin^2\Theta} \right] \tag{44}$$

where

$$\underline{M}_s \equiv \underline{M}_f + \underline{M}_z$$

$$M_s^2 = M_f^2 + M_z^2 \tag{45}$$

and $M_s \cos\Theta = M_f \sin\psi \cos\theta' + M_z \cos\theta'$.

By calculating $(\underline{M}_s/\underline{M}_s) \cdot (-\underline{x}_o)$, Θ is shown to be the angle between the convection Mach number $\underline{M}_s$ and the vector linking the observer and the source, $-\underline{x}_o$. Substitution of equation (44) into equation (43) determines the retarded source position $\underline{x}_s$.

The "present" source position $\underline{x}_p$ is found by adding to the retarded source vector a vector giving the chordwise airfoil movement during the time T_e. The spanwise component of fluid velocity is ignored here since it was ignored in deriving equation (21). This is possible because in calculating the noise of an infinite span airfoil in rectilinear motion, any spanwise flow velocity can be eliminated by a coordinate transformation. The only purpose of calculating the "present" source position is to find the appropriate coordinates for use in equation (21). This position is

$$\underline{x}_p = \underline{x}_s + \underline{M}_{ch} c_o T_e \tag{46}$$

Introducing equations (43) and (38) into equation (46) gives

$$\begin{aligned} \underline{x}_p / r_e = &-\hat{i}\left[M_t \sin\gamma + M_f \cos\gamma \sin(\gamma+\psi)\right] \\ &+\hat{j}\left[M_t \cos\gamma - M_f \sin\gamma \sin(\gamma+\psi)\right] \end{aligned} \tag{47}$$

For a coordinate system at this "present" source position the observer has coordinates $\underline{x}_1$ given by

$$\underline{x}_1 = \underline{x}_o + \underline{x}_p \tag{48}$$

Equation (21) is given in a coordinate system in which the flat plate airfoil lies in the x-y plane with the span along y. The $\underline{x}_1$ coordinate system above must be rotated to the same orientation with respect to the airfoil. Rotation of the $\underline{x}_1$ system about the z_1 axis by an angle γ gives the $\underline{x}_2$ system with y_2 now pointed along the airfoil span

$$\begin{aligned} x_2 &= x_1 \sin\gamma - y_1 \cos\gamma \\ y_2 &= x_1 \cos\gamma + y_1 \sin\gamma \\ z_2 &= z_1 \end{aligned} \tag{49}$$

By rotating the $\underline{x}_2$ system about the y_2 axis by an angle α gives the $\underline{x}_3$ system with x_3 along the chord pointing from leading to trailing edge and

$$\begin{aligned} x_3 &= x_2 \cos\alpha - z_2 \sin\alpha \\ y_3 &= y_2 \\ z_3 &= x_2 \sin\alpha + z_2 \cos\alpha \end{aligned} \tag{50}$$

The $\underline{x}_3$ system is the appropriate system for calculation of the observer position needed in equation (21). Introducing equations (47) to (49) and equation (39) into equation (50) gives for the observer position

$$x_3 = r_e M_f \cos\alpha - r_o \cos\Phi$$

$$y_3 = x_o \cos\gamma + M_f r_e \sin(\gamma+\psi) \tag{51}$$

$$z_3 = (x_o \sin\gamma + r_e M_f)\sin\alpha + z_o \cos\alpha$$

where

$$\cos\Phi = \cos\theta' \sin\alpha - \sin\theta' \sin\alpha \cos\alpha \tag{52}$$

and

$$r_o^2 = x_o^2 + y_o^2 + z_o^2 \tag{53}$$

Here Φ is the angle between the x_3 axis and the actual airfoil position (not the "present" position defined above); this can be seen by substituting $\underline{x}_o$ for $\underline{x}_1$ in equation (49) and proceeding to the calculation of x_3 in equation (51).

Equations (51) to (53) are the appropriate "instantaneous observer coordinates" to use in calculating the sound spectrum given by equation (21). The angle $\gamma = \Omega t$ is a function of time. In order to calculate the time averaged spectrum, an average around the azimuth must be determined. This average must account for both the Doppler shifting of frequency as the airfoil segment moves relative to the observer, and the retarded time effects as the blade moves around the azimuth. The latter correction is needed because the blade spends different amounts of time, in an acoustic sense, at each azimuthal location. As noted in reference 35, the proper azimuthal weighting is the factor ω/ω_o where ω is the frequency of the airfoil forces and ω_o is the Doppler shifted frequency. The azimuthally averaged spectrum is then

$$S_{pp}(\underline{x}, \omega) = \frac{1}{2\pi} \int_0^{2\pi} \frac{\omega}{\omega_o} S_{pp}(\underline{x}, \omega_o, \gamma)\, d\gamma \tag{54}$$

The spectrum $S_{pp}(\underline{x}, \omega_o, \gamma)$ for the case of relative motion between source and observer is related to $S_{pp}(\underline{x}, \omega, \gamma)$ with no relative motion by the Doppler factor ω/ω_o; i.e., as shown in reference 39.

$$S_{pp}(\underline{x}, \omega_o, \gamma) = \frac{\omega}{\omega_o} S_{pp}(\underline{x}, \omega, \gamma) \tag{55}$$

Thus, equation (54) and (55), together introduce a factor of $(\omega/\omega_o)^2$.

The Doppler factor ω/ω_o is shown in reference 39 to be

$$\frac{\omega}{\omega_o} = 1 + \frac{\underline{M}_f \cdot \hat{OS}}{1 - \underline{M}_s \cdot \hat{OS}} \tag{56}$$

where $\underline{M}_t$ = Mach number of source relative to observer

$\underline{M}_r$ = Mach number of source relative to fluid

$\hat{OS}$ = unit vector from retarded source position to observer.

In vector notation

$$\begin{aligned} \underline{M}_t &= M_t(-\hat{i}\sin\gamma + \hat{j}\cos\gamma) \\ \underline{M}_r &= \hat{i}(M_f \sin\psi - M_t \sin\gamma) + \hat{j}(M_f\cos\psi + M_t\cos\gamma) + \hat{k}\,M_z \\ \underline{OS} &= \hat{i}(x - x_s) + \hat{j}(y - y_s) + \hat{k}(z - z_s) \end{aligned} \tag{57}$$

Using equation (43) and the fact that $|\underline{OS}| = r_e$ gives

$$\hat{OS} = \hat{i}(x/r_e + M_f \sin\psi) + \hat{j}\,M_f\cos\psi + \hat{k}(z/r_e + M_z) \tag{58}$$

and finally from equation (56)

$$\frac{\omega}{\omega_o} = 1 + \frac{M_t\left[x\sin\gamma - M_f r_e\cos(\gamma+\psi)\right]}{(1-M_s^2)r_e - x\,M_f\sin\psi - z\,M_z} \tag{59}$$

The final result from the azimuthally averaged spectrum is given by equations (54), (55), and (59) with S_{pp} (x, ω, γ) in equation (55) given by equation (21). The x, y, z coordinates to be used in equation (21) are x_3, y_3, z_3, respectively, given by equation (51).

DESCRIPTION OF THE EXPERIMENT

Acoustic Research Tunnel

Operating Characteristics - The experimental study was conducted in the UTRC Acoustic Research Tunnel. A detailed description of the facility is given in reference 40. The tunnel, shown schematically in figure 2, is an open-circuit, open-jet design. The inlet is provided with a high length-to-diameter ratio honeycomb section and a series of turbulence suppression screens. These features, in conjunction with a large tunnel contraction, provide a spatially uniform, temporally steady flow with a controlled test section turbulence level of approximately 0.2 percent. Turbulence generators and grids can be inserted upstream of the nozzle to generate wake profiles and a range of turbulence levels in the test section.

The open jet test section is surrounded by a sealed anechoic chamber 4.9 m high, 5.5 m long (axial direction), and 6.7 m wide. Downstream of the test section the airflow enters a diffuser by way of a circular collector that has anechoic treatment on its flow impingement surface. The diffuser operates unstalled and is thus not a major source of background noise. To avoid tunnel fan noise from propagating upstream into the anechoic chamber, a Z-shaped muffling section with two right-angle bends and parallel treated baffles is located between the diffuser and the fan. The 1100 kW centrifugal fan exhausts to the atmosphere through an exhaust tower.

Tunnel speed is determined from total pressure measurements at the contraction inlet and static pressure measurements within the sealed anechoic chamber. Since losses are confined to the boundary layer, total pressure upstream and downstream of the contraction are predicted and have been verified, to be equal. The test section velocity has been shown to be temporally steady.

Open Jet Geometry and Test Section Arrangement - A rectangular 0.79 m by 0.53 m test section provided two-dimensional flow conditions for the helicopter main rotor blade segment. The blade segment was mounted vertically in the 0.53 m direction, between the two horizontal sideplates shown in figure 5. The sidewalls provided a uniform spanwise mean flow and eliminated the problem of additional noise generation by incident turbulence had the airfoil extended through the thick turbulent open-jet shear layer. The airfoil mounting plates on each sidewall permitted angle-of-attack variations.

Triangular tabs previously used to suppress the edge tone phenomenon (ref. 40) between the inlet nozzle and collector were not needed. This was because the asymmetry produced by the rectangular jet flowing into the circular collector destroyed the flow field spatial coherence responsible for edge tone generation. Removal of the edge tone suppression tabs was investigated in the earlier trailing edge noise study of Schlinker (ref. 5). Overall background noise was reduced by

approximately 5 dB by removing the tabs. Unfortunately, this improvement was not sufficient to detect the airfoil trailing edge noise over the facility background noise. As in the present study, a directional microphone was needed to measure the airfoil self noise.

Model Airfoil

The objective of the experimental phase of this study was to measure turbulent boundary layer noise at Reynolds numbers close to full scale. For this purpose, a 0.53 m spanwise segment of a helicopter main rotor was employed. (Note that all acoustic spectra measured in the present study were converted to the acoustic radiation from a unit spanwise length (1 ft or 0.3 m) of the model airfoil.) The airfoil segment, shown in figures 5 and 6, is part of a larger main rotor assembly used for aerodynamic response tests conducted at UTRC (ref. 41). The test airfoil with its 0.41 m chord permitted varying the Reynolds number between 9.5×10^5 and 5.2×10^6. Here the larger Reynolds number is close to the value describing the flow near the tip of a helicopter main rotor with the same chord and a tip Mach number near M = 0.8.

Although the operating Reynolds number range of the model airfoil was selected to simulate full-scale rotor conditions, transition was not expected to occur at the same location as on a production rotor blade. This is because the rotor segment in figure 6 had a smooth surface finish since it was machined airfoil section. Thus, transition would not occur until the start of the adverse pressure gradient. In contrast production rotors usually have an abrasion strip covering the leading edge of the profile as depicted by the airfoil cross-section shown in figure 7. The discontinuity in the joint between the abrasion strip and rotor surface can be sufficient to cause laminar to turbulent transition of the boundary layer upstream of the minimum static pressure.

Fortunately, the start of the adverse pressure gradient and the abrasion strip joint are located within the first 10 percent of the model airfoil chord. This is substantiated by figure 8 which shows the location of the minimum static pressure station on the airfoil suction side for the various angles of attack tested in the present study. Also shown is the approximate location of the abrasion strip joint on the specific production rotor which the model airfoil segment simulated.

To ensure that the transition point always occurred at the same point on the model airfoil the boundary layers were tripped at the 10 percent chord station on both sides of the airfoil. An additional trip, located at x/c = 0.08, was needed on the pressure surface side to enhance the surface roughness at positive angles of attack. Vortex shedding noise observed during preliminary tests at positive angles of attack indicated that a single trip would not provide a turbulent flow at the trailing edge on the pressure side of the airfoil.

The boundary layer tripping device employed a thin serrated aluminum tape with its serrations facing forward as shown in figure 6. This geometry is based on the technique reported by Hama in reference 42. Tape thickness was selected to provide minimum surface protrusion to avoid unnaturally large or distorted trailing edge turbulent boundary layers. The criteria selected in the present study required that the ratio of tape thickness, T, to the local boundary layer displacement thickness, δ^*, be unity, i.e., $T/\delta^* = 1$. This avoided disturbing the freestream velocity profile outside the boundary layer. Local δ^* values were estimated using the flat plate boundary layer equation. Velocities needed for this calculation were obtained from surface static pressure curves which were used to calculate the local inviscid velocity field.

Local Reynolds number based on the velocity at the trip thickness was approximately 400 on the airfoil suction side. Hama reported that the serrated trip becomes effective at a critical Reynolds number of $Re_{cr} \gtrsim 45$. This implies that the present trip thickness was sufficient to cause transition. Moreover, a constant spanwise transition station was assured because of the three-dimensional nature of the boundary layer disturbance (ref. 42). Note that the serrated trip approach is more effective than the traditional cylindrical trip device for which $Re_{cr} \sim 900$ (ref. 43) or the distributed roughness approach with $Re_{cr} \sim 120$ (ref. 43).

The presence of the above described boundary layer trips on the pressure side of the airfoil eliminated the phenomenon of discrete vortex shedding noise. Without these trips the boundary layer flow was laminar at positive angles of attack. Paterson, et al. (ref. 44) demonstrated that such a laminar boundary layer can cause vortex shedding noise at discrete frequencies.

Since the study of Paterson, et al., vortex shedding has been the subject of numerous model rotor, propeller, and airfoil studies. This mechanism, however, would not be expected to occur on production main rotors since the abrasion strip would cause early transition. Also, the high Reynolds number of the flow near the outer portion of the rotor span would result in early transition for this dominant noise region of the rotor. Therefore, from a practical standpoint vortex shedding is not an important noise mechanism. Consequently, the boundar layer trip on the two-dimensional airfoil ensured that the model airfoil tests simulated full-scale operating conditions. Additional verification of the absence of vortex shedding was obtained from the acoustic spectrum measurements.

Directional Microphone System

The objective of the experimental study was to measure the trailing edge noise generated by a two-dimensional segment of a helicopter rotor. The various facility background noise sources, shown in figure 9, dominated over the airfoil

noise. To suppress these extraneous sources and detect only the airfoil noise required the use of the directional microphone system illustrated in figure 9. This approach was previously shown by Schlinker (ref. 5) to be successful at isolating airfoil self noise. A brief discussion will be provided here to familiarize the reader with the technique with additional details presented in Appendix A.

Operating Characteristics - The UTRC wide frequency band, highly directional microphone system is similar to that previously developed for jet noise source location measurements. The experimental technique, based on an optical analogy, uses the reflecting surface of a concave mirror to form an image of the sound emanating from a segment of the airfoil surface. The present design was based on the work by Laufer, Schlinker, and Kaplan in reference 45 (see Schlinker (ref. 46) for a more detailed discussion), in which quantitative measurements of supersonic jet noise acoustic source distributions were made.

The 1.067 m aperture spherical reflector, shown schematically in figure 10, has a radius of curvature R_c = 1.346 m. A 0.635 cm microphone, situated at the focal point, is directed toward the reflecting surface (figs. 11, 12). A microphone grid is used in all experiments. The focal point microphone distance, r_i, from the center of the reflector is controlled by the simple lens equation shown in figure 12.

Test Set-up - The directional microphone test set-up is shown in the photographs of figures 5 and 11. The system was traversed parallel to the open jet from a station upstream of the airfoil leading edge to a station downstream of the trailing edge. Vertical position of the reflector centerline was aimed at midspan of the test section.

To obtain source directivity information in the plane normal to the airfoil, the system was aimed at several different angles relative to the open jet centerline. As the unit scanned past the airfoil, the output of the focal point microphone and the axial position sensor were recorded on magnetic tape. Traverse speeds were always less than 0.5 cm/sec.

Forward Flight Effects

Shear Layer Refraction and Scattering of Sound - For tests conducted at freestream Mach numbers less than 0.1, measurements outside the open jet can be used to directly infer the source noise characteristics. However, at higher Mach numbers, the open jet technique is influenced by the shear layer through which the sound is transmitted. The shear layer refracts, reflects, and scatters the sound radiated from the model significantly altering the

acoustic source directivity pattern. A brief discussion of the refraction corrections is presented here. Changes due to reflection by the shear layer were minimal for the angular measurement range investigated here. Additional details of the refraction corrections and the resulting "apparent" source position are given in Appendix B. Scattering effects on directional microphone measurements are also described.

An example of the ray path geometry for transmission of sound through a shear layer is shown in figure 13. Here, wavefronts propagating in the direction, θ_c, inside the airstream propagate in the direction, θ_t, outside the open jet. The actual path of the acoustic ray is described by the points SBO. The change from θ_c to θ_t is a result of refraction by the shear layer. Without flow the sound propagates at angle θ_m.

Directivity information in the present study was obtained over a range of angles, θ_c. To account for the refraction effect, the directional microphone system was rotated in advance to angle, θ_t, to obtain the sound initially radiated in the direction, θ_c. This is illustrated in figure 14(a). Scanning the directional microphone past the airfoil trailing edge isolated the sound radiated in the direction of interest.

Airfoil Angle of Attack in Open Jet - Lifting airfoils within an open jet induce curvature of the shear layer and deflection of the jet. If the wind tunnel has no downstream physical constraint on position of the deflected jet, the lifting airfoil rotates the jet until its downward momentum is equal to the lift force per unit time. The relative airfoil angle of attack is then reduced by the jet deflection. This effect was not accounted for in the present study. All angle of attack values, therefore, refer to the geometric angle of attack.

Instrumentation

Acoustic sound pressure levels at the reflector focal point were measured using a 0.635 cm diameter microphone (with grid) at normal incidence. The normal orientation introduced a frequency dependent microphone response which is typically a function of the angle between the normal to the diaphragm and the acoustic ray direction. This effect was included in the directional microphone gain calibration which compared the focal point microphone output with an omnidirectional microphone output at grazing incidence. The gain measurement, which was previosuly reported in reference 5, was repeated in the present study as a check on the directional microphone system (see Appendix B).

The focal point microphone signal was amplified and recorded on magnetic tape. The frequency response of the FM tape system was flat over the frequency

range investigated here. The output from a linear potentiometer, used to sense the directional microphone position, was also recorded. The data was processed with a 1/3 octave band analyzer. An X-Y plotter displayed the selected 1/3 octave band sound pressure level as a function of reflector aiming position.

The slew rate associated with the continuously varying focal point microphone output was less than the maximum acceptable rate for the 1/3 octave band analyzer. This was verified experimentally by stopping the transverse and checking for an analyzer output lag. Although this was not a problem in the present study, directional microphone measurements of a moving source could encounter such difficulties.

Mean velocity and turbulence intensity measurements at the airfoil trailing edge were acquired by a 0.025 mm diameter hot film probe operating in conjunction with a constant temperature anemometer system. The probe was calibrated directly in the tunnel test section.

Test Program

Airfoil trailing edge noise measurements were obtained over a range of Mach numbers, propagation angles, and airfoil angles of attack to assess the dependence on these parameters in the scaling laws and the trailing edge noise theory. Table I lists the test conditions.

The $\alpha = -0.4°$ angle of attack case in Table I corresponds to zero section lift on the airfoil. At this operating condition the turbulent boundary layers on the pressure and suction side of the airfoil would be expected to be approximately the same. In this case, both boundary layers would generate the same noise characteristics.

The $\alpha = 12°$ angle of attack provided the highest section lift without stalling the airfoil based on available airfoil lift curves. Mach number was limited to $M = 0.3$ for this operating condition because of the dramatic increase of facility background noise. This was because lifting airfoils at high angles of attack in an open jet induce curvature of the shear layer and deflection of the open jet. This deflection impinges the high velocity jet on the downstream collector generating sufficient noise to dominate over the signal enhancement obtained from the directional microphone.

Directivity measurements covered a large angular range for M = 0.3, but at higher Mach numbers only limited measurements could be obtained. In the upstream quadrant the limitation was due to the large refraction angle change. For example, at M = 0.55, sound radiated at $\theta_c = 90°$ is refracted to $\theta_t = 142°$. Placement of the sideline directional microphone traverse system for measuring the sound radiating at $\theta_t = 142°$ was not possible due to the presence of the upstream anechoic chamber wall. The dependence of θ_t on θ_c and M is given in Table II. In the downstream quadrant, measurements at small values of θ_c, corresponding to small θ_t angles, were limited by the dominance of the open jet background noise. Since jet noise varies with velocity to the eighth power at high jet velocities, it dominated over the 5th power dependence of the airfoil trailing edge noise.

AIRFOIL BOUNDARY LAYER CHARACTERISTICS

Objective

The objective of the airfoil boundary layer measurements was to document the boundary layer thickness, δ , at the trailing edge of the model airfoil. Direct measurements of this parameter were needed as an input to the trailing edge noise predictions. In addition, such measurements provided an assessment of the accuracy of using flat plate boundary layer calculations as an input to the noise predictions. If the flat plate boundary layer characteristics could be shown to predict the measured acoustic data with sufficient accuracy, then noise predictions would not require detailed velocity profile information at the airfoil trailing edge. This could, of course, only be expected to hold at small angles of attack where the flow is attached to both surfaces.

Boundary layer thickness is considered to be the length scale parameter involved in the trailing edge noise generation process. This follows from previous studies which showed that the size of the turbulent structure generating the noise is of the order of δ. For example the flow vizualization experiments of Yu and Joshi (ref. 9) revealed the presence of large-scale coherent motions in the outer part of the turbulent boundary later. The approximate scale of the coherent structure was of the order of the boundary layer thickness. Correlation studies concluded that the passage of these large-scale eddies over the airfoil trailing edge generated the trailing edge noise.

Previous investigators have used either the boundary layer thickness, δ, or the displacement thickness, δ^*. The latter parameter is usually chosen when the velocity profile shape makes it difficult to identify the edge of the boundary layer. The displacement thickness however, does not fully represent the physics of the noise generation mechanism as indicated by the above discussion.

Approach

Although the boundary layer thickness controls the noise generation process, it is often a difficult parameter to identify. A comparable length-scale parameter which can be easily measured is the location of the turbulent boundary layer intermittency interface. The mean interface location is determined by the value of the turbulent intermittency parameter, γ. This parameter defines the percentage of time the signal from a hot film probe displays an intermittent or turbulent signal when located near the outer edge of the boundary layer. Since the value of γ approaches zero at the edge of the boundary layer the location at which the hot film signal becomes steady can be used to identify the edge of the turbulent boundary layer.

Klebanoff (ref. 48) indicated that for a flat plate the height above the surface corresponding to an intermittency value of γ = 2% occurred at a distance

of approximately of 1.07 δ. This is illustrated schematically in figure 15 where the boundary layer thickness, based on $U/U_o = 0.99$, is compared with the intermittency interface location, δ_i. Notice that the distance at which the hot wire signal is unsteady for 2% of the time is comparable to the boundary layer thickness. Since δ_i is easily determined using the visual display of the hot film signal on an oscilloscope this method was employed to obtain an approximate measurement of the boundary layer thickness in the present study.

The above argument showing the equivalence of δ and δ_i was previously verfied only for a flat plate boundary layer. To assess the accuracy of this equivalence for an airfoil, mean velocity profiles were also measured in the present study. Comparisons of the value of δ_i with the normalized velocity profile curves indicated that the intermittency interface occurs near $U/U_o = 0.99$. Thus, $\delta_i/\delta \sim 1$ at the airfoil trailing edge in accordance with the flat plate data of Klebanoff. The intermittency interface distance, therefore, provided a comparable but simplified method for determining the boundary layer thickness.

All velocity profile surveys were conducted at a distance of 0.007 chords downstream of the airfoil trailing edge. Admittedly, these measurements corresponded to wake velocity profile surveys instead of boundary layer profile surveys on the airfoil surface. However, the close proximity of the measurement station to the airfoil trailing edge ensured that the outer edge of the wake velocity profile was similar to the boundary layer just upstream of the trailing edge. This was expected to be true for the small angle-of-attack attached flow conditions investigated in the present study.

Calibrations of the hot film probe employed in this study were conducted in the open jet test section. A commercially available linearizer circuit was used to obtain a linear velocity versus voltage response curve over a range of 0-191 m/sec. However, for velocities between 137 m/sec and 191 m/sec the circuit output became nonlinear. This occurred due to the decrease in static pressure inside the open jet test section at high velocities. The pressure changes resulted in a decrease of the fluid density which influences the heat transfer rate on the hot film. Such changes were not accounted for in the analog circuitry of the commercial linearizer unit since most hot film anemometer measurements are conducted in constant static pressure environments. For example, measurements of the downstream flow field development in a model jet are typically conducted at ambient pressure. Fortunately, the effect of static pressure changes were included in the present calibration data since the hot film probe was calibrated in the open jet test section. Absolute velocity profiles on the airfoil surface were then determined from the measured calibration curve. It is recognized that due to the nonlinear response of the anemometry circuitry at high Mach numbers turbulence measurements were only meaningful for $M \leq 0.4$.

Results

Mean Velocity Profiles and the Intermittency Interface Location - Figure 16 shows the measured mean velocity profile and the location of the intermittency interface on both sides of the model airfoil at $\alpha = -0.4°$. All dimensions have been normalized by the airfoil chord and velocities have been normalized by the maximum measured freestream velocity. Velocity profile data near $y/c = 0$ was not needed for the assessment of the noise predictions in the present study. However, such information was essential to determining the position of the hot film probe relative to the airfoil surface. Since velocity profile measurements were made at a minute distance downstream of the trailing edge, it was necessary to reference all transverse distances to a hypothetical extension of the airfoil chord. Thus, the $y/c = 0$ station in figure 16 coincided with the hypothetical airfoil extension.

The lack of a physical reference point downstream of the trailing edge made it difficult to identify the location of airfoil chord extension. This could only be determined visually be requiring the hot film to bisect the projected airfoil surface area when viewing the airfoil trailing edge from the downstream end. To provide a check on this approach the measured velocity profiles near $y/c = 0$ were used to identify the trailing edge stagnation point. Two straight lines were drawn through the suction and pressure side data points near $y/c = 0$ in figure 16. The intersection of these lines approximated the location of the stagnation point at the airfoil trailing edge. For the zero angle-of-attack case shown in figure 16 the location of this stagnation point agreed closely with the $y/c = 0$ reference point. Measurements of δ_i were, therefore, obtained relative to the desired extension of the airfoil chord.

Comparing the location of the intermittency interface with the velocity profile curves near $U/U_o = 0.99$ indicates that δ_i provides a comparable measurement of the boundary layer thickness. The replacement of δ by δ_i has, therefore, been verified for the $\alpha = -0.4°$ angle of attack test condition.

Also shown in figure 16 are the normalized turbulence intensity profiles defined by u'/u'_{max}. As expected from the criterion for selecting, δ_i, the fluctuating measurements approached zero at the intermittency interface. This once again confirmed that δ_i identifies the edge of the turbulent boundary layer. It should be noted that turbulent fluctuation measurements at the higher Mach numbers of $M = 0.43$ and 0.5 corresponded to the turbulent mass fluctuations defined by the ratio $(\rho'u')/(\rho'u')_{max}$. Although this ratio is plotted in figures 16(c) and 16(d) absolute values could not be specified due to the nonlinear characteristics of the hot film response at the high velocities.

A comparison of δ_i on both airfoil surfaces in figure 16 indicates that the boundary layers are similar at $\alpha = -0.4°$. This is demonstrated in figure 17(a) where the values of δ_i/c are plotted for the pressure and suction side surfaces at the various Mach numbers investigated in the present study. Also shown in

figure 17(a) is the flat plate boundary layer thickness calculation for δ/c. Here the turbulent boundary layer is assumed to start at the transition point determined by the boundary layer trip located at $x/c = 0.1$. The good agreement between the predicted values of δ/c and the measured values of δ_i/c indicates the applicability of the flat plate prediction at zero lift condition when both boundary layers develop under the influence of approximately the same adverse pressure gradient.

The effect of Mach number or Reynolds number is weak as shown by the experimental data in figure 17(a). This agrees with the flat plate turbulent boundary layer prediction in which δ varies according to $Re^{-0.2}$.

Figure 18 shows the boundary layer velocity profiles for $\alpha = 7.6°$ angle of attack. The boundary layers are no longer symmetric as in the $\alpha = -0.4°$ case. Here the airfoil trailing edge stagnation point, approximated by the intersection of the two straight lines, shows a small disagreement with the $y/c = 0$ station determined during the experiment. The offset was used to correct the measured values of δ_i to account for the apparent error in determining the $y/c = 0$ reference station. The advantage of measuring the complete velocity profile is now evident.

The mean velocity profiles in figure 18 indicate that the boundary layers are no longer symmetric. The intermittency interface station, however, still occurs where the mean velocity profile asymptotically approaches $U/U_o = 0.99$. Thus, δ_i, continues to provide a representative measurement of the boundary layer thickness, δ.

The variation of δ_i with Mach number is summarized in figure 17(b) for the $\alpha = 7.6$ case. Similar to the $\alpha = -0.4°$, changes with increasing Mach number are small. The flat plate boundary layer prediction would, obviously, be unable to predict the upper and lower surface values of δ_i.

After demonstrating that δ can be replaced by δ_i at $\alpha = -0.4°$ and $7.6°$ measurements at $\alpha = 12°$ were limited to determining the intermittency interface location. Figure 17(c) shows the experimental results at this highest angle of attack. As expected the suction surface boundary layer thickness has increased significantly relative to the $\alpha = -0.4°$ case while the pressure side boundary layer thickness has decreased.

Acoustic Scaling Law Dependence on Boundary Layer Thickness - Existing predictions for airfoil self noise contain a single boundary layer thickness parameter for each side of the airfoil. Unfortunately, at high-lift conditions the boundary layers on both sides of the airfoil are significantly different. One approach to circumventing the resulting dilemma is to use the average of

the suction and pressure side boundary layer thickness values. The Mach number and angle-of-attack dependence of this average value was obtained for the δ_i values in figure 17 and plotted in figure 19. A mean line has been drawn through the measured data points for use in later data reduction. For $\alpha = -0.4°$ and $7.6°$ the average value of δ_i is within 20% of the calculated flat plate boundary layer thickness when $M \leq 0.3$. Note that the effect of angle of attack on the radiated noise is considered to be weak for small α. This is because the boundary layer thickness parameter appears as a logarithmic dependence in the trailing edge noise scaling laws so that 20% error in δ_i introduces at most a 0.8 dB error in the amplitude scaling.

At the highest angle of attack in figure 19 the average value of δ_i no longer agrees with the flat plate boundary layer calculation for δ. Differences between data at the two lower angles of attack and this highest angle of attack are presently not understood.

DATA ACQUISITION AND DATA REDUCTION PROCEDURE

A demonstrated experimental approach to isolating turbulent boundary layer noise is through use of two-dimensional airfoil sections tested in an acoustic wind tunnel with low turbulence levels. In the present study a directional microphone was needed to separate the turbulent boundary layer noise from other facility background noise sources. Directivity information was obtained by orienting the directional microphone system at different viewing angles relative to the airfoil. Examples of the data acquired from the directional microphone system are given below. Also, a brief discussion of the data reduction procedure is provided to describe how the source distribution measurements are converted to absolute sound pressure levels associated with trailing edge noise.

Directional Microphone Data Acquisition Procedure

For each Mach number and directivity angle θ_c, there exists a location in the open jet corresponding to the apparent source position. This apparent source location controls the sideline traverse distance in figure 13 since the reflector-to-apparent source distance was required to be R = 2.07 m or 2.81 m. Once the sideline distance was determined the reflector centerline orientation relative to the open jet axis was adjusted to coincide with the transmission angle, θ_t, determined from refraction calculations. As shown in Table II, θ_t varies with θ_c and M.

After selecting the reflector sideline distance and orientation angle the directional microphone system was traversed past the isolated airfoil. Figure 20 is an example of the measured source distribution as the directional microphone system was traversed parallel to the open jet centerline. Such curves were obtained at each 1/3 octave band frequency between 1 kHz and 50 kHz. Each trace was determined by playing back the analog record from the tape recorder and passing it through the selected 1/3 octave band.

The first peak near the tunnel exit plane in each trace represents the open jet shear layer noise and nozzle lip noise. The spherical directional microphone system is sensitive to these acoustic sources because of the finite depth of field. Note that a large distance separated the nozzle exit from the airfoil trailing edge to avoid contamination of the airfoil source distribution by the tunnel lip noise.

The second peak located downstream of the airfoil trailing edge location in figure 20 is associated with acoustic radiation from the airfoil model. The displacement between the trailing edge and the apparent source position agrees with the expected shift due to convection of sound waves by the tunnel freestream. The downstream displacement of the apparent acoustic source position relative

to the airfoil trailing edge was determined analytically using the simple expression $\Delta x = h_1 U/c_o$. Here h_1 is the trailing edge-to-shear layer distance (see fig. 44) for a ray propagating at angle θ_t when M = 0. The parameter, Δx, represents the distance which the reflector, initially aimed at the trailing edge, must be moved downstream to measure the noise radiation in the presence of flow (fig. 44). Comparisons showed good agreement between the measured and predicted values of Δx. The good agreement between theory and experiment also provided an indirect confirmation of the refraction prediction for the angle θ_t.

To verify that the airfoil trailing edge noise mechanism was responsible for the second peak in each distribution, the airfoil was removed and the traverse was repeated for a few selected cases. The f = 5 kHz curve in figure 20(a) shows the resulting source distribution which is referred to as the facility background noise. Lip noise, open jet shear layer noise, and collector noise are the only contributors to this background noise.

One advantage of the directional microphone is now evident. The reflector, with its large gain, enhances sound arriving from a source on the mirror axis while rejecting sound arriving from other off-axis sources. In comparison, a single omnidirectional microphone would measure all three background noise sources in addition to the trailing edge noise. As previous investigators have indicated, the trailing edge noise source would be masked by the facility noise in this case.

Calculating Trailing Edge Noise Spectra from the Directional Microphone Data

Acoustic source distributions like those in figure 20 are typical of the features observed over the range of test conditions. From such curves the far-field trailing edge noise spectra were calculated. Specific equations developed for the data reduction purposes were presented by Schlinker in reference 5. The calculation procedure uses the absolute sound pressure level measured at the peak of the source distribution associated with the trailing edge noise radiation. Due to the presence of background noise sources it is necessary to correct the measured sound pressure level. Ideally, this would be obtained by subtracting the value of the background noise curve directly under the peak associated with the trailing edge noise.

Unfortunately, the background noise curve shown in figure 20(a) is a function of the airfoil angle of attack. This is because for high values of lift coefficient the airfoil deflects the open jet sufficiently to cause increased collector impingement noise. Removal of the airfoil to determine the open jet background noise levels is, therefore, possible only at zero lift conditions where the airfoil has no affect on the impingement noise. For this reason, a direct measurement of the facility background noise curve associated with finite lift conditions

was not possible. Instead, straight lines were drawn connecting the broadband noise levels on either side of the trailing edge noise peak in figure 20(b). The assumed sound pressure level beneath the peak represented the facility background noise. Based on the flat shape of the curve on either side of the peak in figure 20(b), a straight line was adequate for defining the facility background noise distribution.

The directional microphone data reduction procedure described in reference 5. determines the equivalent trailing edge noise spectrum which would be measured by a hypothetical omnidirectional microphone situated at the reflector station at which the peak occurred in figure 20. The equivalent noise spectrum in this case represents the sound field sensed by an omnidirectional microphone situated at the observer position (0) in figure 13. Applying the refraction angle and amplitude corrections (Table II) to the resulting experimental data converts the measurements at station 0 to the sound pressure level that an omnidirectional sideline microphone would sense at station D in figure 13. These corrections transform the experimental data to a measurement system in which the microphone is located inside the flow field and fixed relative to the noise source. Thus, the converted data corresponds to an airframe flyover measurement in which the microphone, situated at angle θ_c, is moving at the aircraft flight speed in a direction parallel to the flight path. This coordinate system is often referred to as the present coordinate system.

To facilitate comparisons with theoretical directivity predictions, it is convenient to convert all present coordinate system measurements to a retarded-time coordinate system. This latter coordinate system effectively moves the noise source downstream to its relative physical location in addition to changing the radiation angles from θ_c to θ_e. The retarded source coordinate defines the position of the source when it emitted the sound sensed at the microphone station. Thus, conversion of the data to this coordinate system would represent the sound pressure level measured with the microphone fixed and the source moving at speed, M, in figure 13. The Galilean transformation which results in the source moving also results in a zero open jet velocity.

The ray path angles linking the present and retarded coordinates are given by the frequency independent equation

$$\cos \theta_e = \cos \theta_c \sqrt{1 - M^2 \sin^2 \theta_c} - M \sin^2 \theta_c \qquad (60)$$

In addition to converting to the retarded source angles a sound pressure level correction was applied to the data. Measured sound pressure levels were converted from the sideline location (point D in fig. 13) to a common source radius in the retarded coordinate system given by r_e = 3 m. The correction was determined from the equation

$$\Delta SPL = 10 \log_{10} \left(\frac{y_1}{r_e \sin \theta_c} \right) \tag{61}$$

A Doppler shift was not included in the transformed data since the theoretical predictions of trailing edge noise for the isolated airfoil test conditions did not include this effect. The resulting angle and amplitude changes between the measured data and the retarded frame of reference are summarized in Table II.

After correcting for refraction effects, converting to retarded source coordinates, and correcting for the directional microphone resolution and gain characteristics, the 1/3 octave band sound pressure levels associated with each test condition were plotted as a function of Strouhal number. In this case the Strouhal number was based on the parameter $St = f\ \delta/U_o$. Here, the length scale parameter, δ, is determined from $\delta = \delta_i/1.07$ where δ_i corresponds to the average of the measured intermittency interface distance presented previously in figure 19. The frequency, f, corresponds to the 1/3 octave band center frequency and the velocity, U, corresponds to the freestream velocity of the open jet test section.

EXPERIMENTAL ASSESSMENT OF TRAILING EDGE NOISE RADIATION FROM A TWO-DIMENSIONAL AIRFOIL SECTION

Objective

The objective of this phase of the study was to experimentally assess the noise generated by a turbulent boundary layer flowing over the trailing edge of an airfoil. Tests conducted over a range of Mach numbers, airfoil angles of attack, and directivity angles were used to assess the dependence of the trailing edge noise on these physical parameters. Conclusions obtained from this assessment were used to develop a scaling law based on the different physical parameters. Included in the data base used to assess the scaling law were the trailing edge noise measurements reported by previous investigators in references 5 and 10. These different experimental studies provided data with widely varying freestream Mach number, airfoil chord, and airfoil profile values, thereby generalizing the scaling law applicability. The experimental measurements cited in references 5 and 10 were also compared to the fundamental analytical approach described in the section titled Theoretical Formulation of the Trailing Edge Noise Mechanism. This provided a preliminary evaluation of the accuracy of the theoretical prediction procedure. A detailed assessment is presented in the following section titled Trailing Edge Noise Predictions.

Angle-of-Attack Assessment

Approach - The effect of angle of attack on airfoil trailing edge noise was assessed by comparing acoustic spectra for different values of α. Comparisons were obtained over a range of Mach numbers as angle of attack varied from $\alpha = -0.4°$ to $12°$. All spectra corresponded to a fixed radiation angle of $\theta_c = 70°$. When transformed to retarded coordinates, the radiation angle, θ_e, varied with Mach number according to equation (60). Angle θ_e is indicated in each data set. Note that the spectra have been converted to the acoustic radiation from a unit length (1 ft or 0.33 m) of the airfoil.

Prior to evaluating the experimental results, a brief discussion of the spectrum measurement range is needed. Due to the lack of data points at low Strouhal numbers, it was not possible to identify the trailing edge noise spectrum peak (see, for example, fig. 21). This limitation occurred because of the low signal-to-noise ratio for directional microphone measurements at frequencies below 1.25 kHz. In this range, the reflector gain was too small to raise the trailing edge noise level above the facility background noise which radiates directly to the focal point microphone. Also, the large depth of field at low frequencies resulted in the reflector sensing the open jet shear

layer noise. Despite these limitations to measuring the complete acoustic spectrum, the experimental data obtained from the present study was sufficient to isolate the parametric dependence of trailing edge noise. This will become apparent in the following discussions. Also plotting the data in a normalized format, as is done in the section titled Generalized Scaling Law, shows that the lowest measured Strouhal numbers approached the spectrum peak in most cases.

Experimental Results - The general trend in figure 21 shows an increasing sound pressure level in the low Strouhal number range as the airfoil angle of attack increases. This dependence can be explained by the change in the boundary layer thickness on the suction side of the airfoil. As angle of attack increases, the adverse pressure gradient on the suction side creates a thicker boundary layer (see, for example, fig. 17). Since turbulent eddy size scales with the boundary layer thickness, increasing α creates larger eddies on the suction side of the airfoil. The presence of these large eddies results in a boundary layer pressure spectrum dominated by low frequencies which in turn increased the low frequency acoustic radiation.

The above physical explanation is substantiated by the flat plate turbulent boundary layer wall pressure fluctuation study by Schloemer (ref. 49). The tests were conducted with zero, adverse, and favorable pressure gradients. The results indicated that the effect of an adverse pressure gradient on the nondimensionalized wall pressure spectral density is to increase the low frequency content without influencing the high frequency portion appreciably. In contrast, a favorable pressure gradient creates a sharp decrease in the spectrum at high frequencies. Since the turbulent boundary layer pressure spectrum controls the acoustic radiation, similar trends would be expected in the acoustic far field.

Indeed, the data in figure 21 demonstrates an increase in low frequency acoustic energy, thereby, verifying the postulated link between boundary layer thickness and spectrum content. At high frequencies the expected decrease in sound pressure level did not occur. Instead, in the mid-frequency range, the noise levels remained constant. One possible explanation is that changes in the suction side and pressure side boundary layers compensated each other in the mid-frequency range, given by $St \sim 0.8$. For even higher Strouhal numbers, a different explanation is, however, needed. Now an increase in angle of attack also increases the noise radiation (see, for example, figs. 21(b) and 21(c)). These changes, which occurred mainly for $M \leq 0.3$, are presently not understood. Fortunately, the high frequency portion of the spectrum generated at the full-scale Reynolds number operating conditions tested here, would not be audible ($f \geq 20$ kHz). Thus, it was not critical to understand the observed changes. These changes were, however, considered to be due to a different source mechanism since the spectrum changes were centered near $St = 3$ as shown by figure 29(c). This Strouhal value is approximately a factor of 10 above the value associated with the trailing edge noise mechanism.

One noise mechanism which was evaluated as a possible explanation for the high frequency anomaly in figure 29(c) was vortex shedding due to the bluntness of the airfoil trailing edge. Assigning a Strouhal number of 0.2 to this mechanism and using the source frequency associated with the center frequency of the hump (f = 31.5 kHz in fig. 21(c)) provided a calculated dimension of 0.065 cm. This dimension is of the same order of magnitude as the airfoil trailing edge thickness which is 0.038 cm. Blunt body vortex shedding is therefore, a possible mechanism responsible for the high frequency portion of the spectra in figure 21.

Directivity Assessment

Approach - Directivity patterns were evaluated in the overhead plane at specific Strouhal numbers for various angles of attack and open jet Mach numbers. Sound pressure levels were normalized by the level measured at a specified retarded angle. The value of θ_e selected to normalize the data was close to 90° in each case. Theoretical directivity curves were also normalized by the same reference angle.

Evaluating the directivity pattern for various Strouhal numbers provided several advantages compared to the standard method of using the overall sound pressure level (OASPL). First, it permitted evaluating the directivity dependence on Strouhal number. Second, it permitted selecting the segment of the spectrum responsible for trailing edge noise while rejecting the noise postulated to be due to the vortex shedding source mechanism described in the previous subsection. Finally, the directivity dependence could be assessed despite the inability to determine OASPL values due to the limitations in the spectrum measurement range.

Directivity measurements were referenced to the open jet centerline which was within -0.4° of the airfoil chord line at zero lift conditions. The small changes in airfoil orientation due to increasing angle of attack were not included in the data reduction. The resulting error was small due to the slow variation in the radiation field with θ_e for the angular range investigated here. At most, the error was equivalent to 0.75 dB at the highest Mach number of M = 0.5.

Experimental Results and Comparison with Present Theory - Data showing the directivity pattern for various Strouhal numbers are shown in figure 22 for a range of velocities with α = -0.4°. The measurements show little difference in the directivity shape for Strouhal numbers below St = 1.0. The similarity of the data curves indicates that the directivity pattern is independent of Strouhal number.

The effect of angle of attack is determined by comparing the $\alpha = 0.4°$ case in figure 22(b) with the $\alpha = 7.6°$ case in figure 23. For the limited angular range available in figure 23, the directivity pattern is approximately similar to the measurement at zero lift coefficient. This constant shape of the radiation field indicates that the directivity pattern is independent of angle of attack.

Also shown in figures 22 and 23 is the analytical trailing edge noise directivity pattern determined from equation (32) of the present study. This radiation pattern, which is independent of Strouhal number, was normalized to the same retarded angle as used in the experimental data analysis. It is seen that the measured sound field agrees with the predicted shape to within 1 dB in most cases.

Mach Number Assessment

Approach - Mach number scaling laws were assessed experimentally using 1/3 octave band spectra like those shown in figure 24. Sound pressure levels measured at a fixed Strouhal number were plotted as a function of increasing Mach number. The influence of angle of attack was also evaluated by comparing the Mach number dependence at $\alpha = -0.4°$ and 7.6°. At each Mach number the sound pressure level plotted for a specified Strouhal number represented the 1/3 octave band measurement at the Strouhal number closest to the specified value. This occurred because the fixed 1/3 octave bands in the spectrum analyzer could not be expected to be centered at the precise frequency calculated from the Mach number and boundary layer thickness using the equation $f = St \cdot U/\delta_i$.

Since the directivity dependence was evaluated in the previous section, the present discussion will be limited to the Mach number dependence at a single retarded angle of $\theta_e = 98°$. This was considered close to $\theta_e = 90°$ where the directivity function is independent of Mach number. The value of $\theta_e = 98°$ was selected based on the availability of data at this angle for the Mach number of $M_o = 0.5$. Because measured data at lower Mach numbers was obtained at other angles (see Table II for θ_e values), it is necessary to introduce directivity corrections to convert the lower Mach number data to $\theta_e = 98°$. All corrections were based on the theoretical directivity patterns.

Experimental Results - Figure 24(a) shows the variation of sound pressure level versus Mach number for a range of frequencies with angle of attack set at $\alpha = -0.4°$. Within the accuracy of the figure, the general trend shows good agreement with a velocity scaling law of M^5 (see solid lines in fig. 24(a)) for Strouhal numbers varying over a factor of approximately 10. Note that low Strouhal number data for the case of $M_o = 0.1$ was not available due to the frequency limitations of the original data.

Increasing the airfoil angle of attack to $\alpha = 7.6°$ in figure 24(b) continued to give good agreement with the M^5 scaling law. From this it can be concluded that at each angle of attack the Mach number dependence is the same. Of course, the absolute value of the measured sound pressure level at a fixed Strouhal number continues to be a function of both α and M. This dependence is demonstrated by the change in spectrum shape and absolute amplitude as angle of attack and Mach number varied in figure 21.

The above described M^5 sound pressure level dependence agrees with the theoretical analysis of the present study. This is verified in the section titled Trailing Edge Noise Predictions.

Comparison with Previous Investigators

Experimental and theoretical results of the present study can be compared with the results of previous investigators. The following subsection concentrates on the angle of attack, directivity, and Mach number dependence. Comparison of the measured acoustic spectra with spectra reported by previous investigators are presented in the subsection titled Spectrum Shape Assessment. Finally, comparisons with existing scaling laws are given in the subsection titled Generalized Scaling Law.

Angle of Attack Dependence - The observed increase in sound pressure level at low Strouhal numbers as angle of attack increases agrees with the trends reported earlier by Schlinker in reference 5. The study by Brooks and Hodgson (ref. 10) also showed that angle of attack changes affect primarily the low Strouhal portion of the spectrum. Their results, however, showed a tendency for the spectrum peak to shift to lower frequencies in addition to experiencing a small decrease in the 1/3 octave band sound pressure level.

Brooks and Hodgson also observed a distinct peak in their acoustic spectra at high frequencies similar to the trend in figure 21(c). Their experiment was able to demonstrate that this additive contribution to the spectrum was generated by vortex shedding due to the airfoil trailing edge bluntness. By increasing the ratio of the trailing edge thickness, T, to boundary layer displacement thickness, δ^*, from $T/\delta^* = 0$ and $T/\delta^* = 0.28$, the hump was seen to increase in amplitude.

Directivity Dependence - The analytical directivity pattern described by equation (32) of the present study can be compared with the shape predicted by the theory of Howe (ref. 11). If the Kutta condition is applied at the airfoil trailing edge and the wake convection velocity parameter is assumed equal to the turbulent boundary layer convection velocity, the theory of Howe gives the same directivity shape as equation (32). If, however, the wake

convection velocity in the theory of Howe is considered to be zero, as used by Brooks and Hodgson (eq. (31), ref. 10), then the analytical equation describing the directivity pattern is different from radiation field defined by equation (32) of the present study.

Although not specially formulated as theoretical study of airfoil trailing edge noise, the recent work of Goldstein (ref. 33) also provides directivity predictions. The objective of the study was to predict the radiation pattern associated with a turbulent shear flow at the edge of a semi-infinite plate. To obtain directivity information relevant to the present study required removal of the refraction affects which were included in the analysis of reference 33. Correcting for shear layer refraction using the approach developed by Amiet (ref. 34) resulted in an analytical expression identical to equation (32) of the present study. The similarity with the analysis of Goldstein occurred only for the high frequency (or high Strouhal number) solution. At low frequencies (low Strouhal number), wehre the acoustic wavelength in the analysis of Goldstein was equivalent to the transverse dimension of the shear flow, internal reflections by the shear layer complicated efforts to correct for the presence of the shear layer. In this case, the analysis of Goldstein could not be modified to permit comparison with the analysis in the present study.

With several different theoretical directivity patterns available in the literature, it is worthwhile to evaluate further the differences between them. A comparison of the directivity pattern obtained from equation (32) and the prediction of Brooks and Hodgson (eq. (31), ref. 10) is given in figure 25. The parameter, $\bar{D}(\theta_e, \pi/2)$, represents the directivity pattern variation with angle θ_e. In both cases the calculation for $\bar{D}(\theta_e, \pi/2)$ assumed a turbulent boundary layer convection velocity to freestream velocity ratio of 0.6. At a Mach number of $M_o = 0.2$, corresponding to the maximum operating condition tested in reference 10, figure 25(a), shows that the two analyses (curves 1 and 2) give almost identical results. Yet, the two analyses use different values for the wake convection velocity. The present study assumes that the wake velocity is equivalent to the freestream convection velocity while Brooks and Hodgson assign a value of zero to the wake velocity. Thus, good agreement between the predicted and experimental directivity patterns is insufficient to assess the value selected for the wake convection velocity.

At a higher Mach number of $M_o = 0.43$, corresponding to one of the test conditions evaluated in the present study, the source directivity patterns described by curves 1 and 2 show a different shape (fig. 25(b)). When the Mach number is increased further to $M_o = 0.86$, the differences between curves 1 and 2 becomes even larger, especially in the forward arc (fig. 25(c)). For example, at $\theta_e = 140°$, a difference of 10 dB exists. The above described differences between the present analysis and the prediction of Brooks and Hodgson

demonstrates the need for experimental assessment of the trailing edge noise directivity pattern at high Mach numbers. Direct verification using isolated airfoils is presently not available.

Mach Number Dependence - Mach number to the fifth power scaling laws were obtained by several previous investigators. Brooks and Hodgson (ref. 10) measured an OASPL dependence of $M^{5.07}$. Schlinker (ref. 5) also observed a fifth power dependence for the maximum sound pressure level in the acoustic spectrum. Both of these studies employed isolated airfoils. A similar velocity dependence was observed in previous investigations of airframe noise. Fink (refs. 6 and 7) reported a fifth power velocity dependence for aerodynamically clean conventional low speed aircraft, jet aircraft, and sailplanes.

Spectrum Shape Assessment

Objectives - The first objective of this phase of the study was to determine if there exists a universal spectrum shape defining the trailing edge noise radiation. A second objective was to identify the Strouhal number associated with the spectrum peak. Recall that the present study was unable to measure the low frequency portion of the spectrum so that the spectrum peak could not be isolated. This limitation was overcome by including in the spectrum shape evaluation data sources which clearly identified the spectrum peak. These data included the previous reported isolated airfoil measurements of Schlinker (ref. 5) and Brooks and Hodgson (ref. 10). If it could be demonstrated that these different measurements collapse onto a single curve, then the Strouhal number of the spectrum peak could be determined.

Approach - Acoustic spectra presented here are limited to a single retarded angle of θ_e near 90°. In addition, spectrum measurements will be limited to $\alpha \sim 6°$ angle-of-attack results. This is because helicopter rotors operate at a finite angle of attack. Zero lift coefficient measurements were discussed earlier only to provide a complete evaluation of the trailing edge noise dependence on angle-of-attack.

Frequency information in this section of the report continues to be presented in terms of a nondimensional Strouhal number. As discussed in the section titled Airfoil Boundary Layer Characteristics, δ is the appropriate length scale to use in the Strouhal number parameter. Using measurements reported by previous investigators to check for a universal spectrum shape, therefore, required estimating δ for each study. This was necessary because the data reported by Schlinker (ref. 5) did not provide direct measurements of the boundary layer thickness. Brooks and Hodgson (ref. 10) presented their data in terms of a Strouhal number based on the displacement thickness which the authors determined from measured velocity profiles. A direct measurement

of δ was not available possibly due to the asymptotic shape of their velocity profile near the edge of the boundary layer. Detailed discussions of the procedures used to predict δ in each of the above studies are given in Appendix D. Tables III and IV list the average values of δ calculated in each case.

Figure 26 shows the measured trailing edge noise sound pressure levels obtained from the present study for $\alpha = 7.6°$ angle of attack. The spectra were measured at different retarded angles but were not converted to a common retarded angle. This was, however, done when the spectra were normalized to check for the existence of a scaling law. Note that all acoustic spectra represent the acoustic radiation from a unit length (1 ft or 0.3 m) of the airfoil.

Figures 27 and 28 present the acoustic spectra measured by previous investigators. Frequency information in each case is given in terms of a Strouhal number based on the boundary layer thickness values listed in Tables III and IV. These spectra represent trailing edge noise measurements from airfoil geometries and chord lengths different from the present study. The following discussion develops the scaling law and tests it against the different data sources.

Scaling Law Development - Dependence of trailing edge noise on Mach number and directivity were assessed in the previous subsections. Comparisons between theory and experiment indicated that the velocity dependence can be modeled as M^5 or as U^5 for incompressible flow. In addition, the noise directivity pattern can be represented by equation (32) in the plane normal to the airfoil model. However, the influence of airfoil profile shape and angle of attack have not yet been quantified. These parameters are considered to influence the noise indirectly by altering the turbulent boundary layer thickness at the airfoil trailing edge.

Noise dependence on boundary layer thickness was modeled as a linear function of δ. A linear dependence on δ also follows from the theoretical trailing edge noise formulation. Since δ is proportional to δ^* for the flat plate geometry used in the theoretical derivation, δ^* can be replaced by δ.

The theoretical dependence on δ will become more explicit in the next section titled Trailing Edge Noise Predictions. There the high frequency limit of equation (21) will be derived to show the dependence on δ as well as the other physical parameters. The resulting expression guided the selection of the specific parametric dependence for use in the scaling law. It should be noted that the linear dependence on δ agrees with the derivation of Ffowcs Williams and Hall (ref. 16) in addition to the analysis of Howe (eq. (7), ref. 11).

Based on the above arguments for the parametric dependence on M, $\bar{D}$ and δ, the overall sound pressure level for a two-dimensional isolated airfoil section is given by

$$\overline{p^2} \propto U^5 \bar{D} \frac{\delta s}{r_e^2} \tag{62}$$

Here the parameter s defines the airfoil span and r_e represents the acoustic source-to-microphone distance in the retarded coordinate system. In logarithmic form the above equation becomes

$$\text{OASPL} = 50 \log_{10} \frac{U}{100} + 10 \log_{10} \frac{\delta s}{r_e^2} + 10 \log_{10} \bar{D} + K_1 , \qquad U \text{ in knots} \tag{63}$$

where K_1 is the unknown constant of proportionality. A reference velocity of 100 knots was selected for the velocity scaling term to permit comparing the value of K_1 obtained from the present study with the value previously determined in the airframe noise study by Fink (refs. 6 and 7). For this reason the velocity in equation (63) must be in terms of knots. Note that equations (62) and (63) apply to an airfoil with zero sweepback angle at the trailing edge.

If a universal spectrum exists then the OASPL and 1/3 octave band sound pressure level are related by a Strouhal dependent function where

$$\text{SPL}_{1/3} = \text{OASPL} + F_1(\text{St}) \tag{64}$$

Here, the parameter SPL represents the 1/3 octave band sound pressure level in dB and F_1 describes the spectrum shape. Solving equations (63) and (64) for the SPL dependence gives

$$\text{SPL}_{1/3} = 50 \log_{10} \frac{U}{100} + 10 \log_{10} \frac{\delta s}{r_e^2} + 10 \log_{10} \bar{D} + F_1(\text{St}) + K_1 , \qquad U \text{ in knots} \tag{65}$$

Recognizing that $\bar{D} = 1$ at $\theta_e = 90°$, and isolating both $F_1(\text{St})$ and K_1 gives

$$F_1(\text{St}) + K_1 = \text{SPL}_{1/3} - 50 \log_{10} \frac{U}{100} - 10 \log_{10} \frac{\delta s}{r_e^2} , \qquad U \text{ in knots} \tag{66}$$

By subtracting the second and third terms on the right side of equation (66) from the different 1/3 octave band spectra in figures 26 to 28, the existence of a universal spectrum shape can be tested. If the resulting curves of $F_1(St) + K_1$ for each data set collapse on a single curve then the scaling laws in equations (64) and (65) will have been verified. Furthermore, the existence of a normalized spectrum shape will have been confirmed.

Normalized Spectra - Figure 29 shows the normalized acoustic spectra obtained from the present study. The normalization includes conversion of the spectra measured at different retarded angles in figure 26 to a common angle of $\theta_e = 90°$ where the directivity function, $\bar{D}$, is unity. Theoretical directivity calculations were used for the data conversion.

Trailing edge noise spectra in figure 29 tend to collapse onto a single curve when normalized by the parameters on the right side of equation (66). Although a definite spectrum peak cannot be determined from the data shown here, the curve suggests that the peak is near St = 0.1. This is similar to the value of St = 0.1 determined by Fink (refs. 6 and 7) in the study of trailing edge noise generated by fullscale clean airframe configurations.

Normalized acoustic spectra obtained from the earlier data reported by Schlinker are shown in figure 30. The data collapses onto a single curve with the spectrum peak occurring near St = 0.1. Values of the parameters used in the normalization are given in Table III.

Figure 31 shows the normalized acoustic spectra obtained from the data reported by Brooks and Hodgson for $\alpha = 5°$. The spectrum peak in figure 31 occurs near St = 0.14 which is close to the Strouhal peak suggested by figures 29 and 30.

A table of the peak Strouhal numbers associated with the different data sources described above gives

Investigators	Peak St Value Based on δ
Present Study	0.1
Brooks and Hodgson	0.14
Schlinker	0.1

Based on the tabulated values the Strouhal peak associated with trailing edge noise lies between St = 0.1 and 0.14. This is consistent with the value of St = 0.1 obtained from the clean airframe trailing edge noise studies of Fink (refs. 6 and 7) but differs from the value reported by Brooks and Hodgson

(ref. 10). Their study based the Strouhal number on the measured value of δ^* instead of δ as in the above tabulation. Their range of peak Strouhal number values was close to the values tabulated above with $St(\delta^*)$ varying from 0.07 to 0.1. Here $St(\delta^*)$ designates a Strouhal value based on δ^*. It is not clear why the Strouhal values would be similar when δ^* is significantly smaller. It is possible that the value of δ^* was too large as discussed in Appendix D.

The measurements of Brooks and Hodgson can also be compared with the peak Strouhal value (based on δ^*) obtained from the study of Heller and Dobrzynski (ref. 8). The latter study presented far-field trailing edge noise spectra only as a function of frequency. However, the value of δ^* = 5 mm, presented in reference 8 to nondimensionalize the surface pressure spectra, can also be used to form a nondimensional Strouhal number for the far-field radiation. Based on the spectrum peak occurring at f = 200 Hz when U = 50 m/sec (see fig. 14, ref. 8), the peak Strouhal number becomes $St(\delta^*)$ = 0.02. This is approximately a factor of 4 to 5 smaller than the peak Strouhal value reported in reference 10.

The Strouhal peak associated with the measurements of Heller and Dobrzynski (ref. 8) agrees with the average value determined from the present study. If St = 0.11, based on the average value of δ, then using $\delta^* = \delta/8$, the Strouhal number based on displacment thickness is $St(\delta^*)$ = 0.014. This is similar to the value of $St(\delta^*)$ = 0.02 calculated for the study of Heller and Dobrzynski.

Generalized Scaling Law

Approach - The general conclusion from figures 29 to 31 is that for a given airfoil geometry, 1/3 octave band trailing edge noise spectra collapse onto approximately a single curve when normalized by the scaling law given in equation (66). It now remains to determine if the normalized spectra obtained from the different airfoil geometries can be represented by a single spectrum function, $F_1(St)$, and a constant, K_1. For this purpose, the spectra in figures 29 to 31 were plotted on the same graph as shown in figure 32. Only selected spectra are shown to avoid crowding the data.

Development of Equation - The success of normalizing the spectra from different airfoil geometries demonstrates that there exists a universal trailing edge noise spectrum. To quantify the spectrum for noise predictions requires analytically describing the functional form for $F_1(St)$. This can be achieved by fitting an equation to the nondimensional spectrum such as the solid solid line in figure 32. In this case, the analytical equation corresponds to the function presented by Fink in reference 6 and 7 for full-scale airframe trailing edge noise. The function is currently used in the NASA ANOPP Total Aircraft Analysis. The equation describing the relationship between 1/3 octave band sound pressure levels and the overall sound pressure level is

$$F_1(f) = SPL_{1/3} - OASPL = 10 \log_{10} \left\{ 0.613 \left(\frac{f}{f_{max}} \right)^4 \left[\left(\frac{f}{f_{max}} \right)^{3/2} + 0.5 \right]^{-4} \right\} \qquad (67)$$

where f_{MAX} is the frequency associated with the spectrum peak. Replacing frequency by Strouhal number gives the solid line in figure 32. In this case, $St_{MAX} = 0.1$ was selected based on the average peak Strouhal value determined from the different data sources described in the table in the previous subsection. In addition, a value of $St_{MAX} = 0.1$ provided the best agreement with the data points in figure 32.

It now remains to determine the relationship between the spectrum shape and the absolute sound pressure level. The link between these parameters is controlled by the unknown constant, K_1, in equation (66). Based on the decibel level corresponding to the value at the maximum of the solid line shown in figure 32, $F_1(St = 0.1) + K_1 = 84.0$. But $F_1(St = 0.1) = -9.16$ dB in equation (67). Thus, $K_1 = 93.2$ dB.

The final equations for predicting both overall sound pressure levels and 1/3 octave band sound pressure levels are then

$$OASPL = 50 \log_{10} \frac{U}{100} + 10 \log_{10} \frac{\delta S}{r_e^2} + 10 \log_{10} \bar{D} + K_1, \qquad K_1 = 93.2, \ U \text{ in knots} \qquad (68)$$

and

$$SPL_{1/3} = OASPL + 10 \log_{10} \left\{ 0.613 \left(\frac{St}{St_{max}} \right)^4 \left[\left(\frac{St}{St_{max}} \right)^{3/2} + 0.5 \right]^{-4} \right\} \qquad (69)$$

Here $St_{MAX} = 0.1$.

Effects of directivity have been included in equation (68) to generalize the results for application to all radiation angles. It should be emphasized that the constant, K_1, was determined from various isolated airfoil data sets with the airfoils at a finite angle of attack ($\alpha \approx 6°$). Thus, in the strictest sense, the above equations cannot be applied to the $\alpha = 0°$ test conditions. Fortunately, changes in angle of attack can be accounted for by introducing the correct value of δ, as shown by the good collapse of data in figure 21. Equation (68), therefore, is a general equation.

Comparison With Existing Scaling Law - The above formulation can now be compared to the equations developed by Fink (refs. 6 and 7) to predict airframe trailing edge noise. The functional dependence on M, δ, and St is

identical to the formulation given by Fink. However, the directivity function used by Fink for a wing with zero sweep-back angle was different from that given by equation (32). Fink proposed that

$$D\left(\theta_e, \frac{\pi}{2}\right) = \cos^2(\theta_e/2) \tag{70}$$

Here θ_e is the angle between the flight path and the observer position measured from the approach direction. Recall that θ_e in the present study is measured from the opposite direction so that $\cos^2(\theta_e/2)$ in the above equation becomes $\sin^2(\theta_e/2)$. Thus, equation (70) is similar to the numerator of equation (32) but lacks the Mach number dependent terms. This is because the directivity pattern given by equation (70) represents a low Mach number result which was based on the early theory of Ffowcs Williams and Hall (ref. 16). In contrast the present study provides a general expression given by equation (32). This functional form included in the present scaling law, is considered to be the correct formulation for trailing edge noise.

Another difference between the present scaling law and the result of Fink becomes evident when comparing the value of the constant K_1. Equation (68) uses a value of $K_1 = 93.2$ dB while Fink reported a value of $K_1 = 101.5$ dB. The latter value is based on measurements using microphones on posts 1.2 m above the ground. Accounting for ground reflections, which cause measured levels to be approximately 3 dB above free-field conditions at high frequencies, results in $K_1 = 98.5$. Hence, the value of K_1 associated with the scaling law in references 6 and 7 was high by approximately 5 dB when compared to the present study. This difference was evident earlier when Schlinker compared his trailing edge noise measurements with the prediction developed by Fink. The comparisons reported in reference 5 indicated approximately a 4 dB difference between measured and predicted values.

TRAILING EDGE NOISE PREDICTIONS

Objective

Two different trailing edge noise prediction methods were developed in the previous sections of this report consisting of a fundamental theoretical approach with no adjustable constants and a scaling law approach based on experimental data. Each approach modeled the noise as radiating from a stationary two-dimensional isolated airfoil segment.

It now remains to assess the accuracy of the two prediction methods. Following this the stationary two-dimensional isolated airfoil formulation will be extended to the rotating coordinate system. Transformations described in the section titled Theoretical Formulation of the Trailing Edge Noise Mechanism will be used for this purpose. Sound pressure levels will be calculated and compared to specific full-scale helicopter test data.

Assessment of Isolated Airfoil Noise Prediction Procedures

Scaling Law Approach - It would appear that selecting values for St_{MAX} and K_1 based on experimental data removes any discrepancy between the scaling law prediction and experimental measurements. Supposedly this would provide an accurate scaling law method for predicting the trailing edge noise. The accuracy of the scaling law approach, however, is limited by how closely the initial data collapses onto a single curve. Although the solid line in figure 32 represents the average of the experimental data, the curve should be compared to the individual data sets used to generate this figure.

Figure 29 compares the scaling law with the experimental results of the present study. Measurements at Strouhal numbers below unity show reasonable agreement with the solid line representing equation (70). The Strouhal number associated with the spectrum peak is close to the value of $St_{MAX} = 0.1$

Data from the study of Schlinker (ref. 5) is compared to the scaling law in figure 30. Again the sound pressure levels are in good agreement with the measured values while the spectrum peak occurs near the value of St_{MAX} selected for the scaling law. Comparing the scaling law with the measurements of Brooks and Hodgson in figure 31 indicates a difference in Strouhal number associated with the spectrum peak. This difference was not apparent in figure 32 due to the heavy concentration of data points.

The detailed comparison available in figures 29, 30, and 31 emphasizes that the scaling law represents the average of the data points in figure 32 and specific data sets can be different from the average line. Such differences define the accuracy of the scaling law approach when compared to the isolated airfoil studies conducted by different investigators.

Theoretical Approach - Figure 33(a) compares the first principles trailing edge noise theory given by equations (21) and (22) with the measurements obtained from the present study. Note that the power spectral density formulation in equation 21 has been converted to one-third octave band form. Also the value of δ^* needed in equation (22) was determined from figure 19 using the flat plate boundary layer approximation $\delta^* = \delta/8 = \delta_i/(1.07)(8)$. Recall that the accuracy of modeling the flow field as a flat plate boundary layer was discussed earlier in the section titled Airfoil Boundary Layer Characteristics. Additional discussions are given in Appendix D.

A comparison of the predicted and measured spectra in figure 33(a) shows good agreement at high frequencies but poor agreement at low frequencies. A similar comparison with the narrowband spectra of Brooks and Hodgson, given in figure 34, also shows poor agreement. In the latter case the value of δ^* needed as an input to the present prediction was based on Table IV and the relationship $\delta^* = \delta/8$.

Predictions in figure 33(a) and 34 are based on a flat plate surface pressure field model with the spectrum shape, S_{qq}, given by equation (22). It was postulated that better agreement at low frequencies could be obtained by replacing the flat plate convecting surface pressure model with the pressure field existing at the trailing edge of an airfoil. Justification for this approach was based on the normalized surface pressure spectrum measurements of Yu (ref. 9) as well as Brooks and Hodgson (ref. 10). The experimental results obtained from reference 9 are plotted in figure 35(a) as a function of $\tilde{\omega}$ for two freestream velocities. These measurements correspond to an airfoil at zero degrees angle of attack. Also shown in the same figure is the normalized surface pressure spectrum for a flat plate given by equation 22.

Comparison of the airfoil and flat plate spectra in figure 35(a) indicates a definite difference in the spectrum shape and absolute level for these two geometries. Qualitatively, the fluctuating surface pressure spectrum near the airfoil trailing edge is seen to be about 7 dB higher than the zero pressure gradient flat plate result. This contrast is presented quantitatively in figure 35(b) where the abscissa represents the difference between the average of the airfoil data (see figure 35(a)) and the flat plate spectrum. Representing the difference function in figure 35(b) as DIFF ($\tilde{\omega}$) results in a modified expression for the surface pressure spectrum given by

$$S'_{qq}(\omega,0) = \left(\frac{1}{2}\rho_0 U^2\right)^2 \frac{\delta^*}{U}\left[2 \times 10^{-5} F(\tilde{\omega})\ DIFF(\tilde{\omega})\right] \qquad (71)$$

Applying S'_{qq} to the isolated airfoil noise prediction provides the modified theoretical prediction shown in figure 33(b) for trailing edge noise measurements conducted during the present study. A comparison of the modified theory and experiment now shows better agreement at low frequencies. In particular, predicted noise levels are within 3 dB of measured levels over most of the spectrum range from M = 0.1 to 0.5. The need to include the airfoil surface pressure spectrum has, therefore, been demonstrated.

A similar conclusion is obtained from figure 34 where the modified theory is compared to the measurements of Brooks and Hodgson. The improvement in the predicted sound pressure levels is evident when the circle and square symbols are compared at M = 0.2.

A final demonstration of the ability to calculate trailing edge noise radiation using the modified first principles theory is given in figure 36. Here the present analysis is compared to the data reported by Schlinker (ref. 5). Again the comparison between theory and experiment shows good agreement in absolute sound pressure levels.

Figure 34 also shows the trailing edge noise prediction calculated by Brooks and Hodgson for their own data. A brief discussion of the difference between their prediction and the present calculation is warranted. The prediction in reference 10, which is based on the measured surface pressure spectra and characteristic length scales, does not require a value of δ^* as an input. In contrast, the present approach uses an analytical model for the surface pressure characteristics and requires a knowledge of δ^* which is calculated from flat plate boundary layer theory. As noted in Appendix D, the calculated δ^* value differs from the measured value reported by Brooks and Hodgson by a factor of approximately 2.5. It is not clear which value should be used. However, Appendix D discusses the above described differences in δ^* and presents the reasons for using the value of δ^* obtained from flat plate boundary layer theory.

Modification of the first principles trailing edge noise theory focused on replacing the expression for S_{qq} on a flat plate with a measured airfoil surface pressure spectrum. A similar modification was considered for the spanwise length scale, ℓ_y, which is derived in equation (19) from the spanwise cross-spectrum $S_{qq}(\omega,y_o)$. Based on the comparisons of S_{qq} and S'_{qq} the functional form of the parameter, ℓ_y, would not be expected to be the same for an airfoil surface and a flat plate. However, Brooks and Hodgson showed that, indeed, the normalized airfoil and flat plate spectra are identical. Consequently, if was not necessary to alter the expression for ℓ_y and the flat

plate boundary layer length scale was considered to be representative of the flow field modeled here.

Comparison of Scaling Law and Theoretical Approach - It is worthwhile to compare the analytical and the scaling law approach for calculating trailing edge noise. For comparison purposes the theory will be simplified by removing the dependence on the ratio of acoustic wavelength to airfoil chord. Letting the ratio of chord-to-wave-length approach infinity, and letting $M_{ch} = M$ in the expression for $\mathcal{L}$ in equation (21) gives for the far-field narrow band sound pressure level

$$S_{pp}(\underline{x}, \omega) = \frac{M}{8\pi^2} \frac{S\ell_y}{r_e^2} \bar{D}(\theta_e, \phi) \; S'_{qq}(\omega, 0) \tag{72}$$

where $\bar{D}(\theta_e, \phi)$ is given by equation (32). Note that the modified surface pressure spectrum given by S'_{qq} in equation (71) has replaced the flat plate surface pressure spectrum term in equation (21).

Putting this in third octave form using equation (24) gives approximately

$$SPL_{1/3} = 10 \log_{10}\left[\left(\frac{U}{343.5\,m/sec}\right)^5 \frac{S\delta^*}{r_e^2} \bar{D}(\theta_e, \phi) F(\tilde{\omega}) DIFF(\tilde{\omega})\right] + 126.8 \quad 0.1 < \tilde{\omega} < 20 \tag{73}$$

where $F(\tilde{\omega})$ represents the frequency dependence given by equation (22b). Here the value K follows strictly from the theoretical noise model proposed and the values of the parameter S'_{qq} and ℓ_y obtained after assuming that surface pressures near the trailing edge can be modeled by equation (71) and (24). No adjustment of the value of K exists in equation (73). It should be noted that there is a factor of 8π difference between equations (72) and (73). This change occurs because a factor of 2 is needed to account for both sides of the airfoil, a second factor of 2π accounts for changing from an $\tilde{\omega}$ spectrum to a frequency spectrum, and an additional factor of 2 is needed to convert a two-sided spectrum ranging from $\tilde{\omega} = -\infty$ to $\tilde{\omega} = +\infty$ to a one-sided spectrum ranging from $\tilde{\omega} = 0$ to $\tilde{\omega} = +\infty$.

Before the above theoretical result can be compared to the scaling law equation it is necessary to convert the equation to a form similar to that given by equation (69). This requires replacing the Mach number dependence by velocity and letting $\delta^* = \delta/8$. Equation (73) then becomes

$$SPL_{1/3} = 50 \log_{10}\left(\frac{U}{100\,knots}\right) + 10 \log_{10}\left(\frac{\delta s}{r_e^2}\right) + 10 \log_{10}(\bar{D}) + 10 \log_{10}\left[F(\tilde{\omega}) DIFF(\tilde{\omega})\right] + K \tag{74}$$

$$0.1 < \tilde{\omega} < 20, \quad K = 76.6$$

Now the constant, K, contains the conversion which changes Mach number dependence to a velocity dependence in knots. The constant also contains the factor of 8 which links δ^* and δ.

For comparison to the above expression, equations (68) and (69) are combined into one similar equation which is

$$SPL_{1/3} = 50 \log_{10}\left(\frac{U}{100 \text{ knots}}\right) + 10 \log_{10} \frac{\delta s}{r_e^2} + 10 \log_{10}(\bar{D}) + 10 \log_{10}\left\{0.613 \left(\frac{St}{St_{max}}\right)^4 \left[\left(\frac{St}{St_{max}}\right)^{3/2} + 0.5\right]^{-4}\right\} + K_1 \quad (75)$$

where $K_1 = 93.2$.

The form of equations (74) and (75) now permit direct comparison. The parametric dependence on U, δ, and $\bar{D}$ (θ_e, ϕ) is similar. However, the peak value in addition to the frequency dependence appear to be different in each equation. These differences are best evaluated by isolating the frequency and amplitude dependent terms in a form similar to equation (66), thereby, permitting direct comparison of the normalized spectrum shape. The result is shown in figure 37 where the abscissa represents either:

a) for the first principles theory, F(St)DIFF(St)+K
b) for the scaling law, $F_1(St)+K_1$

Figure 37 shows that the spectrum peak amplitudes for the two prediction methods are approximately the same. However, the Strouhal numbers associated with each peak differ by a factor of two even though the spectrum shapes are similar (see shifted curve in figure 37). In the case of the scaling law the peak occurs at St = 0.1 while the theoretical result gives a value of approximately St = 0.2. This explains why the peak Strouhal number in the analytical prediction shown in figure 33(b) occurs near St = 0.2 while the scaling law (based on figure 32) peaks near St = 0.1.

Summary and Evaluation - The above discussions assessed the accuracy of the scaling law and theoretical approach for predicting trailing edge noise levels. Based on the comparisons between predictions and experiment both methods give approximately the same sound pressure level at the spectrum peak and predict approximately the same spectrum shape. However, the fundamental theory predicts a larger value for the Strouhal number associated with the spectrum peak. Thus, for the purpose of predicting trailing edge noise radiation from rotating blades the scaling law is considered presently to be the most reliable. This conclusion applies for a range of Mach numbers up to a maximum of M = 0.55. Furthermore, this result applies to Reynolds numbers representative of full-scale helicopter main rotor operating conditions.

For those cases in which the Mach number is above the highest value investigated here the fifth power Mach number scaling continues to be applicable. This follows from the fundamental theory which includes the compressibility effects occurring at high Mach numbers. Based on equation (72) $S_{pp} \alpha MU^4$. For a rotor operating in a constant atmospheric propagation speed given by c_o, $S_{pp} \alpha M^5$. Thus, the Mach number dependence is the same at low speeds and high speeds.

Trailing edge noise directivity dependence in the scaling law is also considered to remain the same at high rotor Mach numbers. This follows again from the theoretical directivity function which was incorporated directly into the scaling law. Similarly the spectrum shape is considered to remain unaltered based on the theoretical normalized spectrum. Recall that the analytical and empirical spectrum shapes given by F(St)·DIFF(St) and F_1(St) have approximately the same shape although they peak at a different Strouhal number (see Fig. 37).

There are two limitations to the applicability of the trailing edge noise prediction procedures developed here. The first requirement is that the airfoil section Mach number must be below the condition at which impulsive noise is generated due to locally supersonic flow. In this case the shock boundary layer interaction increases the trailing edge boundary layer thickness making the flat plate boundary layer calculation unreliable for determining the value of δ needed as an input to the scaling law. It should be noted that based on the scaling law dependence trailing edge broadband noise would increase significantly under this operating condition.

The second requirement applies to model noise tests and the location of the laminar to turbulent transition point on the airfoil. To simulate full scale trailing edge noise radiation it is required that turbulent boundary layer develop over a sufficient distance to ensure an equilibrium boundary layer at the airfoil trailing edge. Otherwise the surface pressure spectrum field convected over the trailing edge does not possess a universal spectrum shape and becomes a function of the turbulent flow distance on the airfoil surface. The above criterion is best satisfied by maintaining the same Reynolds number as that expected for a full scale geometry. The length scale in the Reynolds number calculation would be based on the distance from the transition point to the airfoil trailing edge.

It should be noted that differences between the present theoretical approach and the experimental results should not preclude further development and application of the theory. The analytical model of surface pressure spectra convecting past the airfoil trailing edge is basically correct and can be shown to be similar to the formulations of other investigators. The source of the difference in spectrum peak location is, therefore, not the acoustic source model but rather the surface pressure spectra data needed as

an input to the prediction. The lack of agreement can be traced to insufficient details in the surface pressure field description. Specifically, the pressure spectrum, S'_{qq}, is presently based on measurements obtained for an airfoil at $\alpha=0°$. Differences between the predicted and measured spectrum peak Strouhal number could possibly be removed by incorporating the influence of angle of attack on the surface pressure spectrum. Measurements of both Yu (ref. 9) as well as Brooks and Hodgson (ref. 10) have shown that increasing α increases the low frequency portion of the suction side surface pressure spectrum by approximately 3 dB. Conceptually this would increase the absolute sound pressure level of the low frequency side of the predicted spectrum in figure 37 sufficiently to shift the broad spectrum peak by the one octave in figure 37. This could result in total agreement of the first principles trailing edge noise theory with the experimental results.

Accurate predictions of the trailing edge noise mechanism may, therefore, require using measured surface pressure data obtained near the airfoil trailing edge. Such detailed measurements were conducted by Brooks and Hodgson at low Mach numbers ($M \leq 0.2$) to provide the necessary experimental input to their theoretical noise prediction. This approach should be extended to the higher Reynolds numbers associated with full-scale helicopter rotor operating conditions. If it can be demonstrated that the surface pressure data at higher Reynolds numbers continues to collapse onto a universal curve, then this curve could be used as a generalized input to the noise prediction.

Rotating Blade Noise Predictions

Approach - For the purpose of predicting trailing edge noise from rotating blades the scaling law was transformed to the rotating frame. The method employed assumed that the spectrum of a given blade segment is, at any particular instant, given by equation (75). The local relative velocity of the rotor blade segment determined the boundary layer details and the resulting noise spectrum. The 1/3 octave band spectrum shape, given by equation (75), was converted to a narrowband power spectral density expression by accounting for the filter bandwidth. The spectrum was permitted to vary as the rotor moved about the azimuth.

To obtain the final spectrum, the instantaneous spectrum was averaged around the azimuth, together with a weighting which accounted for retarded time effects. Details of the analysis were described earlier in the section titled Theoretical Formulation of the Trailing Edge Noise Mechanism.

Input to Noise Prediction - Equation 75 requires for each spanwise segment of the rotor blade a knowledge of a) the local freestream velocity, b) the average of the suction side and pressure side boundary layer thickness, and c) the observer position relative to the rotor plane. With the exception of

the boundary layer thickness, δ, the above variables are easily determined. To avoid using complicated computational fluid dynamics methods for determining δ this parameter was estimated using the flat plate boundary layer calculations. This approach was justified earlier by a comparison of the flat plate calculation with the average of the pressure and suction side values of δ for the rotor blade segment tested in the present study. The comparisons showed good agreement at small angles of attack (see fig. 19).

Recall that the differences between flat plate boundary layer theory and experiment were less than 20 percent. Based on the trailing edge noise scaling law the estimated difference in noise radiation would be less than 0.8 dB. This statement imples that helicopter rotor trailing edge noise predictions based on flat plate boundary layer characteristics are accurate within several decibels. Greater accuracy, and therefore, detailed boundary layer information, was not required since the objective of the study was to assess the relative importance of this noise mechanism compared to the other operative mechanisms on a full scale helicopter.

Since the abrasion strip on full scale helicopter rotors is known to trip the surface boundary layer close to the blade leading edge the flat plate boundary layer calculation was initiated at the blade leading edge. This is expected to introduce only a small error in the calculation of δ.

Test Case - The trailing edge noise prediction method was tested against data measured during a full-scale helicopter noise flyover. Details of the helicopter main rotor and tail rotor are tabulated below.

	Main Rotor	Tail Rotor
Number of Blades	4	4
Rotor Radius	6.7 m	1.2 m
Blade Chord	0.4 m	.17 m
Rotor Rotation Rate	307 rpm	1689 rpm

The main rotor blade geometry was identical to the rotor blade segment tested during the two-dimensional isolated airfoil investigation conducted in the present study.

Data presented here correspond to a level flyover condition of 36 or 72 m/sec and an altitude of 76 m. Acoustic spectra were processed when the helicopter was in approximately an overhead position so that $\theta_e = 90°$. Data was obtained using microphones on posts 1.2 m above the ground. To account for the ground reflection effect 3 dB were added to the free field trailing edge noise prediction. Weather conditions during the helicopter flyover are tabulated below.

Wind speed - zero velocity (calm)
Temperature - 77°F
Relative Humidity - 90%

The effect of atmospheric attenuation due to humidity was accounted for by applying a correction to the measured data.

Figure 38 shows the narrowband (12.5 Hz bandwidth) total helicopter noise spectrum measured during the flyover. Corrections for ground reflections and atmospheric attenuation have not been applied here. The objective of presenting this figure is to demonstrate that the flyover signature is mainly broadband noise above 1 KHz. Apparent discrete tone peaks in the spectrum are due only to the short averaging time (1/2 sec) used during the spectrum analysis. Although a longer averaging time would have provided a smoother spectrum, spatial directivity information would then be averaged. For example, the 1/2 second averaging time employed in the above described measurements resulted in averaging angular information within $\pm$ 11° about the 90° overhead position during the 72 m/sec flyover. Fortunately, directivity information varied slowly at this angle as shown by the three different spectra superimposed on figure 38. Each spectrum represents the output from a 1/2 sec spectrum analysis obtained during the flyover. One spectrum corresponds to the 90° overhead position while the other two spectra represent the preceeding and following spectra.

Figure 39(a) shows the same flyover condition measured with a narrowband spectrum in figure 38 converted to 1/3 octave band analyzer (circle symbol). The square symbol in figure 39(a) represents the same data with the atmospheric attenuation correction added to the measurement. Additional corrections to account for the Doppler shift and retarded source position were not necessary in the overhead position.

Also shown in figure 39(a) is the scaling law prediction for the helicopter main rotor trailing edge noise. Comparison of the total helicopter noise spectrum and the trailing edge noise spectrum demonstrates that at high frequencies trailing edge noise can be a significant noise mechanism. In fact, at some frequencies predicted and measured noise levels are almost identical. Below 2 KHz other broadband noise mechanisms begin to dominate over the trailing edge noise as shown by the divergence of the predicted and measured curves.

Figure 39(b) shows a second measured spectrum at a different flyover speed. Again the comparison between predicted 1/3 octave band levels and measured spectra is good.

Also presented in figure 39 is the first principles prediction for the main rotor tailing edge noise. The spectrum peak amplitude is close to the measured levels although the frequency associated with the peak occurs at a value about the dominant portion of the measured broadband noise spectrum.

This latter feature was expected from the comparison of the scaling law and the first principles trailing edge noise predictions in figure 37. It is felt, however, that further development of the airfoil surface pressure spectrum model will provide better agreement with measured data.

A comparison of the predicted trailing edge noise for the helicopter main rotor and the measured total helicopter noise spectrum has been presented in figure 39. Although noise from the tail rotor was also present this contribution was expected to be weak. This is due to the smaller boundary layer thickness and rotor span values which are linear inputs to the analysis according to equation (75). Also, the smaller boundary layer thickness on the tail rotor causes the spectrum peak to shift to a higher Strouhal number.

Summary and Evaluation - The importance of the helicopter trailing edge noise mechanism has been verified by direct calculation of the associated noise levels during an aircraft flyover. Predicted noise levels close to the total helicopter noise spectrum demonstrate that trailing edge noise must be accounted for in future noise prediction procedures.

Since trailing edge noise is controlled by the inherent characteristics of the rotor blade boundary layer, it is difficult to eliminate this noise mechanism. Delaying the boundary layer transition to reduce δ in equation (75) is a possibility but the benefits are marginal due to the linear dependency on boundary layer thickness. Efforts to shift the blade surface pressure spectrum to a higher frequency to increase atmospheric attenuation represents a possible but difficult task of controlling details of the turbulent boundary layer pressure spectrum.

The reduction of helicopter rotor trailing edge noise is, therefore, limited to changes in the aerodynamic operating conditions. As suggested by the prediction methods presented here, a reduction of tip speed would provide the greatest improvement. Reduced speeds would, presumably, require increasing the number of rotor blades to maintain a constant rotor thrust. The resulting increase in trailing edge noise would, however, be less than the decrease achieved by changing the tip speed.

With the exception of the above described noise reductions, trailing edge noise represents the limiting acoustic source mechanism for the total helicopter noise spectrum. This conclusion is similar to the conclusions obtained in previous studies of the noise generated by fixed wing aircraft. This noise, referred to as "airframe noise", has set the noise limit for such aircraft. Based on the results of the present study, a similar noise limit exists for helicopter rotor broadband noise.

Reductions in high frequency helicopter broadband noise have also been achieved by changing the rotor blade tip shape. The source mechanism,in this case,is not the attached boundary layer trailing edge noise investigated in the present study. Instead, the noise is generated by convection of the three dimensional tip vortex flow field over the blade trailing edge. George (ref. 50) provided an approximate model of the noise generated by this separated and highly turbulent flow field as it convects over an airfoil trailing edge. His predictions indicated that blade tip vortex noise can be comparable to trailing edge noise. This result explains the broadband noise reduction observed by some investigators after changing the airfoil tip shape.

CONCLUSIONS AND RECOMMENDATIONS

A. Full-Scale Rotor Noise

A.1. Extension of a validated isolated airfoil trailing edge noise scaling law to the rotating blade case demonstrated that trailing edge noise from a full-scale helicopter contributes significantly to the total broadband noise spectrum at high frequencies. This noise mechanism is expected to control the minimum rotor noise level.

A.2. The helicopter rotor trailing edge noise scaling law for subsonic tip speeds was validated using two-dimensional isolated airfoil results at full-scale Reynolds numbers. Knowledge of the helicopter altitude, speed, angular position, rotor tip speed, blade number, rotor chord and span, and rotor boundary layer thickness are the only parameters required in the analysis. Based on two-dimensional isolated airfoil results, helicopter rotor boundary layer thickness can be estimated using a flat plate turbulent boundary layer calculation. This simplifies the flow field details needed as an input to the prediction procedure.

A.3. A first principle theory for trailing edge noise predicts the correct absolute sound pressure level but does not predict the Strouhal value identifying the spectrum peak. The basic noise model of a frozen pressure pattern convecting past a trailing edge, however, agrees with the acoustic source models developed by other investigators. Differences between theory and experiment are believed to be due to the airfoil fluctuating surface pressure field model used as an input to the analysis. Accurate predictions require using measured surface pressure data obtained near the airfoil trailing edge.

A.4 Future efforts should be directed toward detailed airfoil surface pressure measurements at Reynolds number representative of full scale helicopter operating conditions. If it can be demonstrated that the surface pressure spectra data at high Reynolds numbers collapse onto a single nondimensional curve, then this curve can be used as an input to the noise prediction.

B. Trailing Edge Noise From a Local Blade Segment

B.1. Based on two-dimensional airfoil results, trailing edge noise radiation patterns from a local blade segment are well predicted by the theory developed in the present study. Directivity patterns are independent of angle of attack and acoustic source Strouhal number.

B.2. Noise dependence on local section Mach number varies as M^5 and is independent of angle of attack and acoustic source Strouhal number.

B.3. Local rotor blade angle of attack influences only the low Strouhal number portion of the spectrum. Increasing angle of attack increases sound pressure level by only a few decibels near the spectrum peak. The observed trend is explained by the increase in boundary layer thickness on the suction side of the airfoil.

B.4. Trailing edge noise 1/3 octave band spectra from a local blade segment can be approximated by a universal spectrum shape. A scaling law capable of predicting the absolute spectrum levels depends only on Mach number, boundary layer thickness, and observer location.

B.5. Boundary layer thickness input data to the scaling law can be estimated using flat plate turbulent boundary layer calculations. Such calculations approximate the average value of the pressure side and suction side boundary layers. The average value controls the peak Strouhal number of the universal spectrum curve.

APPENDIX A

Directional Microphone System

Directional Sensitivity and Spatial Resolution - Although the directional microphone system is most sensitive to sources located on its aiming axis, it does sense sources at off axis directions defined by the angle ϕ_o in figure 12. The response of the system to such off axis sources is controlled by diffraction at the circular aperture of the reflector. For the present geometry the diffraction phenomenon is governed by the nondimensional parameter $\eta = (\pi D f \sin\phi_o)/c_o$ where D is the reflector aperture, f is the acoustic frequency, and c_o is the sound speed. Figure 40 shows the measured normalized response from the focal point microphone plotted as a function of η. The response function, H, decreases as ϕ_o increases demonstrating the decrease in sensitivity to off-axis angles. This response, often referred to as the spatial discrimination capability, has been shown to agree with the Fraunhofer diffraction pattern for a circular aperture system (see Fig. 40). Such agreement permitted using an analytical expression for the response function in the data reduction.

Figure 40 demonstrates that diffraction causes the system to have a finite spatial resolution instead of the ideal delta function resolution. Thus, while the system is most sensitive to sources located on its aiming axis, it does sense sources at off axis directions. The "sharpness" of the resolution, however, increases with the acoustic frequency, f, which appears in the numerator of the parameter, η. Thus, for a fixed off-axis source position defined by ϕ_o, the response H decreases as f increases.

One parameter which quantifies the directional microphone frequency dependent spatial discrimination is the diffraction pattern half-width, ΔW. The half-width, defined as the spatial distance between the negative 3 dB points in the diffraction pattern of figure 40 corresponds to the points $\eta = \pm 1.66$. A 3 dB decrease in sensitivity to off-axis sources, therefore, occurs for displacements given by $x = 1.66\, c_o R/fD$ where x corresponds to the off-axis distance shown in figure 12. Here $\sin\phi_o \sim x/R$ has been employed in the expression for η. The resolving half-width is then $\Delta W = 2x = 3.32\, c_o R/fD$. This result is shown in figure 41 in addition to the experimentally determined value for a source situated at a distance of R = 2.81 m from the reflector The good agreement between theory and experiment confirms the accuracy of the Fraunhofer diffraction pattern description for the reflector spatial discrimination characteristics.

Gain - The directional microphone system also has a significant gain. A gain exists because the large collecting area of the reflector focuses the sound onto the small focal point microphone. In an ideal system without diffraction the gain, G, depends on the solid angle subtended by the reflector and the focal point microphone so that $G = (D/d)^2$ where D = 1.067 m and d = 0.635 cm. However, the frequency dependent diffraction characteristics smear out the focal point image so that only part of the acoustic energy incident on the reflector is concentrated on the focal point microphone.

The directional microphone gain in, this case, can be determined experimentally (ref. 5). The sound pressure level generated by a point source of sound is measured with the reflector and with an omnidirectional microphone. Source-to-reflector and source-to-omnidirectional microphone distances are identical during the measurements. The ratio of these two measurements represents the gain, G,

$$G(f,R) = \frac{\overline{p_{DM}^2}(f,R)}{\overline{p_o^2}(f,R)} \tag{A.1}$$

where $\overline{p_{DM}^2}$ defines the focal point microphone sound pressure level and $\overline{p_o^2}$ represents the omnidirectional microphone sound pressure level. The gain measurement, which was repeated in the present study as a check on the directional microphone system, is shown in figure 41 for two source distances corresponding to R = 2.81 m and 2.07 m. The large gain was beneficial at high frequencies because turbulent boundary layer noise decreases rapidly with increasing frequency.

The directional microphone gain must be determined before absolute source levels can be calculated. At low frequencies the gain function can be calculated explicitly (ref. 5) based on the Fraunhofer diffraction theory giving the result

$$G(f,R) = \frac{1}{4}\left[\frac{\pi D^2}{2Rc_o}\,\frac{2R-R_c}{R_c}\right]^2 f^2 \tag{A.2}$$

which is plotted in figure 41.

Differences between the measured and theoretical gains at high frequencies in figure 41 are attributed to spherical aberrations at the focal point microphone. These characteristics are not included in the analytical calculations of the gain. Thus, the experimentally determined gain was used at high frequencies for all data reduction.

APPENDIX B

Forward Flight Effects

Shear Layer Refraction - As shown in figure 13, refraction changes both the acoustic ray path as well as the path length of the sound waves arriving at a microphone station outside the flow. In addition, transmission of sound across the open jet shear layer changes the divergence rate of the acoustic ray tubes. These latter changes in path length and divergence rate require correcting the measured sound pressure levels.

The detailed analytical study and experimental verification by Schlinker and Amiet (ref. 47) formed the basis of the corrections applied to the present data. The corrections were used to convert measurements at the observer station (O), in figure 13, to the constant sideline station (D) on the non-refracted path. The corrected sound pressure level represents an equivalent measurement in the absence of the shear layer. In other words, the shear layer is considered to be located at infinity with uniform flow existing between the source and the far field microphone at station D. As concluded in the study of Schlinker and Amiet, the finite thickness shear layer can be replaced by an idealized vortex sheet. Specific details of the shear layer mean velocity profile are, therefore, not needed.

An example of the magnitude of the angle and amplitude changes is given in figure 42 for an open jet Mach number of M = 0.5, corresponding to one of the operating conditions tested in the present study. The distance to the sideline microphone measurement station is given by $h/y_1 = 0.14$ where h represents the source-to-shear layer distance and y_1 is the sideline distance in figure 13. As shown by figure 42 , sound initially propagating at $\theta_c = 80°$ inside the open jet is refracted to $\theta_t = 113°$ outside the airstream. Also, the sound pressure level measured on the resulting refracted path at station 0 in figure 13 should be increased by 4 dB according to figure 42. Note that the amplitude correction is always added to the measured data.

Apparent Source Location - The above described refraction angle changes control the propagation of a single ray through the shear layer and arriving at the far field microphone station (O) in figure 13. In contrast, the directional microphone system senses refracted acoustic rays propagating within the angle, $d\theta_t$, as shown in figure 14(a). Transmitted rays, A and B, each of which are refracted differently, define the angle, $d\theta_t$, in the horizontal plane. Since the directional microphone system senses only the refracted rays outside the flow, it must be focused on the "apparent" source location defined by rays A and B. The intersection of these rays inside the flow controls this apparent source location S_H, in figure 14(a).

Position S_H was determined analytically using the refraction angle correction controlling rays A and B. (See Appendix C for a detailed evaluation.) For each Mach number, M, and directivity angle, θ_c, a unique apparent source position was calculated. As shown by the analytical derivation, the apparent source location is independent of the distance to the reflector surface.

Once the apparent source location was calculated, the sideline distance, y_1, for the directional microphone traverse could be selected. This distance was controlled by the apparent source-to-reflector distance, R, in figure 12. Since detailed calibrations of the directional microphone spatial resolution and gain were only available for two specific values of R, the value of y_1 was selected to provide a distance of R = 2.07 m or 2.81 m between the reflector and the apparent source position. Recall that the value of R controlled the focal point microphone location r_i, in figure 12.

As shown by figure 14(a), the directional microphone senses sound within a solid angle. In the horizontal plane, rays A and B (fig. 14(a)) describe the limits of this solid angle in addition to determining the apparent source position. In the vertical plane (fig. 14(b)) rays C and D define similar limits of the solid angle. According to the arguments previously presented, the directional microphone system must be focused on the apparent source position defined by the intersection of rays C and D inside the flow. These rays experience identical refraction angle changes in the vertical plane in contrast to the horizontal plane where rays A and B are refracted differently as they propagate through the shear layer. Thus, tracing rays C and D back into the flowfield resulted in a different apparent source position in the vertical plane when compared to the horizontal plane. Details of the analysis used to predict the apparent source position, S_V (see fig. 14(b)) in the vertical plane are included in Appendix C.

Both S_H and S_V are situated on the reflector centerline but at different distances from the open jet shear layer. Figure 14(a) shows that S_H is situated at a distance, a, from the shear layer while figure 14(b) indicates that S_V is located at a distance of b_1. The significance of these different apparent source locations is best demonstrated by a numerical example. For M = 0.5 and $\theta_c = 50°$, the direct distance between S_H and S_V is 16 cm.

The ability to sense the acoustic radiation from these different source regions depends on the directional microphone depth of field. This parameter, shown in figure 43 represents the frequency dependent decrease in the measured directional microphone output as a source is moved closer or further from the reflector. In each case the focal point microphone distance, r_i, is fixed by the distance R shown in figure 12. Consequently, source position variations about R, represented by $R \pm \Delta$, result in a decrease in the measured response.

The different source locations given by S_H and S_V represent the extremes of the apparent source position in the open jet. Ideally, the directional microphone should have a large depth of field to sense the distributed apparent source region. Oddly, this contradicts the usual requirement for sharp spatial resolution demanded of directional microphone systems.

The final criteria selected for focusing the directional microphone system on the apparent trailing edge noise source region was based on the distance to the midpoint between S_V and S_H. As shown in figure 44, the sideline distance, y_1, was selected to provide $R_{MID} = R$. Here R = 2.81 m or 2.07 m corresponding to the two distances for which detailed depth of field calibrations were available. Most important of all, with the system focused on R_{MID}, the decrease in the system output due to the source at $R_{MID} \pm \Delta R/2$, where ΔR represents the distance between S_H and S_V, could not exceed 0.5 dB. This tight tolerance assured that the apparent source region was definitely within the reflector depth of field. All data reported in the present study satisfied this condition.

It should be noted that as the measurement angle, θ_c, approached the open jet axis, the distance between S_H and S_V increased to the point where the depth of field was insufficient for sensing the entire source region at high Mach numbers. This situation was considered unacceptable and measurements at such conditions were not conducted at high Mach numbers for angles close to the open jet axis. Other investigators should be aware of this limitation when using a directional microphone to investigate acoustic source distributions at high Mach numbers in an open jet test section.

Scattering Effect on Directional Microphone Measurements - The directional microphone spatial resolution and gain characteristics shown in figures 40 and 41 apply only in the absence of flow between the acoustic source and the directional microphone system. In reality, the directional microphone, situated outside the flow, collects the sound transmitted through the turbulent shear layer. Turbulent eddies in the shear layer can spatially scatter the sound sufficiently to reduce the measured acoustic source strength and broaden the source distribution pattern. For example, if the directional microphone were scanned past an ideal point source of sound inside the open jet the "apparent" gain of the system would be reduced while the diffraction pattern would be broadened. These changes must be accounted for since the data reduction procedure includes the directional microphone gain and spatial resolution characteristics. A summary of the effects of scattering on the measured sound pressure levels is provided here.

To help understand the scattering effect on the measured directional microphone sound pressure levels, the following tentative physical explanation is presented. The argument is based on a point source of sound situated in the open jet potential core. Initially, a wavefront originating from the

acoustic source has a smooth spherical shape as shown in figure 45. While passing through the shear layer local scattering by the turbulence structure reorients small segments of the acoustic wavefront. The angle between the normal to each wavefront segment and the reflector axis is no longer zero. Thus, the wavefront segment arriving at the reflector appears to originate from an off-axis source. Since the response to off-axis sources is diminished, the directional microphone output is decreased. In this manner, the effective gain of the system is reduced. At the same time, the diffraction pattern for the point source is broadened giving the appearance of a distributed acoustic source region instead of a point source inside the open jet. This is similar to the appearance of a light observed through frosted glass. The size of the light appears to be much larger.

The effects can be demonstrated quantitatively using the source distribution measurements shown in figure 46 . The experiment was conducted during the present study with the aid of a point source of sound located inside the open jet test section. In each case the directional microphone was scanned past the source providing 1/3 octave band source distribution curves like those shown for 10 kHz and 40 kHz. The abscissa in each figure represents the ratio of the directional microphone sound pressure level to the omnidirectional sound pressure level. The latter microphone was placed at the directional microphone station corresponding to the peak in the measured acoustic source distribution. Apparent source-to-reflector and apparent souce-to-omnidirectional microphone distances were identical. The ratio of the sound pressure level measurements at the source distribution peak represented the directional microphone gain defined earlier.

At M = 0, scanning the directional microphone past the acoustic source provided the expected point source diffraction pattern and system gain. This is verified by comparing the measured half-width, ΔW in figure 46, with the theoretical value in figure 41 at the corresponding frequency. Also, a comparison of the gain represented by the peak values in figure 46 shows agreement with the previously measured values described in figure 41.

As the open jet Mach number increased the peak amplitudes in figure 46 decreased while the source distribution became broader. These changes were more pronounced at the higher frequency of 40 kHz since the acoustic wavelength was then comparable to the turbulent eddy size. Turbulence scattering of sound has been shown to be stronger under this condition (ref. 47).

The above described changes, represented by the parameters AMP and ΔW, were monitored over the range of 1/3 octave band center frequencies from 1.25 kHz to 50 kHz. Measurements were conducted using the point source of sound at each Mach number and directivity angle investigated in the airfoil trailing edge noise study. As an example, the final effective gain, G_e, applied to the reflector measurements obtained at M = 0.5 and $\theta_c = 90°$ is

given by figure 47. Here the value of G_e at f = 10 kHz, M = 0.5, and R = 2.07 m, is obtained from the corresponding peak value in figure 46. Also shown is the diffraction pattern half-width function, ΔW, which increases as frequency increases. These measured values obtained in the presence of flow, can be compared with the M = 0 measurements in figure 41. The difference in the directional microphone response demonstrates why scattering effects must be accounted for. Knowing the effective gain, G_e, trailing edge noise sound pressure levels can be calculated from the directional microphone measurements.

APPENDIX C

Apparent Source Position Beneath Shear Layer

Because of the angle change of a sound ray as it passes through the shear layer, the apparent position of a sound source, from an acoustical standpoint, is not the same as its true source position. The apparent source position can be readily calculated.

Consider rays in the plane defined by the vector normal to the two-dimensional shear layer and the flow vector and define this to be the xy plane (see fig. 48(a)). The actual source position is S and the apparent source position is S_H. The following geometrical relationships follow immediately:

$$s = h/\sin \theta_c \tag{C.1}$$

$$d\ell = s d\theta_c/\sin \theta_c \tag{C.2}$$

Thus,

$$d\ell = h d\theta_c/\sin^2 \theta_c \tag{C.3}$$

Likewise, in terms of θ_t rather than θ_c

$$d\ell = a d\theta_t/\sin^2 \theta_t \tag{C.4}$$

Combining equations (C.3) and (C.4)

$$a = h \frac{\sin^2 \theta_t}{\sin^2 \theta_c} \frac{d\theta_c}{d\theta_t} \tag{C.5}$$

Equation (1) of Amiet (ref. 34) is

$$\tan \theta_c = \zeta_1/(\beta^2 \cos \theta_t + M) \tag{C.6}$$

Taking the derivative gives

$$\frac{d\theta_c}{d\theta_t} = \frac{\sin \theta_t}{\zeta_1^3} \sin^2 \theta_c \tag{C.7}$$

which combined with equation (C.5) gives finally

$$a = h\left(\frac{\sin\theta_t}{\zeta_1}\right)^3 \tag{C.8}$$

For $\theta_t = 90°$, the actual and apparent source positions will coincide, but at other angles they will differ.

An apparent source position can also be calculated based on the ray paths in other planes. In particular, consider a plane perpendicular to the above plane and containing a ray in the xy plane after refraction by the shear layer. Thus, the plane makes an angle θ_t with the shear layer. This plane is shown in figure 48(b) which is basically the same as figure 11 of reference 53. The actual source position is not shown, but is again taken to be a distance h inside the shear layer.

If dz_1 is the ray tube width just at the shear layer and dz_2 is the width at a distance of y_1 from the source, then equation (A.19) of reference 53 gives

$$\frac{dz_2}{dz_1} = 1 + \left(\frac{y_1}{h} - 1\right)\zeta_1 \csc\theta_t \tag{C.9}$$

From the geometry of figures 14(b) and 48(b)

$$\frac{t_1}{dz_1} = \frac{t_1 + (y_1 - h)\csc\theta_t}{dz_2} \tag{C.10}$$

Substitution for dz_2/dz_1 from equation (C.9) gives

$$t_1 = h/\zeta_1 \tag{C.11}$$

However, t_1 is not the distance measured normal to the shear layer (fig. (14b)) since the plane considered makes an angle θ_t with the shear layer. The distance b_1 normal to the shear layer is

$$b_1 = t_1 \sin\theta_t = h\frac{\sin\theta_t}{\zeta_1} \tag{C.12}$$

Again, for $\theta_t = 90°$, $b_1 = h$, but in general $b_1 \neq h$. Note that for $\theta_t \neq 90°$, from equations (C.8) and (C.12), $a \neq b_1$ so that the apparent source position depends on which plane is being considered.

APPENDIX D

Boundary Layer Thickness

Boundary Layer Thickness Calculated for the Study of Schlinker (ref. 5) - For the NACA 0012 symmetric airfoil (22.9 cm chord) measurements reported by Schlinker, the boundary layer thickness was estimated using the flat plate boundary layer theory. It should be noted that a boundary layer trip was needed only on the pressure surface of the airfoil to eliminate discrete vortex shedding tones when the airfoil was at angle of attack. The trip was located at the 30 percent chord station. In contrast, natural transition was permitted to occur on the suction side of the airfoil. Based on the experimental data transition on the suction surface occurs at $x/c = 0.05$ when the airfoil operates at $\alpha = 6°$ angle of attack. A knowledge of the transition location on each surface was then used in the flat plate prediction for δ. The cumulative length over which the boundary layer developed corresponded to the distance from the individual transition points to the airfoil trailing edge. Contributions from the upstream laminar boundary layer were assumed negligible. The final value of δ listed in Table III represents the average of the pressure and suction side boundary layers estimated for the study in reference 5. The credibility of such average value predictions was demonstrated by the close agreement between flat plate predictions and measurements obtained in the present study for an airfoil at small angles of attack (fig. 19). Included in Table III are the airfoil geometric parameters.

A check on the ability to predict δ using the flat plate boundary layer theory is obtained by comparison with the NACA 0012 measurements reported by von Doenhoff (ref. 51). Logarithmic plots of the boundary layer velocity profiles were obtained for $\alpha = 0°$ with natural transition occurring in the boundary layer. Considering the $Re = 2.67 \times 10^6$ case shown in figure 19 of reference 50, skin friction measurements indicated that transition occurred at approximately 50 percent chord when $\alpha = 0°$. Calculating the equivalent flat plate turbulent boundary layer which starts developing at this station gives $\delta/c = 0.022$ at the airfoil trailing edge. In comparison, the measurements of von Doenhoff indicate that the velocity profile at 97 percent chord asymptotically approaches unity near $y/c = 0.02$. Thus, the calculated flat plate result is in good agreement with the experimental result. In addition, reference 50 shows that at the 52 percent chord station $\delta/c = 0.0025$ verifying that the laminar boundary layer upstream of the transition point represented only 10 percent of the final trailing edge boundary layer thickness.

Boundary Layer Thickness Calculated for the Study of Brooks and Hodgson (ref. 10) - The trailing edge turbulent boundary layer thickness for the NACA 0012 airfoil (60.96 cm) chord was calculated using the flat plate boundary layer theory. The approach was similar to that used in calculating δ/c for the study of Schlinker (ref. 5). Since a boundary layer trip was applied at

the 15 percent chord station in the study by Brooks and Hodgson, the calculation was initiated at this station.

Table IV gives the calculated value of δ/c in addition to the parameters describing the airfoil. The value of $\delta/c = 0.0166$ represents the average of the pressure side and suction side boundary layer thickness values.

It is worthwhile to compare the measured values of displacement thickness, δ^*/c, reported by Brooks and Hodgson with the value of δ/c calculated here. This comparison will be needed in a future discussion of the Strouhal value associated with the spectrum peak reported in reference 10. The present discussion will apply to the δ^*/c data reported for the $\alpha = 0°$ angle-of-attack geometry. Data for the $\alpha = 5°$ angle of attack was not provided by Brooks and Hodgson.

For the range of Mach numbers investigated at $\alpha = 0°$, δ^*/c was approximately constant and equal to 0.0065 in reference 10. Then $\delta/\delta^* \simeq 2$ based on the value of δ/c calculated above. This ratio is different from the typical value of $\delta/\delta^* = 8$ measured in a two-dimensional flat plate boundary layer theory. One possible explanation could be the basic difference between the flat plate geometry used to calculate δ/c and the airfoil geometry for which δ^*/c was measured. This, however, would imply that the flat plate boundary layer calculation for δ/c is in error by a factor of approximately four. Yet, measurements obtained by von Doenhoff (ref. 52) showed good agreement with the flat plate calculation for δ/c at $\alpha = 0°$ as noted in the previous subsection. Thus, it is possible that the value of δ^*/c is high in the study reported by Brooks and Hodgson.

A quantitative justification for the above statement is available from the recent study of D'Ambra and Damongeot (ref. 53) using a NACA 0012 airfoil. Their investigation of the airfoil fluctuating surface pressures and broadband noise presented frequency information in terms of a Strouhal number based on δ^*/c. Their displacement thickness was determined through sophisticated calculations based on the potential flow field method of Garabedian and Korn combined with a viscous boundary layer calculation. The following simple relationship was obtained to evaluate the effects of the various parameters:

$$\log_{10} \delta^* = -3.775 + 1.1 \frac{x}{c} + 0.12\, M + 0.8 \log_{10} c + 0.775\, \alpha \qquad (D.1)$$

Here, x/c represents the distance from the airfoil leading edge to the station at which δ^* is to be calculated. The airfoil chord length is specified in meters while α is given in degrees.

The above equation is specific to the NACA 0012 airfoil and includes the location of the transition point and several other parameters. The equation represents the best curve fit derived from the theoretical computations and is applicable for the compressible flow range of $0.3 \leq M \leq 0.84$ and $-4° \leq \alpha \leq 6°$.

Extending equation 62 to the incompressible flow test condition given by M = 0.2 in the study by Brooks and Hodgson gives $\delta^*/c = 0.00247$ for $\alpha = 0°$. In comparison the value reported in reference 10 is $\delta^*/c = 0.0065$. Differences between these values suggest that the displacement thickness in reference 10 may be large by a factor of approximately 2.5.

REFERENCES

1. George, A. R.: Helicopter Noise-State-of-the-Art. AIAA Paper 77-1337, 1977.

2. Schmitz, E. H., Boxwell, D. A.: In Flight Far Field Measurement of Helicopter Impulsive Noise. Journal of the American Helicopter Society, Vol. 24, No. 4, October 1976.

3. Munch, C. L., Paterson, R. W., Day, H.: Rotor Boradband Noise Resulting from Tip/Vortex Blade Interaction. Sikorsky Aircraft Report Ser. 50909, Contract DAHC04-72-C-0040, February 1975 (Available from DTIC as AD A020-692).

4. Paterson, R. W., Vogt, P. G., Fink, M. R., Munch, C. L.: Vortex Noise of Isolated Airfoils. J. of Aircraft, Vol. 10, No. 5, 1973, pp 296-302.

5. Schlinker, R. H.: Airfoil Trailing Edge Noise Measurements with a Directional Microphone. AIAA Paper 77-1269, 1977.

6. Fink, M. R.: Airframe Noise Prediction Method. Federal Aviation Administration Report No. FAA-RD-77-29, March 1977 (Available from DTIC as A039-664).

7. Fink, M. R.: Noise Component Method for Airframe Noise. AIAA Paper 77-1271, 1977.

8. Heller, H. H., Dobrzynski, W. M.: Unsteady Surface Pressure Characteristics on Aircraft Components and Far Field Radiated Airframe Noise. J. of Aircraft, Vol. 15, No. 12, December 1978, pp 809-815.

9. Yu, J. C., Joshi, M. C.: On Sound Radiation from the Trailing Edge of an Isolated Airfoil in a Uniform Flow. AIAA Paper No. 79-0603, 1979.

10. Brooks, T. F., Hodgson, T. H.: Prediction and Comparison of Trailing Edge Noise Using Measured Surface Pressures. AIAA Paper 80-0977, 1980.

11. Howe, M. S.: A Review of the Theory of Trailing Edge Noise. J. of Sound and Vibration, Vol. 61, No. 3, 1978, pp 437-465.

12. Yu, J. C., Tam, C. K.: An Experimental Investigation of the Trailing Edge Noise Mechanism. AIAA Paper 77-1291, 1977.

13. Olsen, W., Boldman, D.: Trailing Edge Noise Data with Comparison to Theory. AIAA Paper 79-1524.

REFERENCES (Cont'd)

14. Fink, M. R.: Prediction of Externally Blown Flap Noise and Turbomachinery Strut Noise. NASA CR-134883, August 1975.

15. Lighthill, M. J.: On Sound Generated Aerodynamically - Part I: General Theory. Proceedings of the Royal Society, London, Vol. A211, 1952, pp 564-587.

16. Ffowcs Williams, J., Hall, L. H.: Aerodynamic Sound Generation by Turbulent Flow in the Vicinity of a Scattering Half Plane. J. Fluid Mech., Vol. 40, Part 4, March 1970, pp 657-670.

17. Crighton, D. G., Leppington, F. G.: Scattering of Aerodynamic Noise by a Semi-Infinite Compliant Plate. Journal of Fluid Mechanics, Vol. 43, 1970, pp 721-736.

18. Crighton, D. G.: Radiation From Vortex Filament Motion Near a Half-plane Journal of Fluid Mechanics, Vol. 51, 1970, pp 357-362.

19. Howe, M. S.: Contributions to the Theory of Aerodynamic Sound with Application to Excess Jet Noise and the Theory of the Flute. Journal of Fluid Mechanics, Vol. 71, 1975, pp 625-673.

20. Howe, M. S.: The Influence of Vortex Shedding on the Generation of Sound by Convected Turbulence. Journal of Fluid Mechanics, Vol. 76, 1976, pp 711-740.

21. Howe, M. S.: The Effect of Forward Flight on the Diffraction Radiation of a High Speed Jet. Journal of Sound and Vibration, Vol. 50, 1977, pp 183-193.

22. Chase, D. M.: Sound Radiated by Turbulent Flow Off a Rigid Half-plane as Obtained from a Wavevector Spectrum Hydrodynamic Pressure. Journal of Acoustical Society of America, Vol. 52, 1972, pp 1011-1023.

23. Chase, D. M.: Noise Radiated From an Edge in Turbulent Flow. American Institute of Aeronautics and Astronautics Journal, Vol. 13, 1975, pp 1041-1047.

24. Chandiramani, K. L.: Diffraction of Evanescent Waves with Applications to Aerodynamically Scattered Sound and Radiation from Unbaffled Plates. Journal of the Acoustical Society of American, Vol. 55, 1974, pp 19-29.

REFERENCES (Cont'd)

25. Amiet, R. K.: Noise Due to Turbulent Flow Past a Trailing Edge. Journal of Sound and Vibration, Vol. 47, 1976, pp 387-393.

26. Amiet, R. K.: Effect of the Incident Surface Pressure Field on Noise Due to Turbulent Flow Past a Trailing Edge. Journal of Sound and Vibration, Vol. 57, 1978, pp 305-306.

27. Amiet, R. K.: High Frequency Thin-Airfoil Theory for Subsonic Flow. AIAA Journal, Vol. 14, 1976, pp 1076-1082.

28. Amiet, R. K.: Acoustic Radiation from an Airfoil in a Turbulent Stream. J. Sound Vibration, Vol. 41, 1975, pp 407-420.

29. Willmarth, W. W. and Roos, F. W.: Resolution and Structure of the Wall Pressure Field Beneath a Turbulent Boundary Layer. J. of Fluid Mechanics, Vol. 22, 1965, pp 81-94.

30. Hinze, J. O.: Turbulence. McGraw Hill Book Co., Inc., New York, 1975, second edition.

31. Eckert, E. R. and Drake, R. M., Jr.: Heat and Mass Transfer. McGraw Hill Book Co., Inc., New York, 1959, pp 144.

32. Corcos, G. M.: The Structure of the Turbulent Pressure Field in Boundary Layer Flows. J. of Fluid Mechanics, Vol. 18, 1964, pp 353-378.

33. Goldstein, M. E.: Scattering and Distortion of the Unsteady Motion on Transversely Sheared Mean Flows. J. of Fluid Mechanics, Vol. 91, 1979, pp 602-632.

34. Amiet, R. K.: Refraction of Sound by a Shear Layer. J. Sound and Vibration, Vol. 58, 1978, pp 467-482.

35. Amiet, R. K.: Noise Produced by Turbulent Flow into a Propeller or Helicopter Rotor. Paper 76-560, AIAA, 1976. (Also published in synoptic form in AIAA Journal, Vol. 15, No. 3, March 1977, pp 307-308.)

36. Amiet, R. K.: Noise Due to Rotor-Turbulence Interaction. NASA Conference Publication 2052, 1978, pp 109-126.

REFERENCES (Cont'd)

37. Paterson, R. W. and Amiet, R. K.: Noise of a Model Helicopter Rotor due to Ingestion of Turbulence, NASA CR-3213, 1979.

38. Bendat, J. S. and Piersol, A. G.: Measurement and Analysis of Random Data. John Wiley and Sons, Inc., 1965.

39. Amiet, R. K.: Frame of Reference Consideration for the Forward Flight Noise Problem. UTRC Report N212775-1, 1974.

40. Paterson, R. W., Vogt, P. G., Foley, W. M.: Design and Development of the United Aircraft Research Laboratories Acoustic Research Tunnel. J. of Aircraft, Vol. 10, No. 7, 1973, pp 427-433.

41. St. Hilaire, A. O., Carta, F. O., Fink, M. R., Jepson, W. D.: The Influence of Sweep on the Aerodynamic Loading of an Oscillating NACA 0012 Airfoil. Volume 1-Technical Report, NASA CR-3092, May 1979.

42. Hama, F. R.: An Efficient Tripping Device. J. of Aeronautical Sciences, Vol. 24, March 1957, pp 236-237.

43. Schlichting, H.: Boundary Layer Theory, McGraw Hill Book Co., 1968.

44. Paterson, R. W., Vogt, P. G., Fink, M. R., Munch, C. L.: Vortex Noise of Isolated Airfoils. J. Aircraft, Vol. 10, No. 5, May 1973, pp 296-302.

45. Laufer, J., Schlinker, R. H., Kaplan, R. E.: Experiments on Supersonic Jet Noise. AIAA J., Vol. 14, No. 4, April 1976, pp 489-497.

46. Schlinker, R. H.: Supersonic Jet Noise Experiments. PhD Dissertation, University of Southern California, 1975.

47. Schlinker, R. H., Amiet, R. K.: Shear Layer Refraction and Scattering of Sound. AIAA Paper 80-0973, 1980.

48. Klebanoff, P. S.: Characteristics of Turbulence in a Boundary Layer with Zero Pressure Gradient, NACA Rep. 1247, 1955 (Supercedes NACA TN-3178).

49. Schloemer, H. H.: Effects of Pressure Gradients on Turbulent Boundary Layer Wall Pressure Fluctuations. Journal of the Acoustical Society of America, Vol. 42, No. 1, 1967.

REFERENCES (Cont'd)

50. George, A. R., Najjar, F. E., Kim, Y. N.: Noise Due to Tip Vortex Formation on Lifting Rotors, AIAA Paper No. 80-1010, 1980.

51. Amiet, R. K.: Correction of Open-Jet Wind Tunnel Measurements for Shear Layer Refraction. Progress in Astronautics and Aeronautics, Vol. 46, 1976, pp 259-280. Also, AIAA Paper 75-532.

52. von Doenhoff, A. E.: Investigation of the Boundary Layer about a Symmetrical Airfoil in a Wind Tunnel of Low Turbulence, NACA Report No. 4-507, August 1940.

53. D'Ambra, F., Damongeot, A.: Airfoil Section Fluctuating Pressure and Rotor Broadband Noise. Paper No. 64 presented at the Fifth European Rotorcraft and Powered Lift Aircraft Forum, Amsterdam, The Netherlands, September 4-7, 1979.

Table I Mach Number vs Propagation Angle, and Airfoil Angle of Attack

SYMBOL	GEOMETRIC ANGLE, α
○	-0.4°
□	7.6
△	12

MACH NUMBER, M	PROPAGATION ANGLE, θ_c, deg				
	50	70	90	110	130
0.1	○	○□△	○	○	○
0.2		○□△			
0.3	○□	○□△	○□	○	
0.43	○	○□	○□		
0.5	○	○□	○□		
0.55		○			

Table II Angle and Amplitude Changes Associated with Refraction and Retarded Source Position Corrections

MACH NUMBER, M	PROPAGATION ANGLE, θ_c, deg				
	50	70	90	110	130
0.1	56.6 54.4 -1.21 -2.9	75.8 75.4 -0.68 -0.45	95.8 95.7 0.2 -0.69	116.6 115.3 0.95 -1.06	138.8 134.3 2.09 -2.94
0.2	—	81.1 80.8 -0.61 -0.33	—		—
0.3	66.7 63.3 -2.40 -2.49	86.4 86.4 -0.36 -0.16	109.2 107.4 1.95 -0.99	133.7 120.3 5.19 -5.79	—
0.43	71.9 69.3 -2.78 0.07	93.7 93.8 0.57 -0.15	121.4 115.4 4.71 -1.6	—	—
0.5	74.9 72.5 -2.53	98.6 98.0 1.43 -0.15	131.8 120 7.08 -4.80	—	—
0.55	—	102.5 101.1 2.26 -0.15	—	—	—

KEY TO PARAMETERS. NUMBERS REFER TO LISTING IN EACH BOX.

1) θ_t, degrees
2) θ_e, degrees
3) REFRACTION AMPLITUDE CORRECTION, dB
4) AMPLITUDE CORRECTION FOR CONVERSION TO RETARDED SOURCE POSITION

Table III Average Boundary Layer Thickness Calculated for the Data of Schlinker

VELOCITY m/sec	M	δ/c
30.5	0.09	0.0234
45.7	0.13	0.0218
61.0	0.18	0.0200
76.2	0.22	0.0197
91.5	0.26	0.0189
106.7	0.31	0.0184

AIRFOIL: NACA 0012
CHORD: c = 22.9 cm
SPAN: s = 53.3 cm
SOURCE TO MICROPHONE DISTANCE: $r_e = 2.81$

Table IV Average Boundary Layer Thickness Calculated for the Data of Brooks and Hodgson

VELOCITY m/sec	M	δ/c
38.6	0.1	0.0187
69.5	0.2	0.0166

AIRFOIL: NACA 0012
CHORD: c = 60.96 cm
SPAN: s = 46 cm
SOURCE TO MICROPHONE DISTANCE: $r_e = 1.22$ m

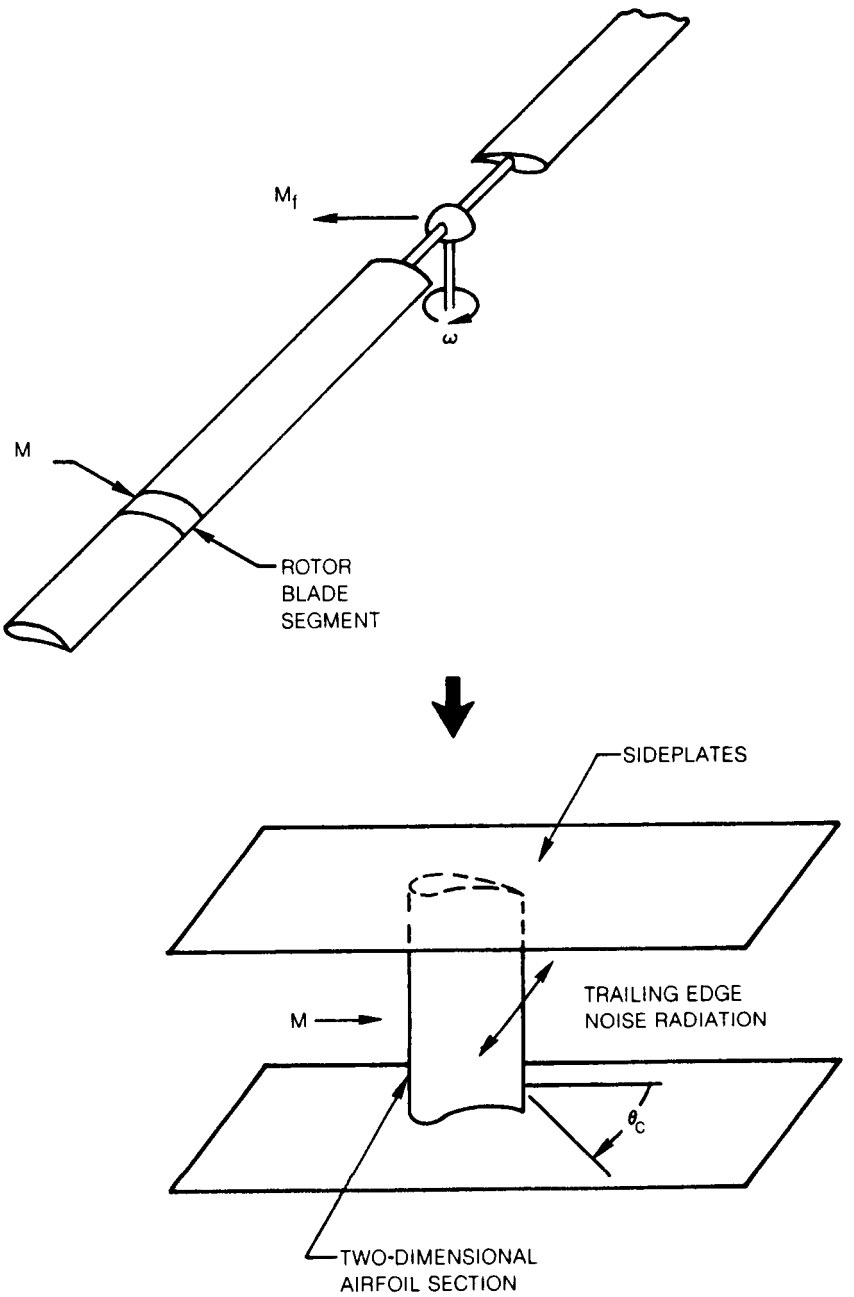

Figure 1 Simulation of Rotating Blade Trailing Edge Noise Radiation by a Two-Dimensional Airfoil Section

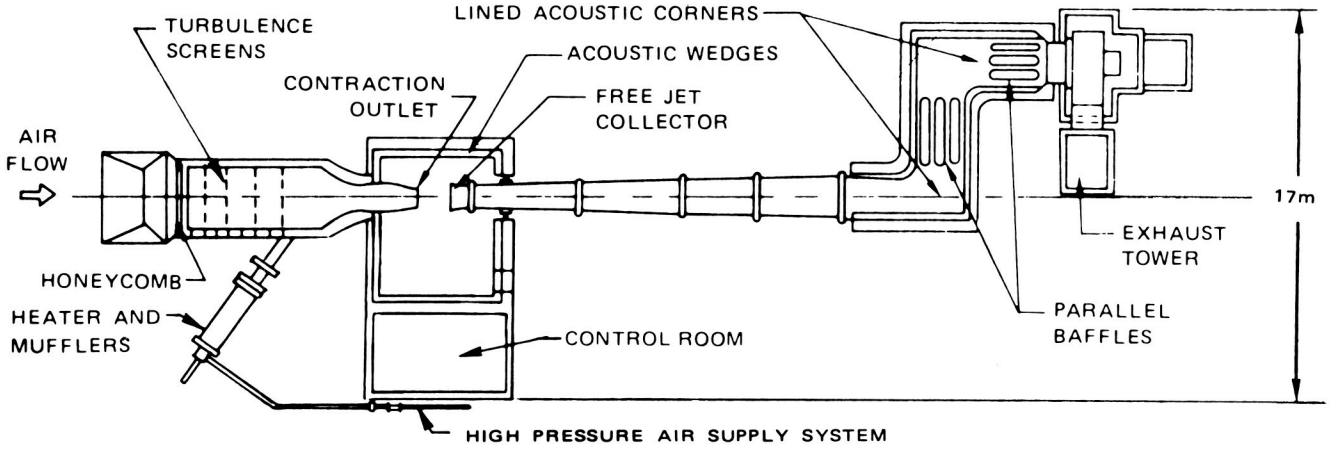

TOP VIEW

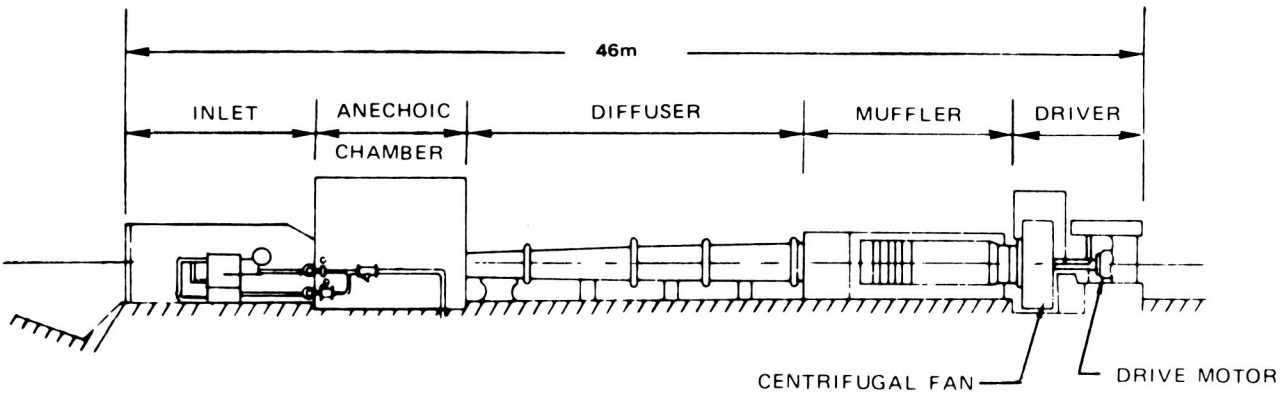

SIDE VIEW

Figure 2 UTRC Accoustic Research Tunnel

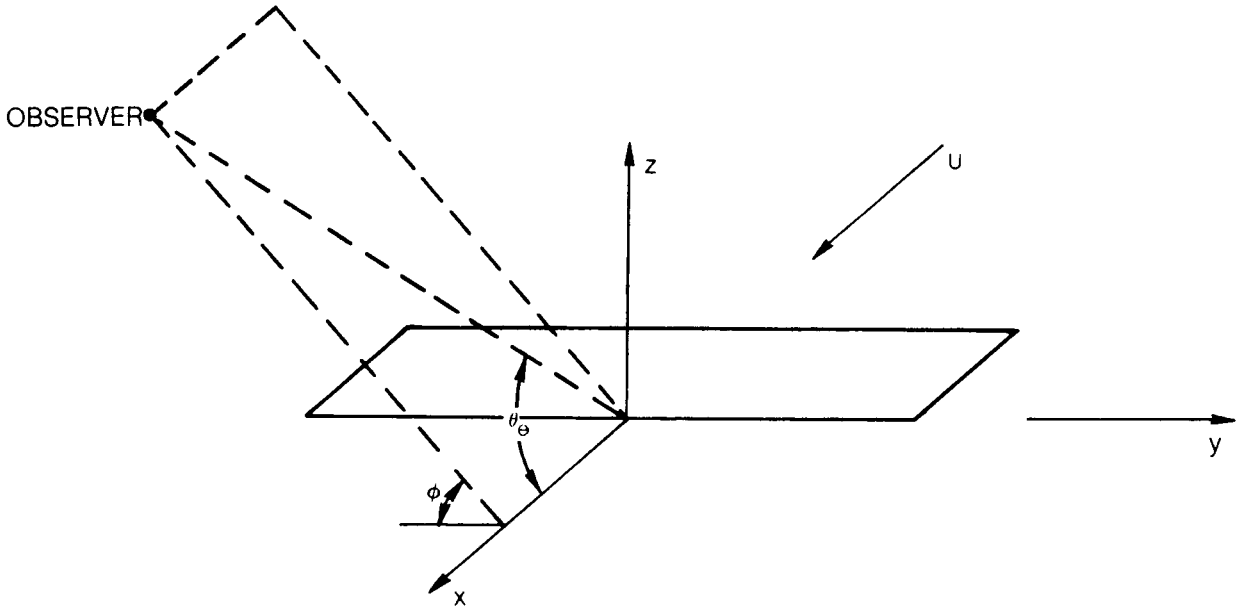

Figure 3 Airfoil in Rectilinear Motion

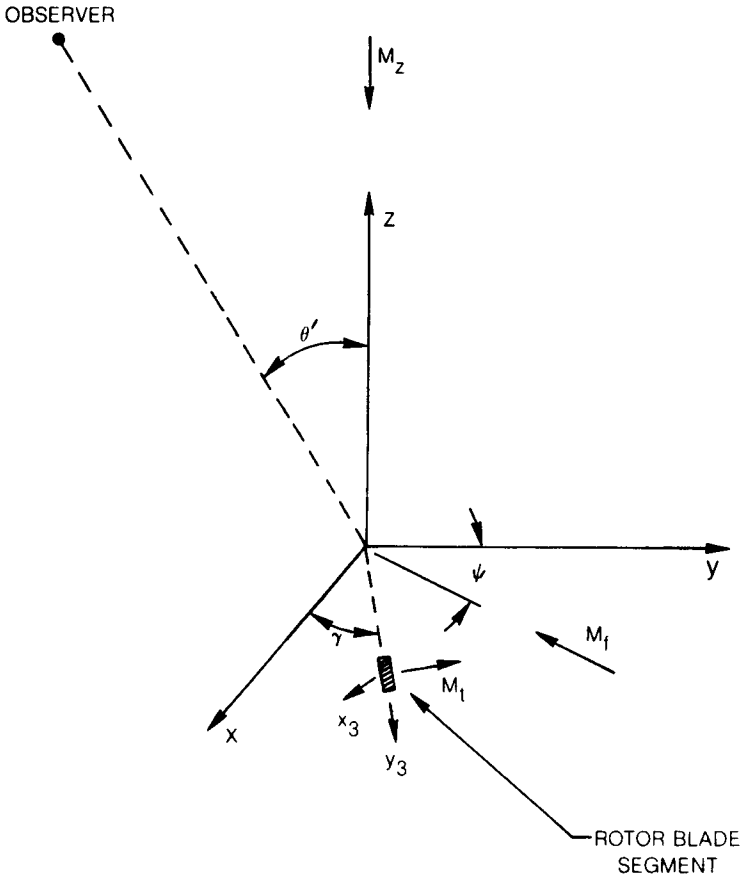

Figure 4 Rotor Blade Segment Moving in Forward Flight

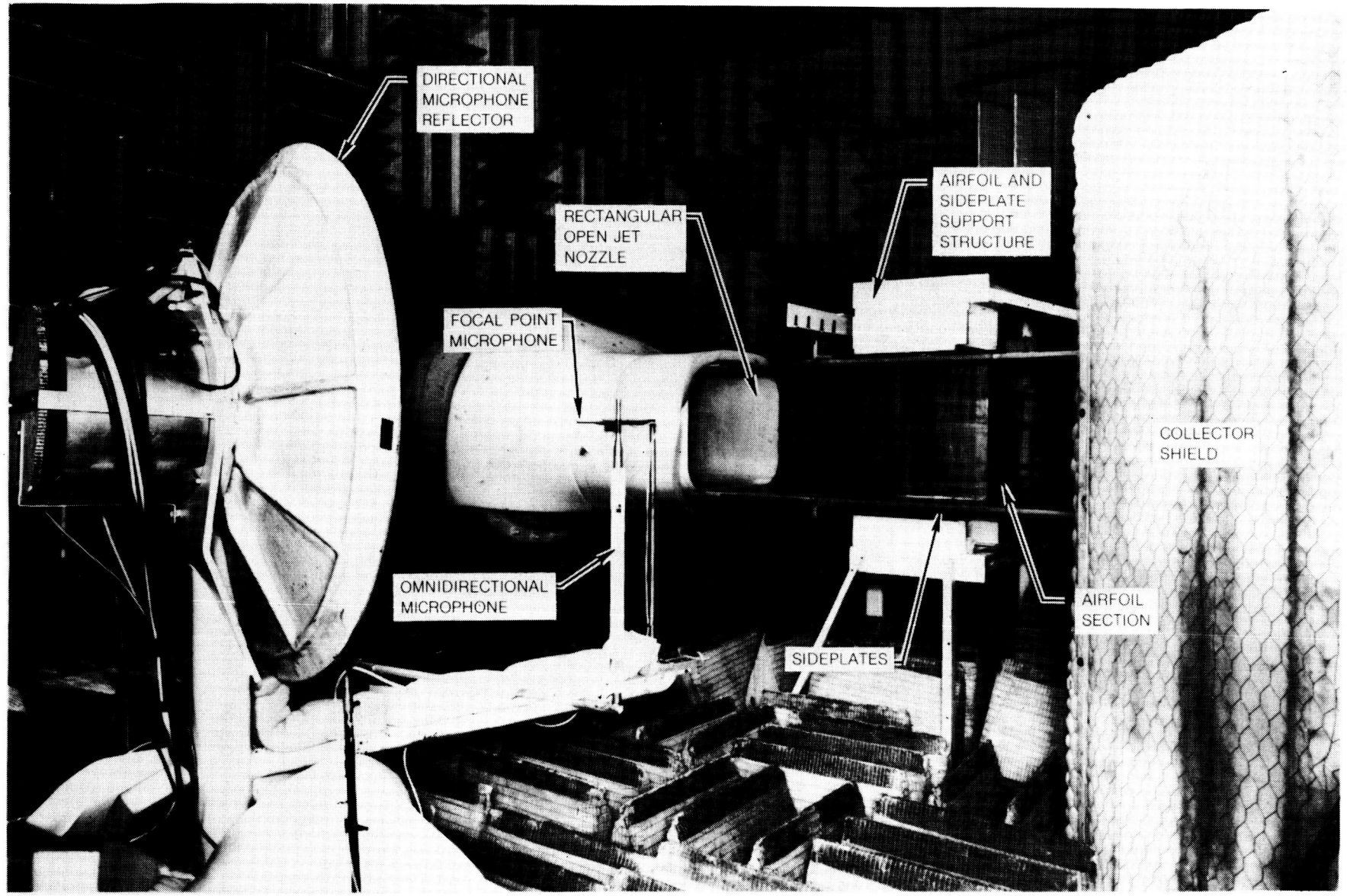

Figure 5 Open Jet Test Section Viewed from Far-Field Microphone Location

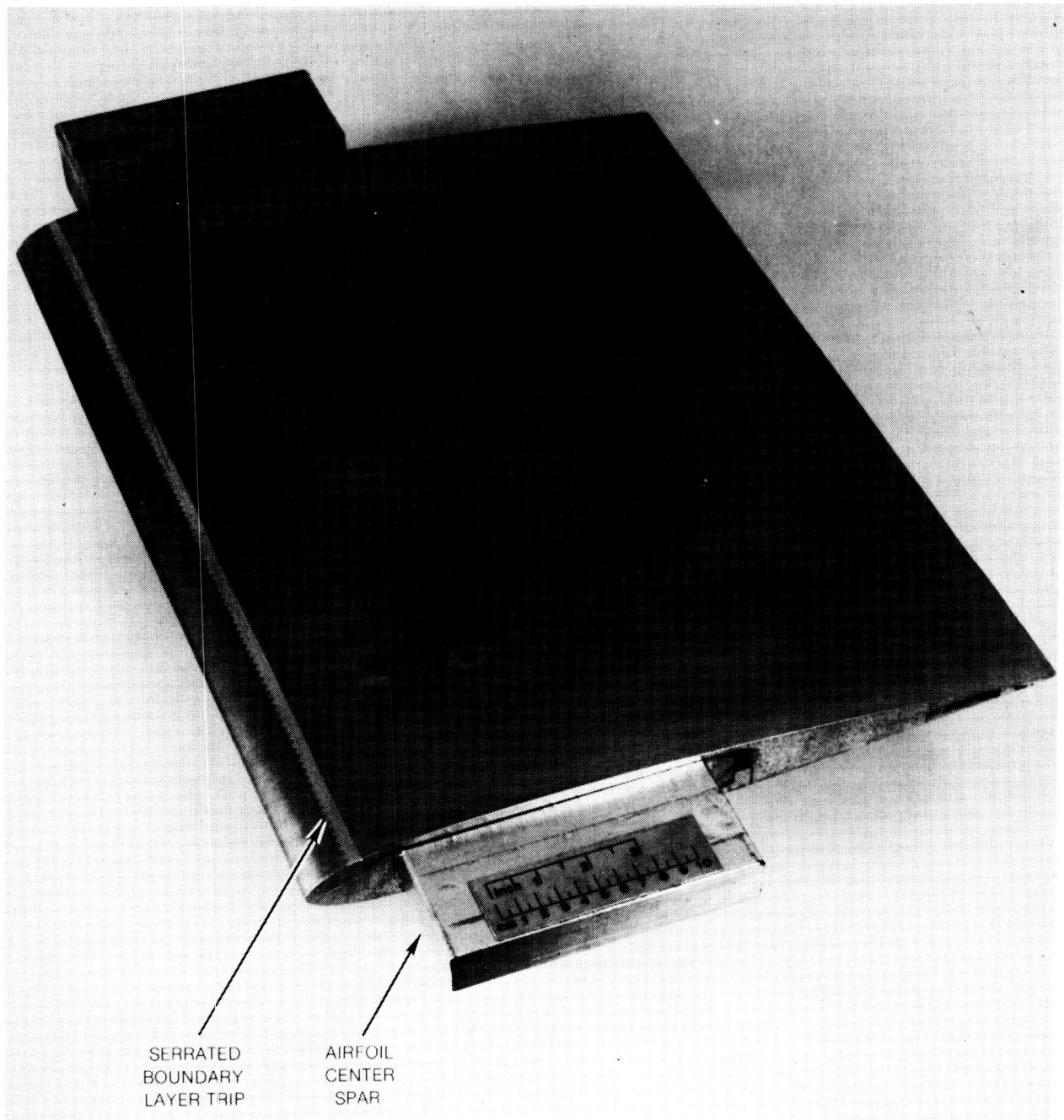

Figure 6 Section of Helicopter Main Rotor Blade Used for Isolated Airfoil Study

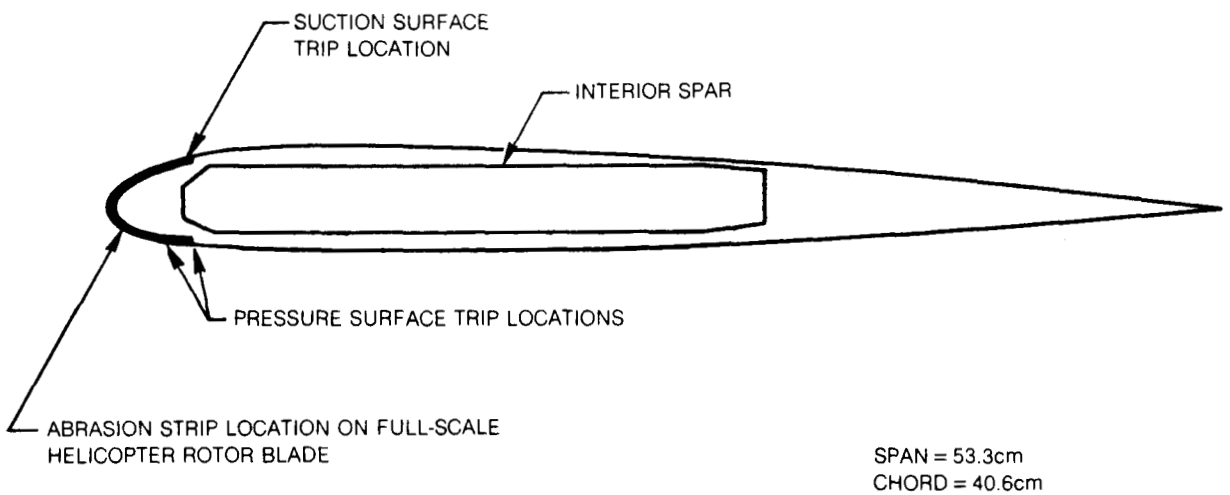

Figure 7 Rotor Blade Cross-Section

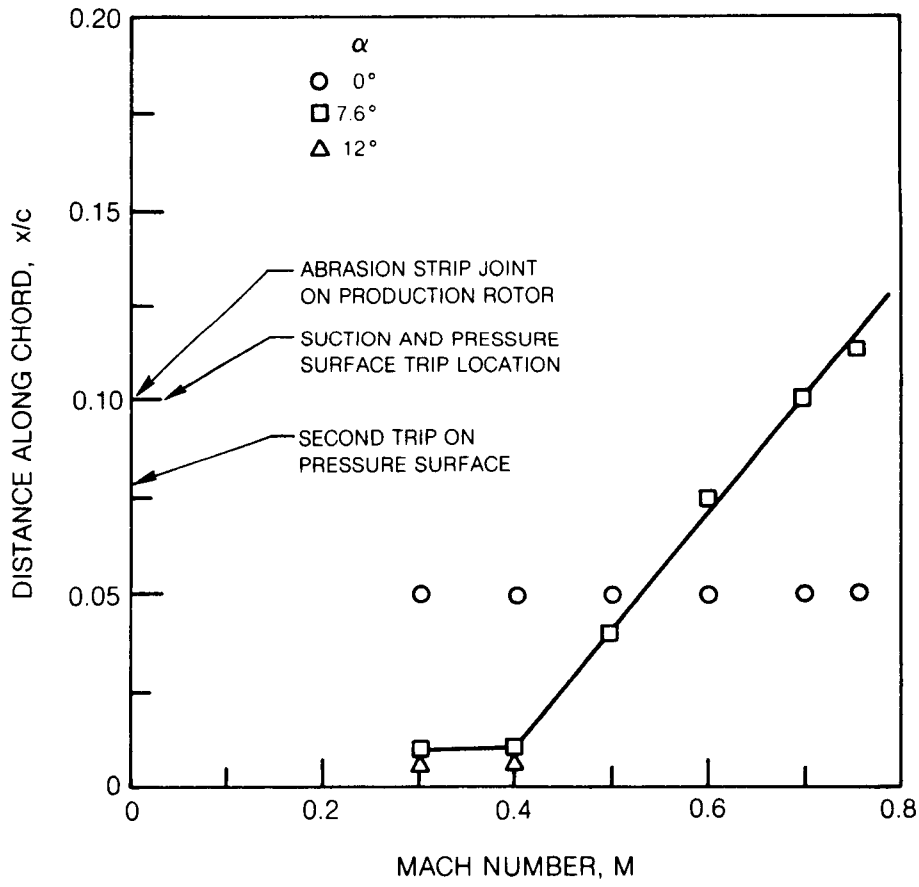

Figure 8 Location of Minimum Static Pressure Point on Airfoil Suction Side

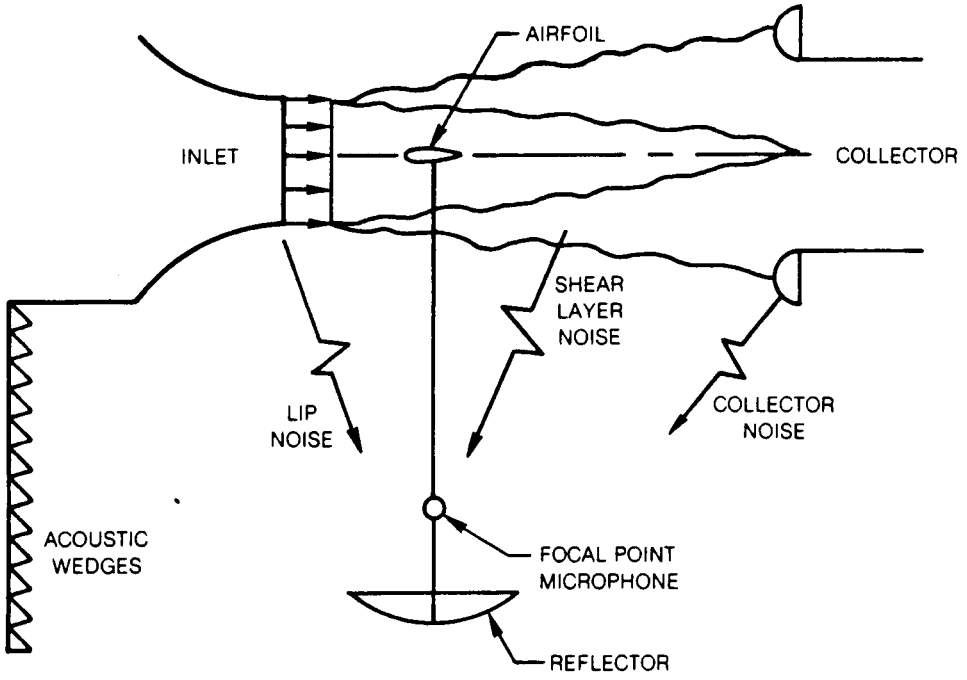

Figure 9 Facility Background Noise Sources

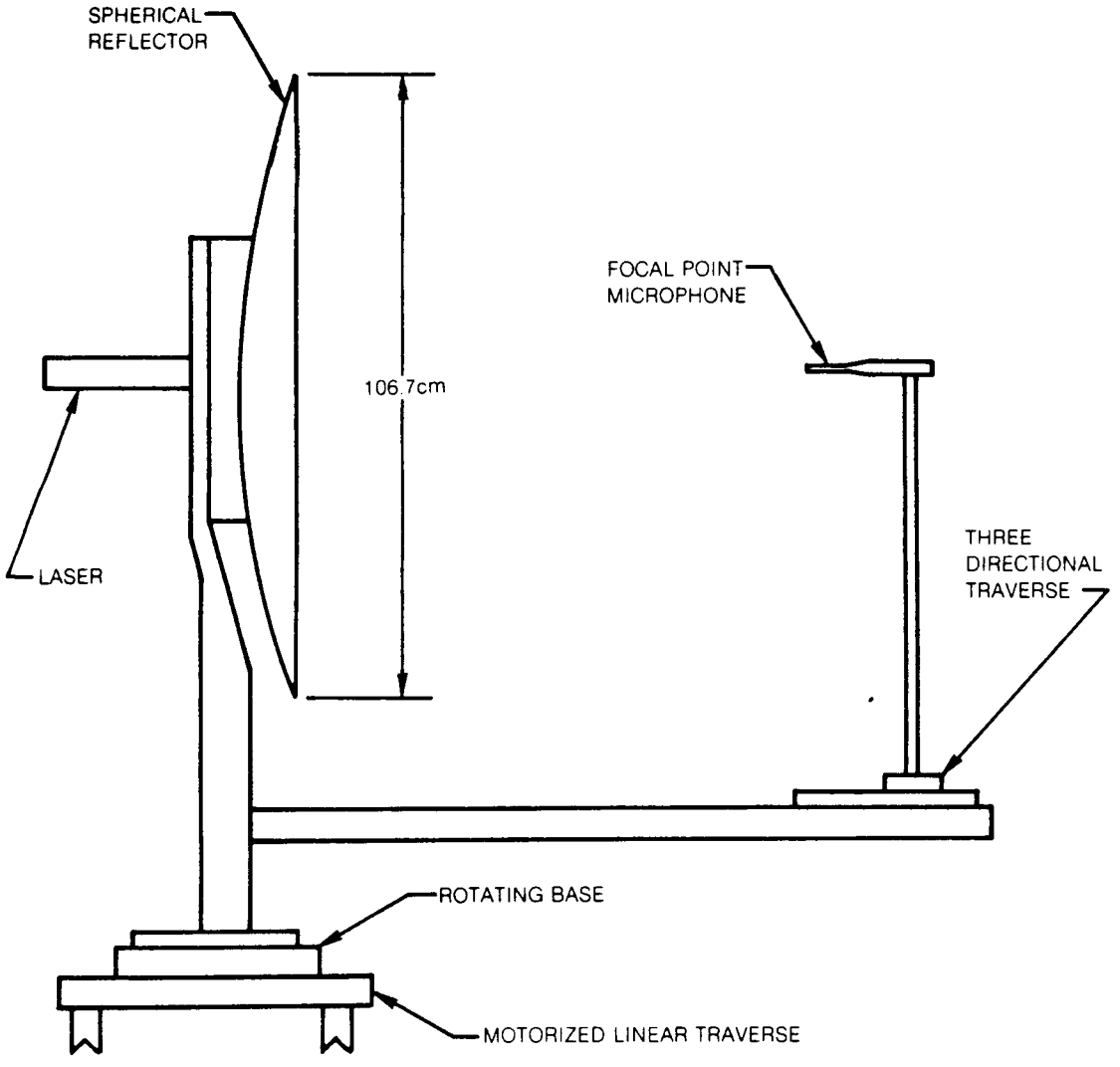

Figure 10 Schematic Diagram of Spherical Reflector Directional Microphone System

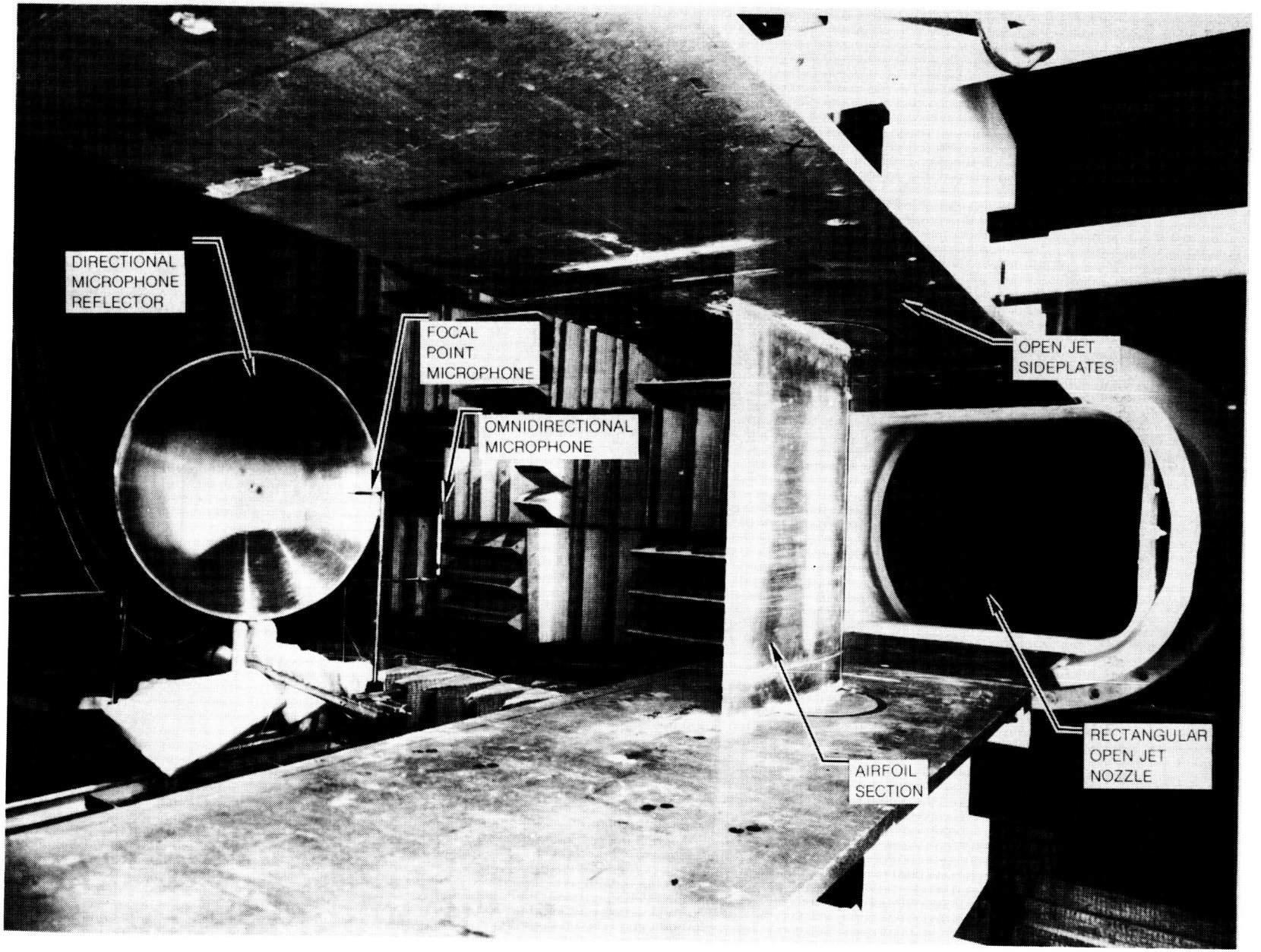

Figure 11 Test Section and Microphone Arrangement

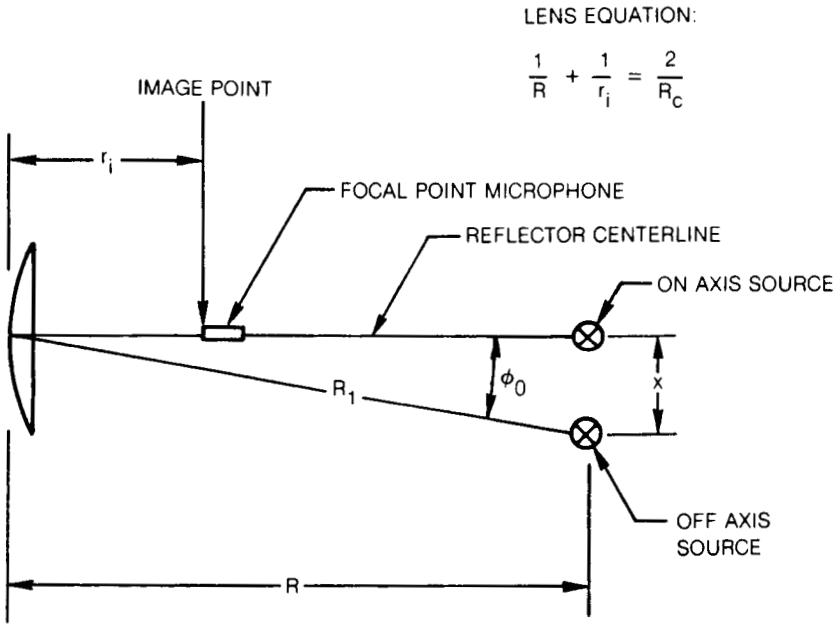

Figure 12 Directional Microphone Operating Principles

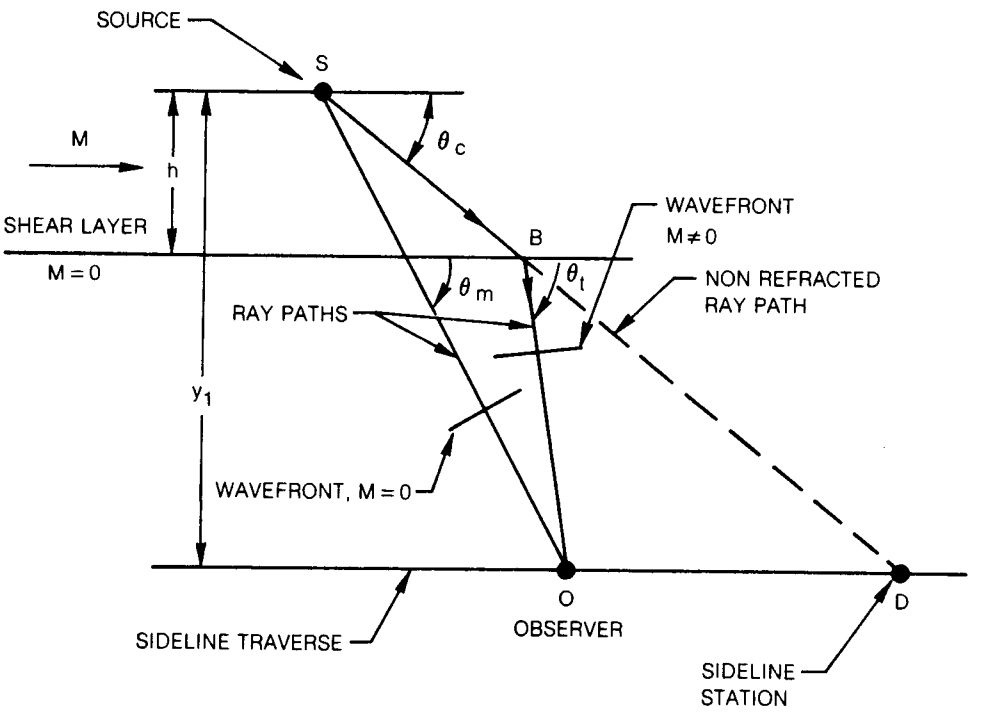

Figure 13 Geometry for Transmission of Sound Through a Shear Layer

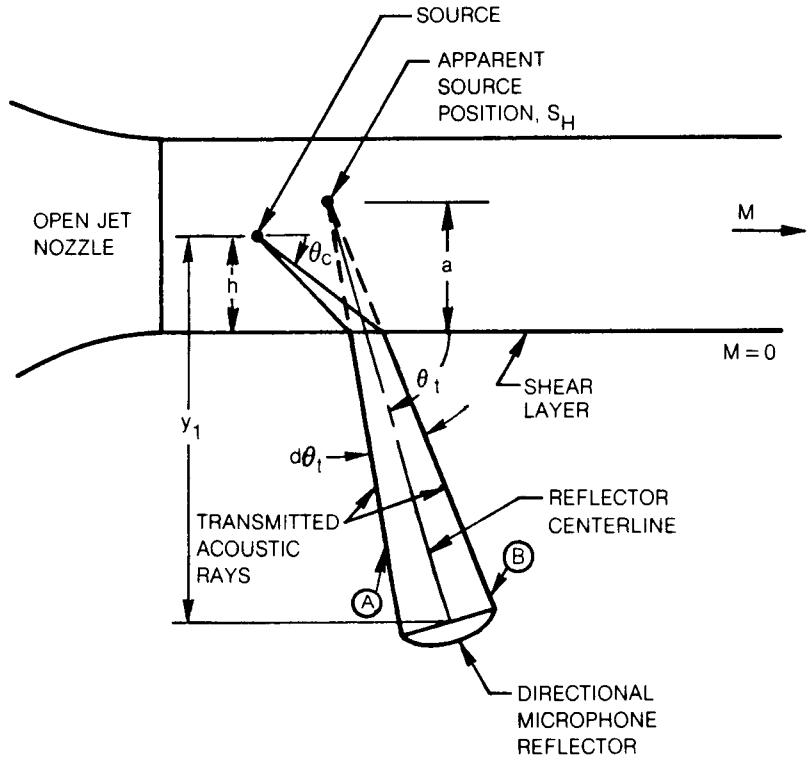

a) HORIZONTAL PLANE

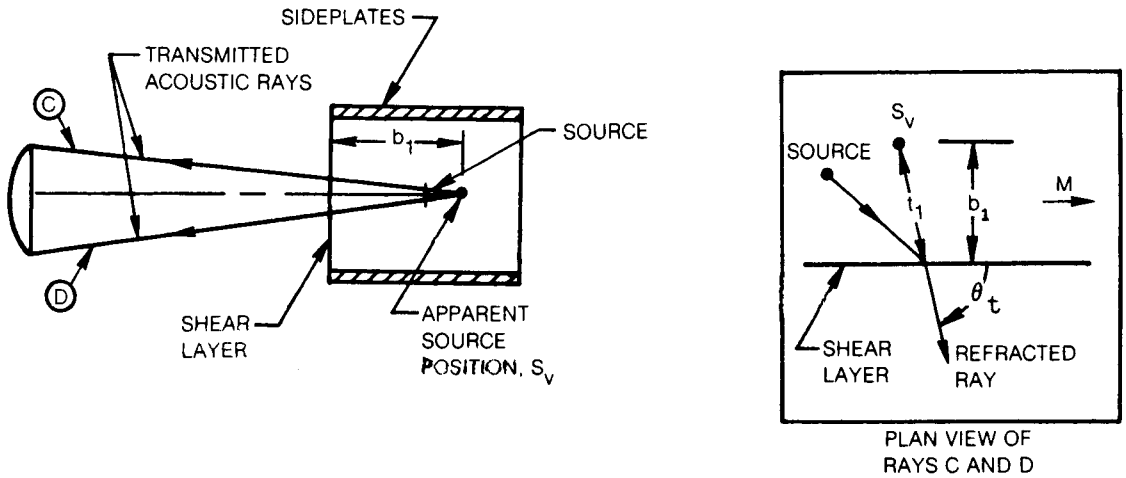

b) VERTICAL PLANE LOOKING UPSTREAM

Figure 14 Apparent Source Position Effects on Directional Microphone Alignment

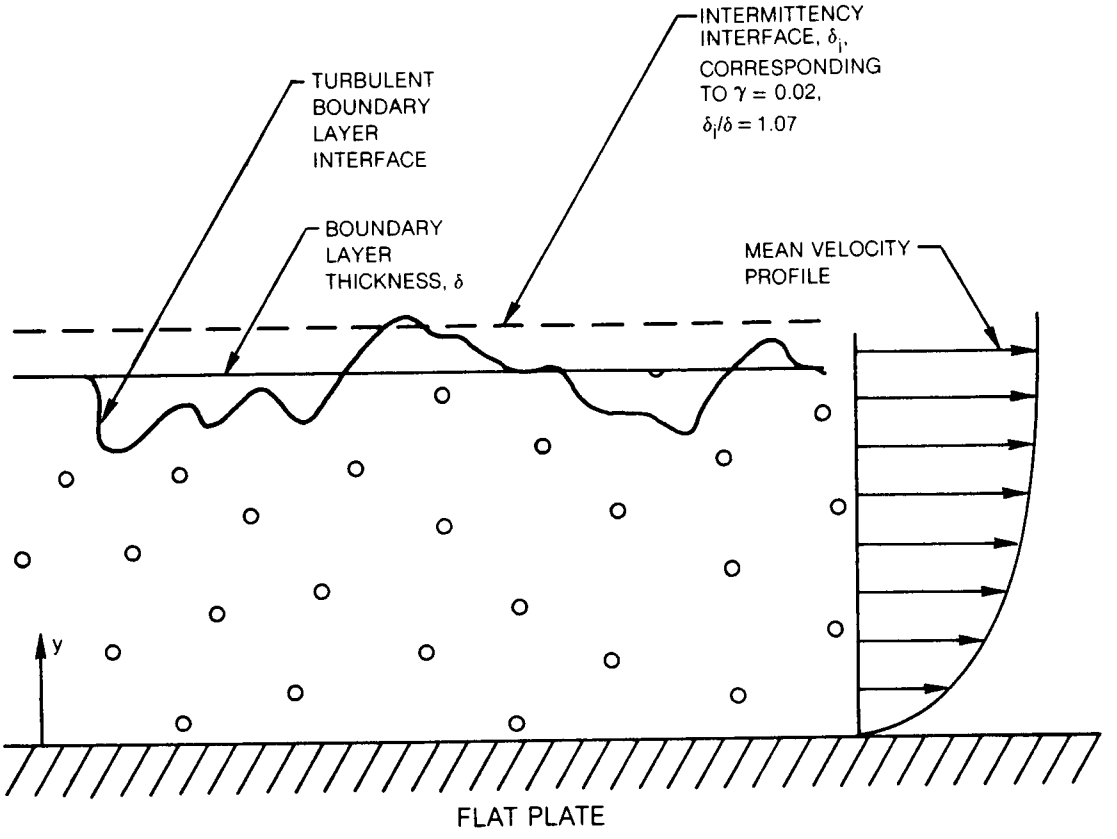

Figure 15 Boundary Layer Thickness and Intermittency Interface Measurements on a Flat Plate

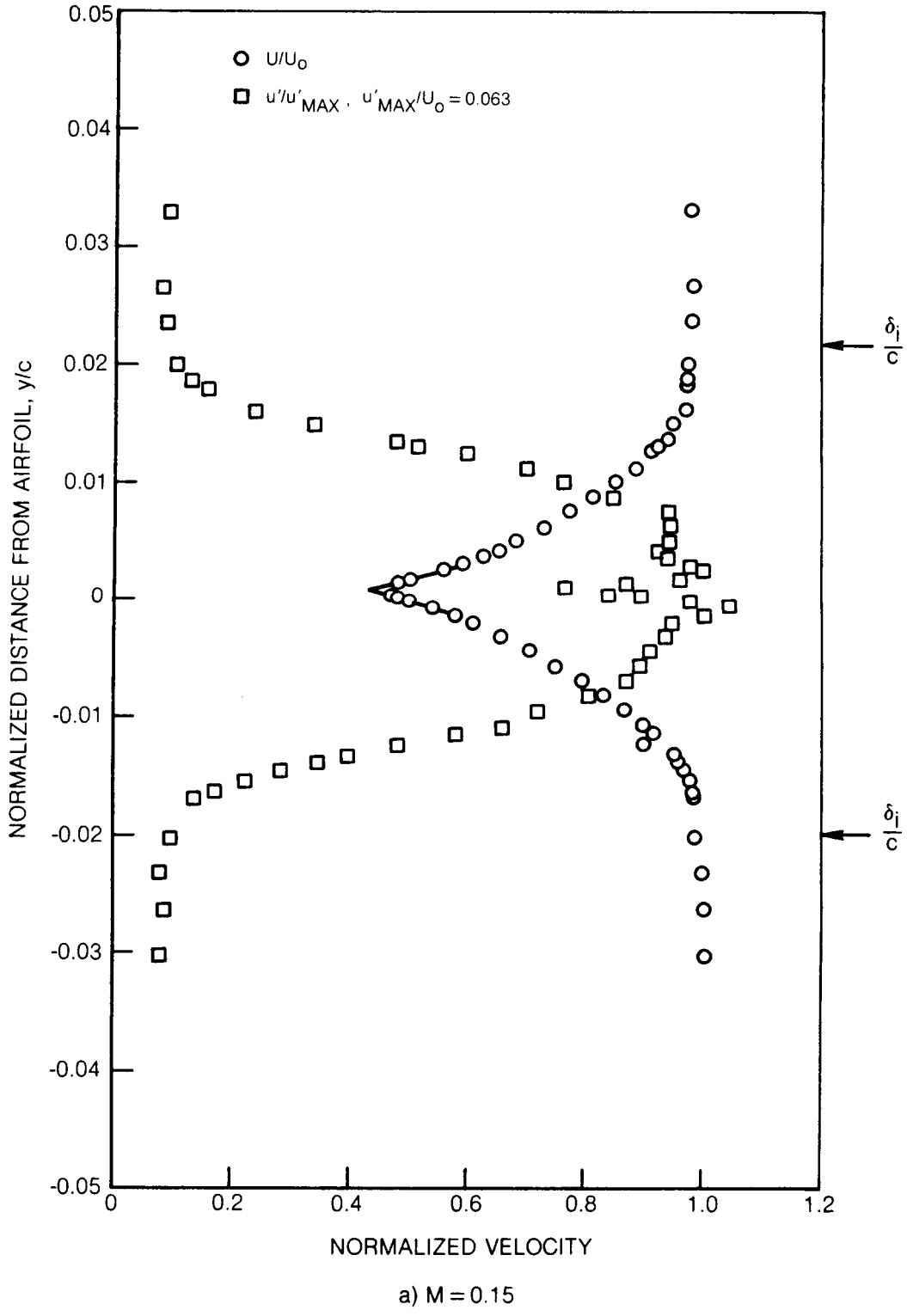

Figure 16 **Normalized Mean Velocity and Turbulence Intensity Profiles for Rotor Blade Section, $\alpha = -0.4°$**

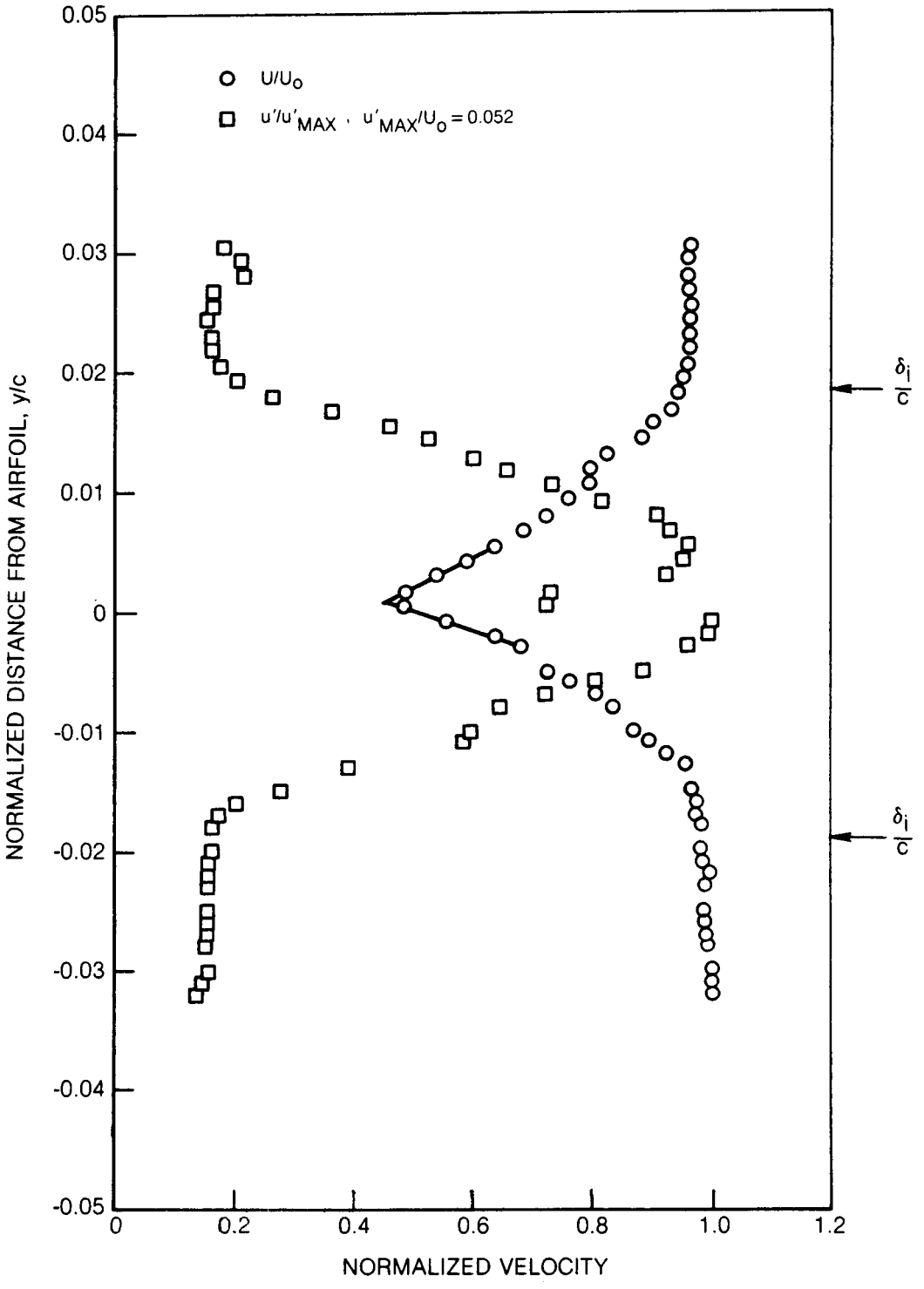

b) M = 0.3

Figure 16 — Continued

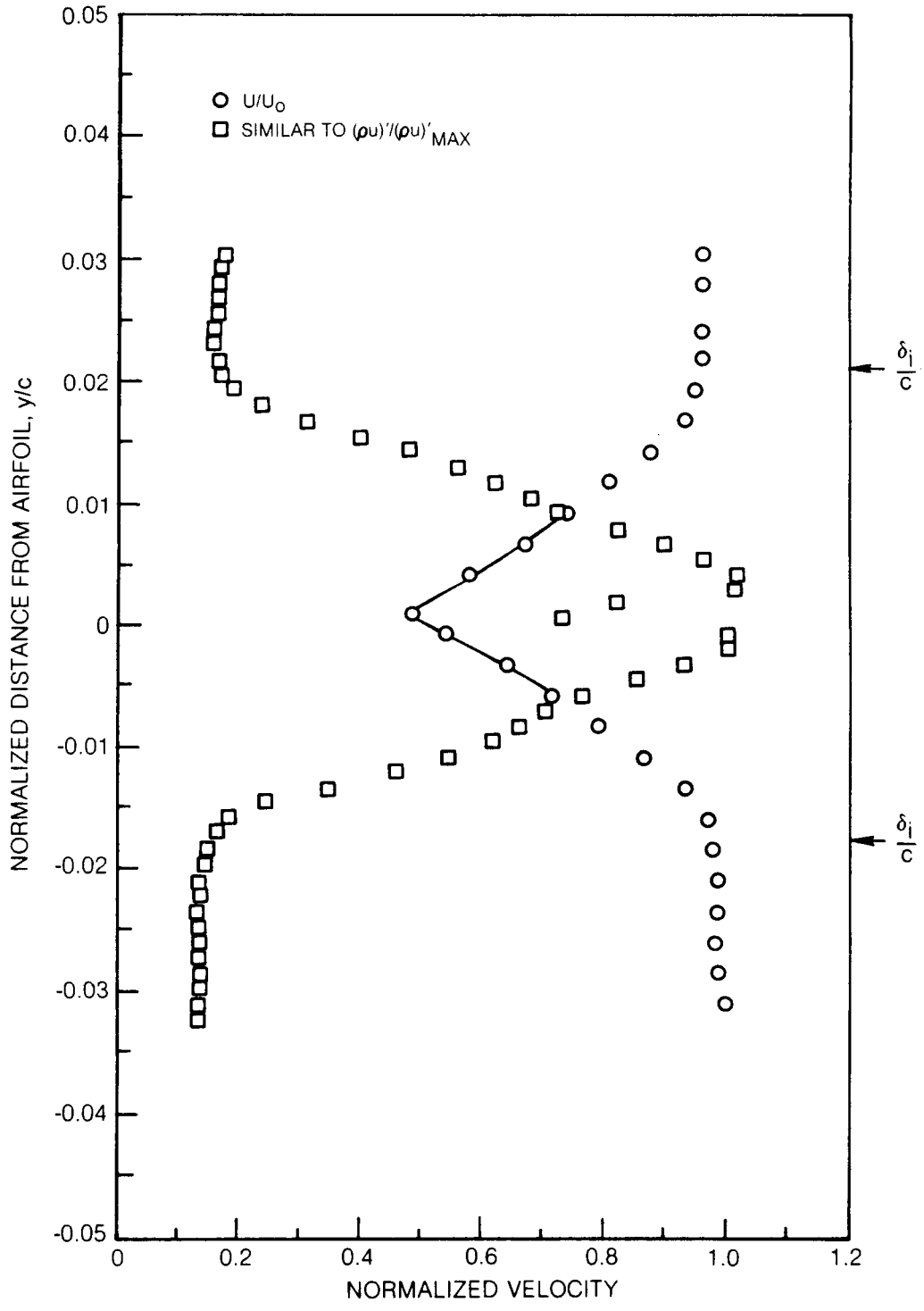

c) M = 0.43

Figure 16 — Continued

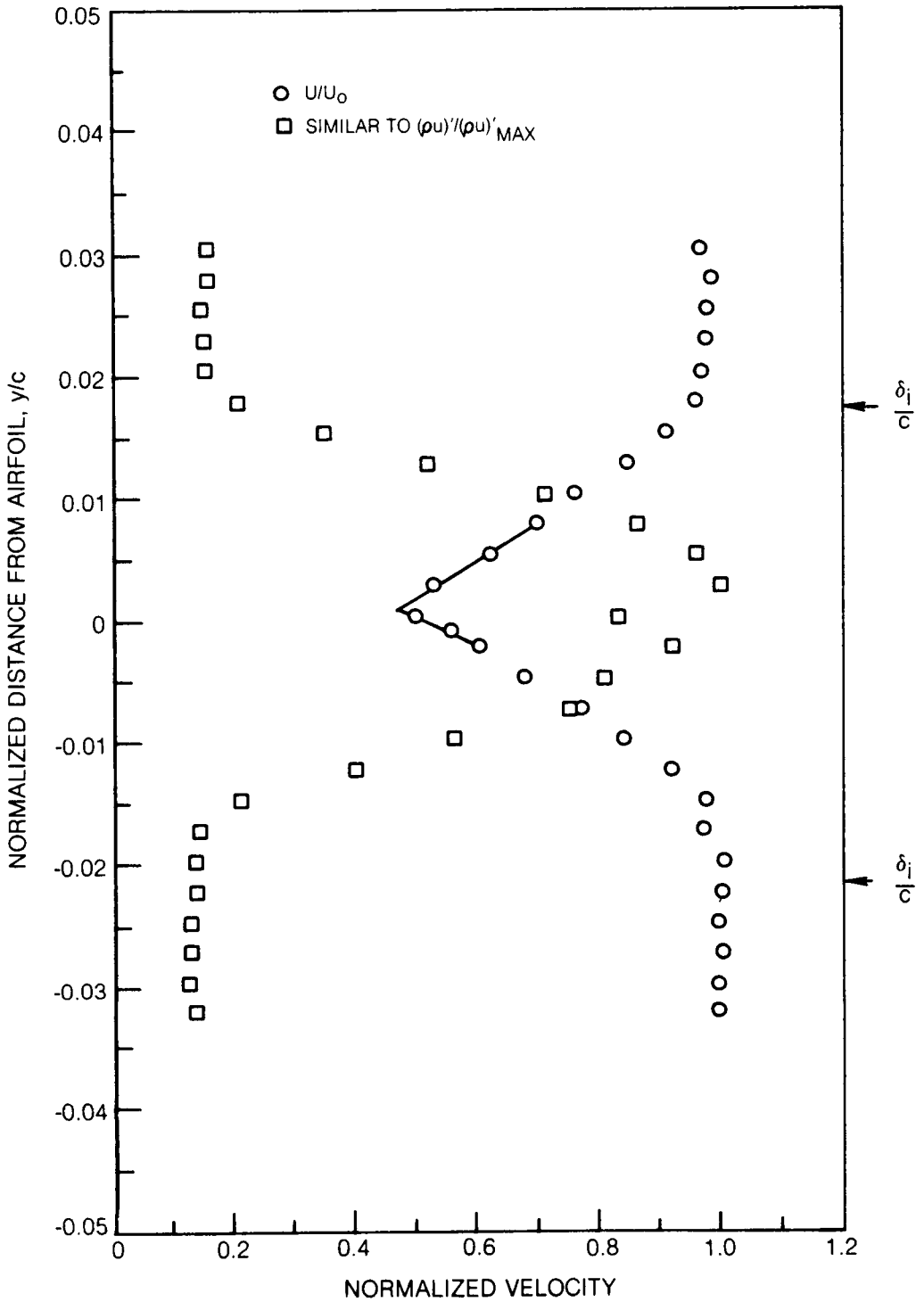

d) M = 0.5

Figure 16 — Concluded

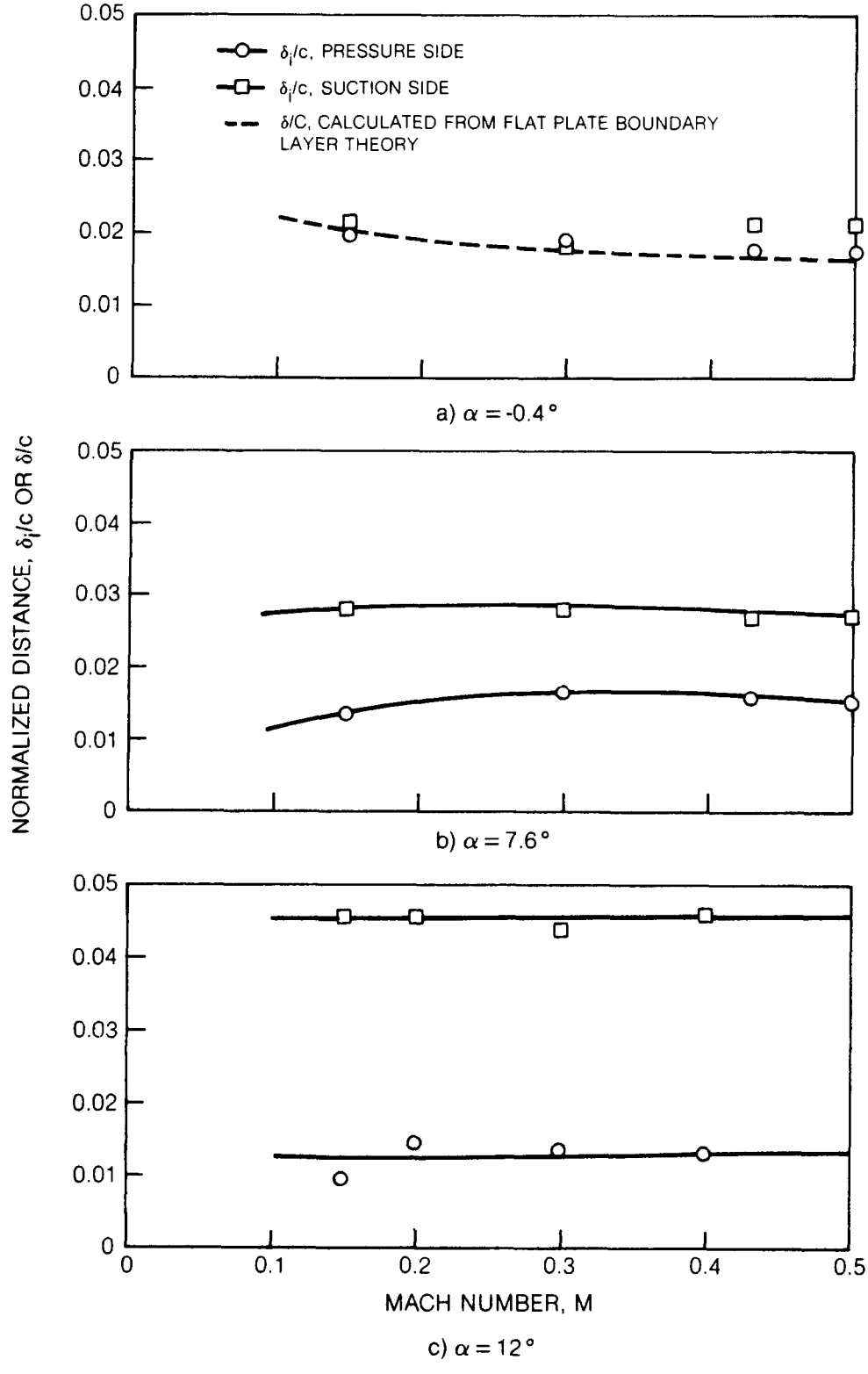

Figure 17 Normalized Boundary Layer Interface Distance Versus Mach Number and Angle of Attack for Rotor Blade Section

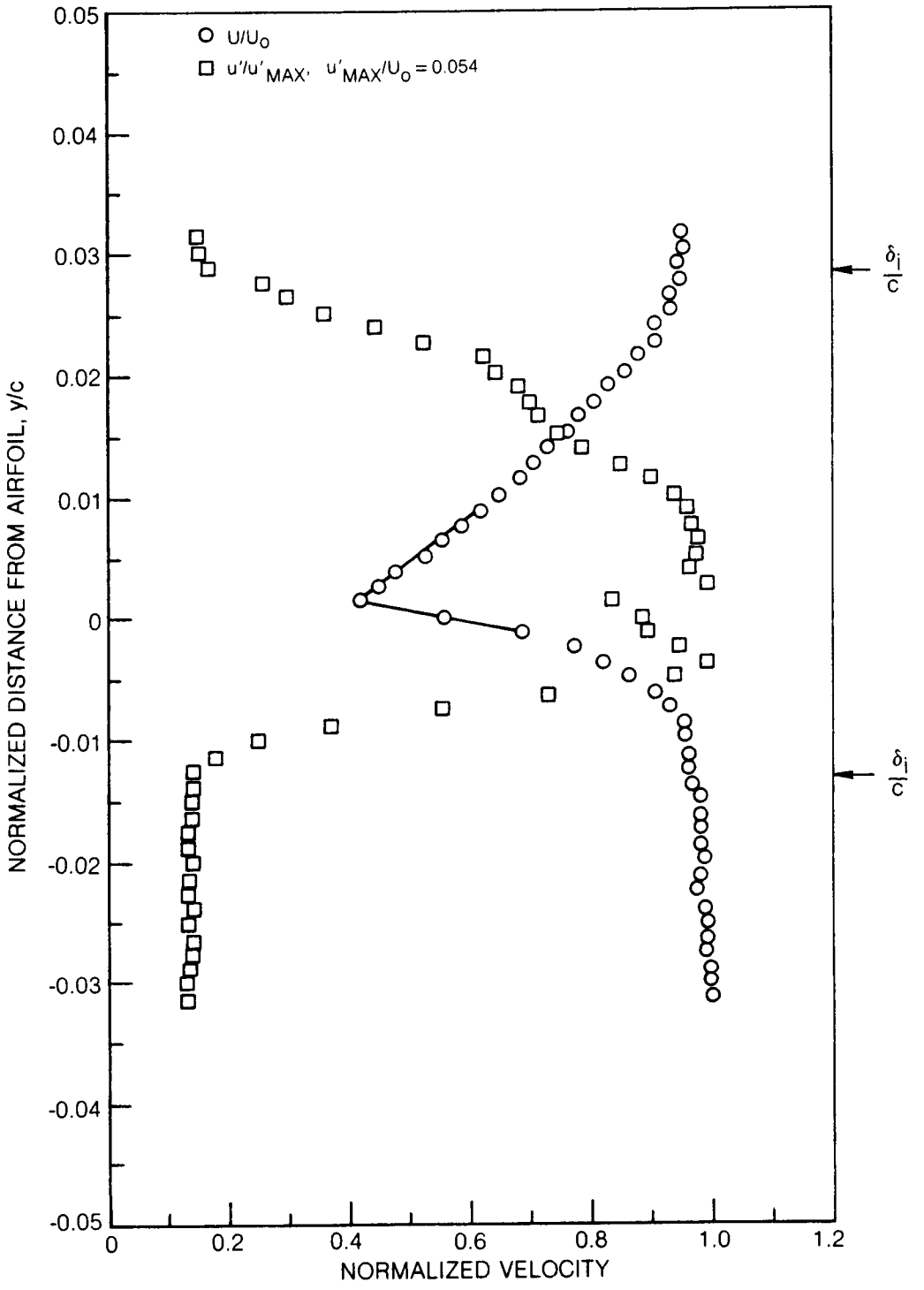

a) M = 0.15

Figure 18 **Normalized Mean Velocity and Turbulence Intensity Profiles for Rotor Blade Section, $\theta = 7.6°$**

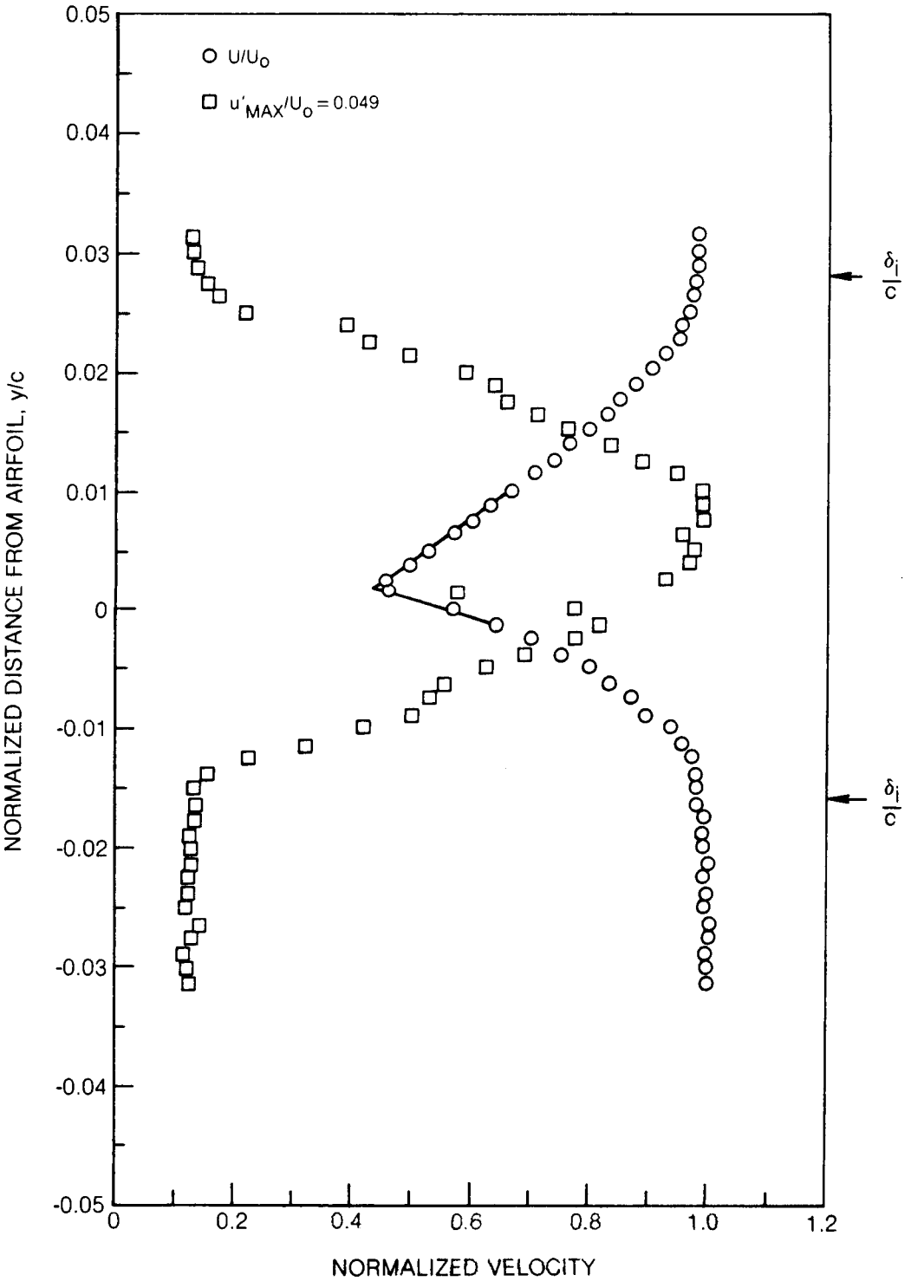

b) M = 0.3

Figure 18 — Continued

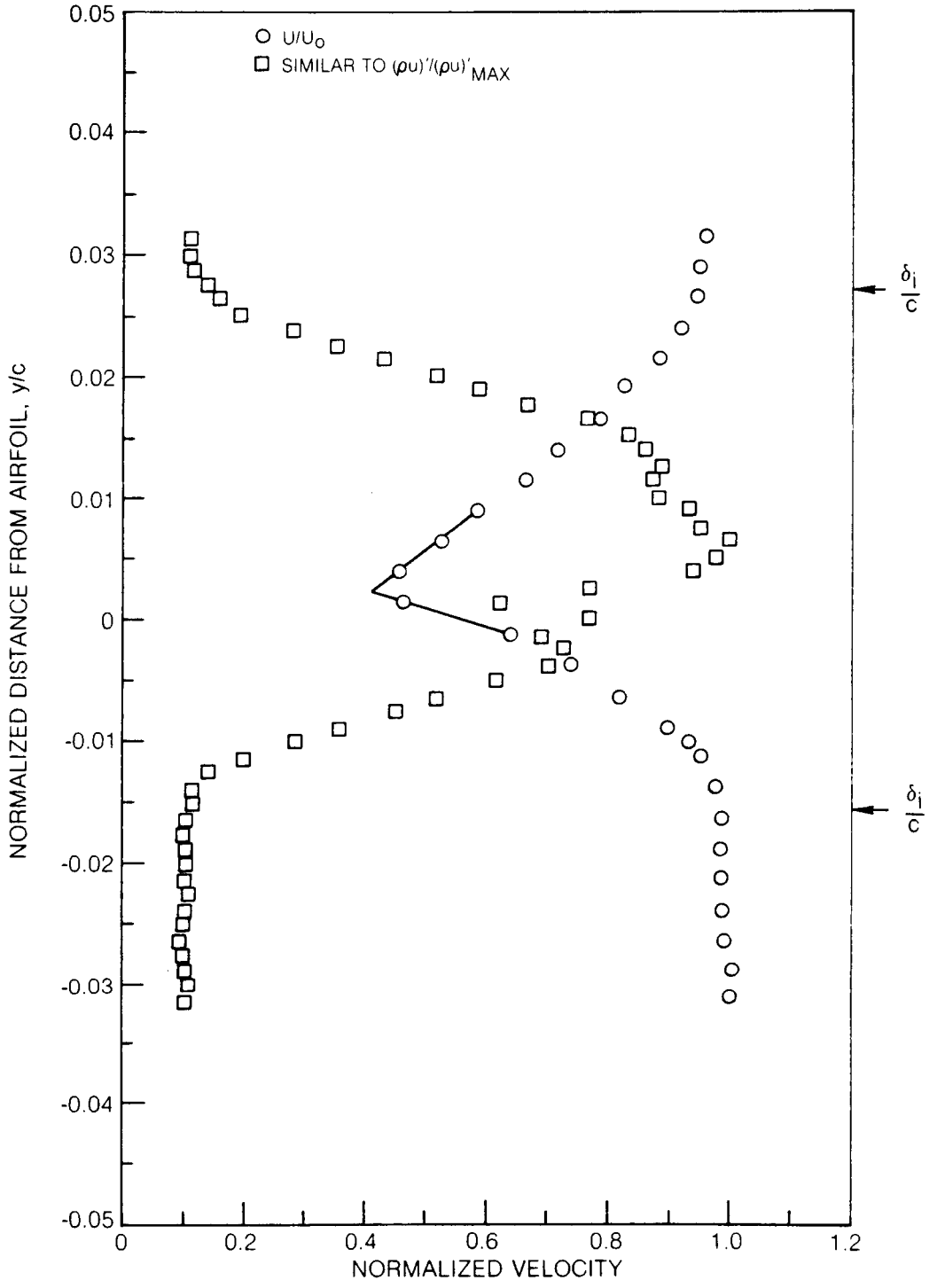

c) M = 0.43

Figure 18 — Continuèd

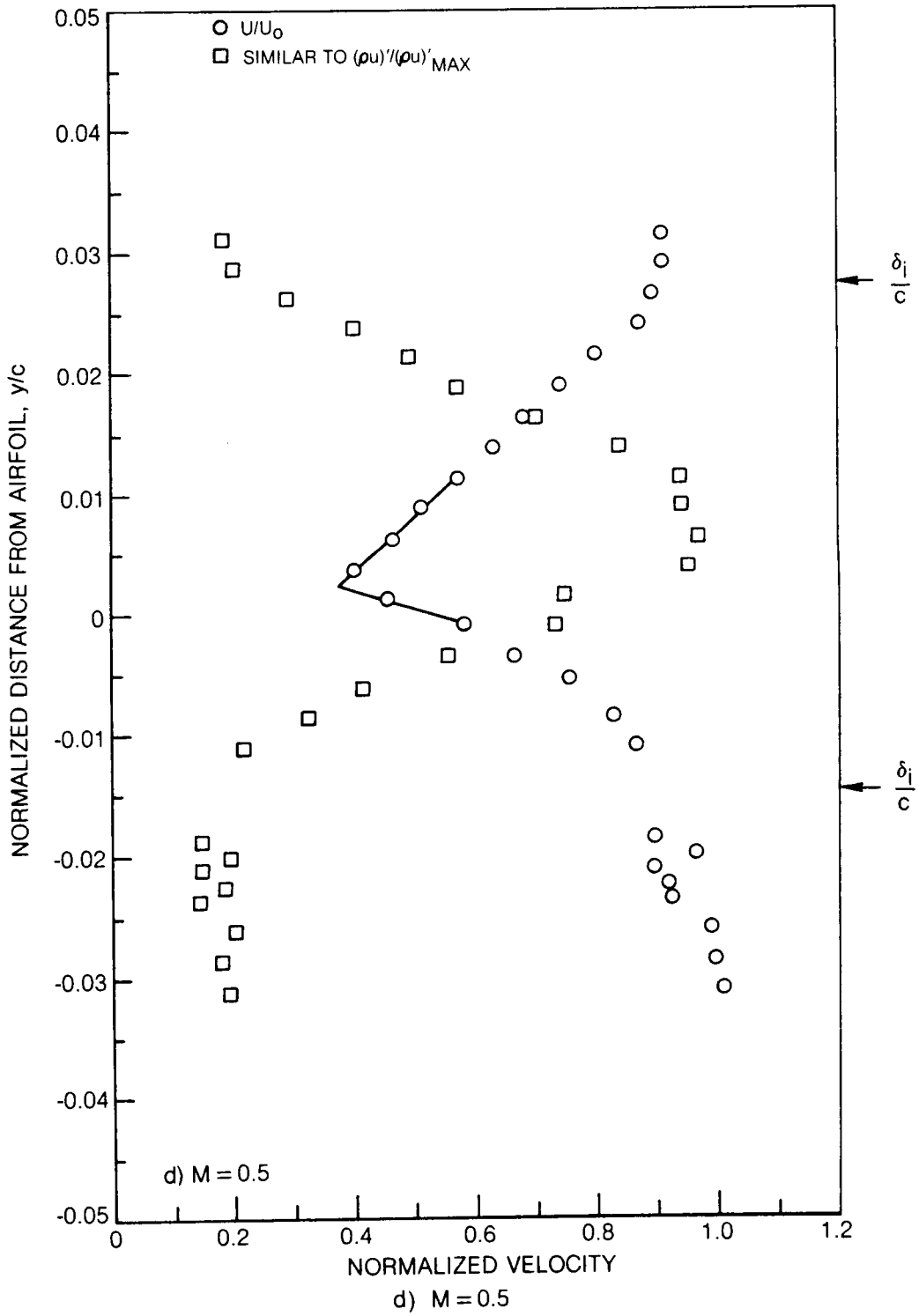

Figure 18 — Concluded

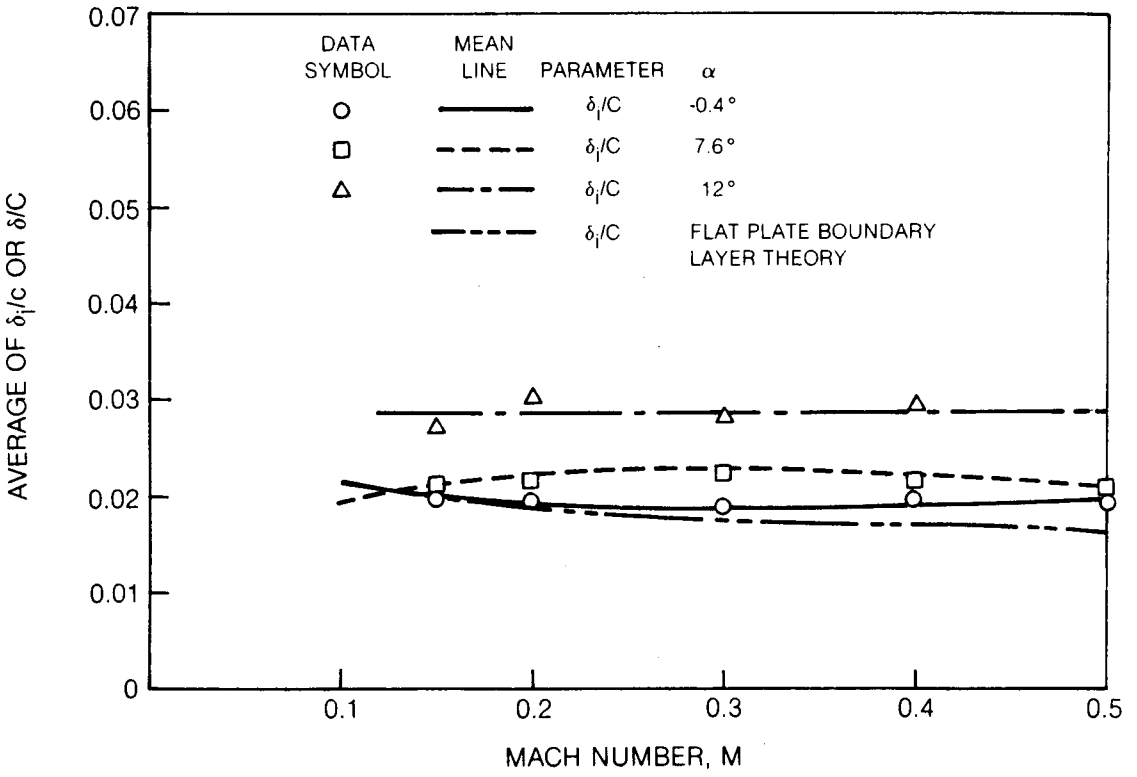

Figure 19 **Average of Normalized Boundary Layer Interface Distances on Pressure and Suction Side of Rotor Blade Section**

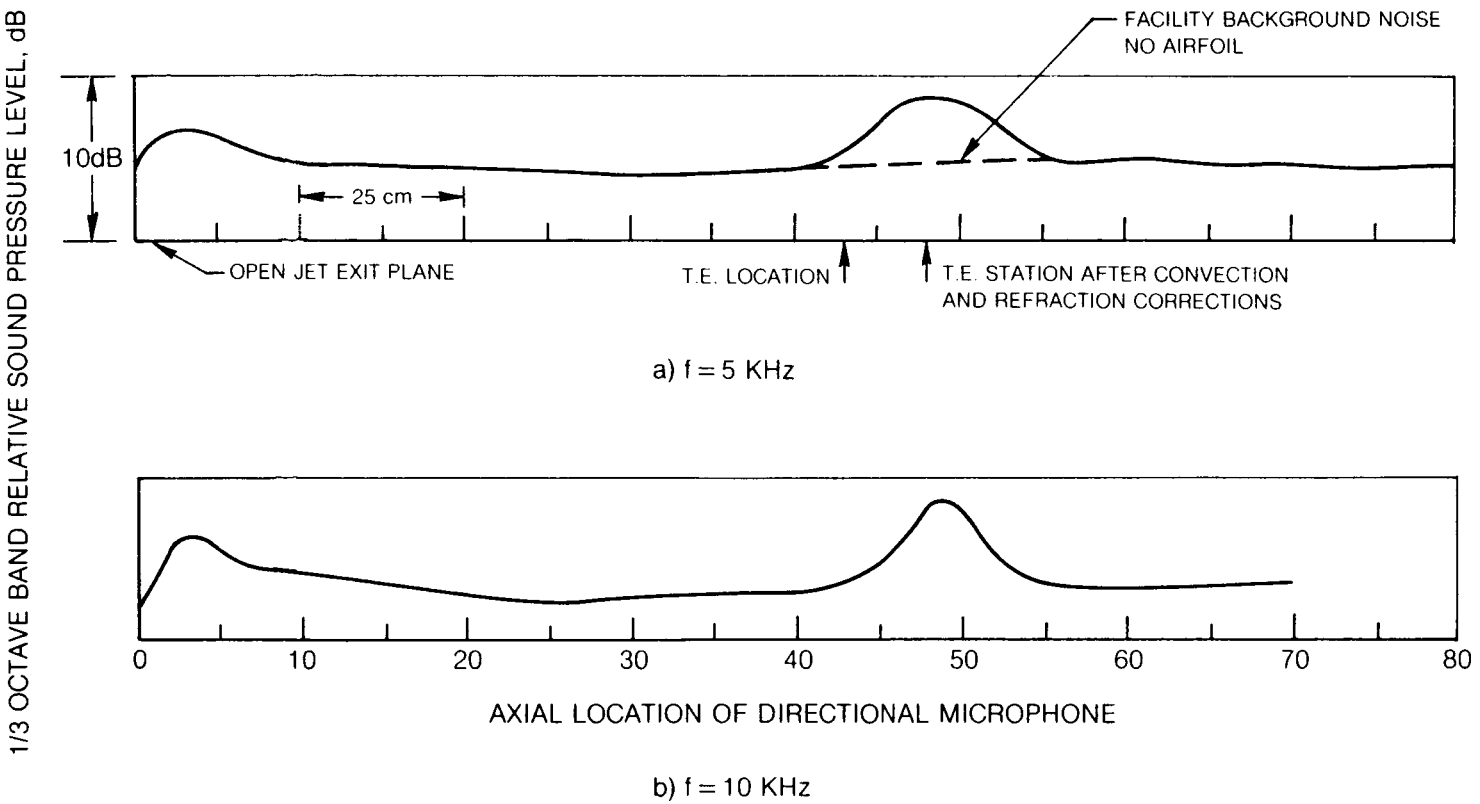

Figure 20 **Measured Axial Acoustic Source Distributions for Rotor Blade Section $M = 0.3$, $\theta_c = 90°$, $\alpha = -0.4°$**

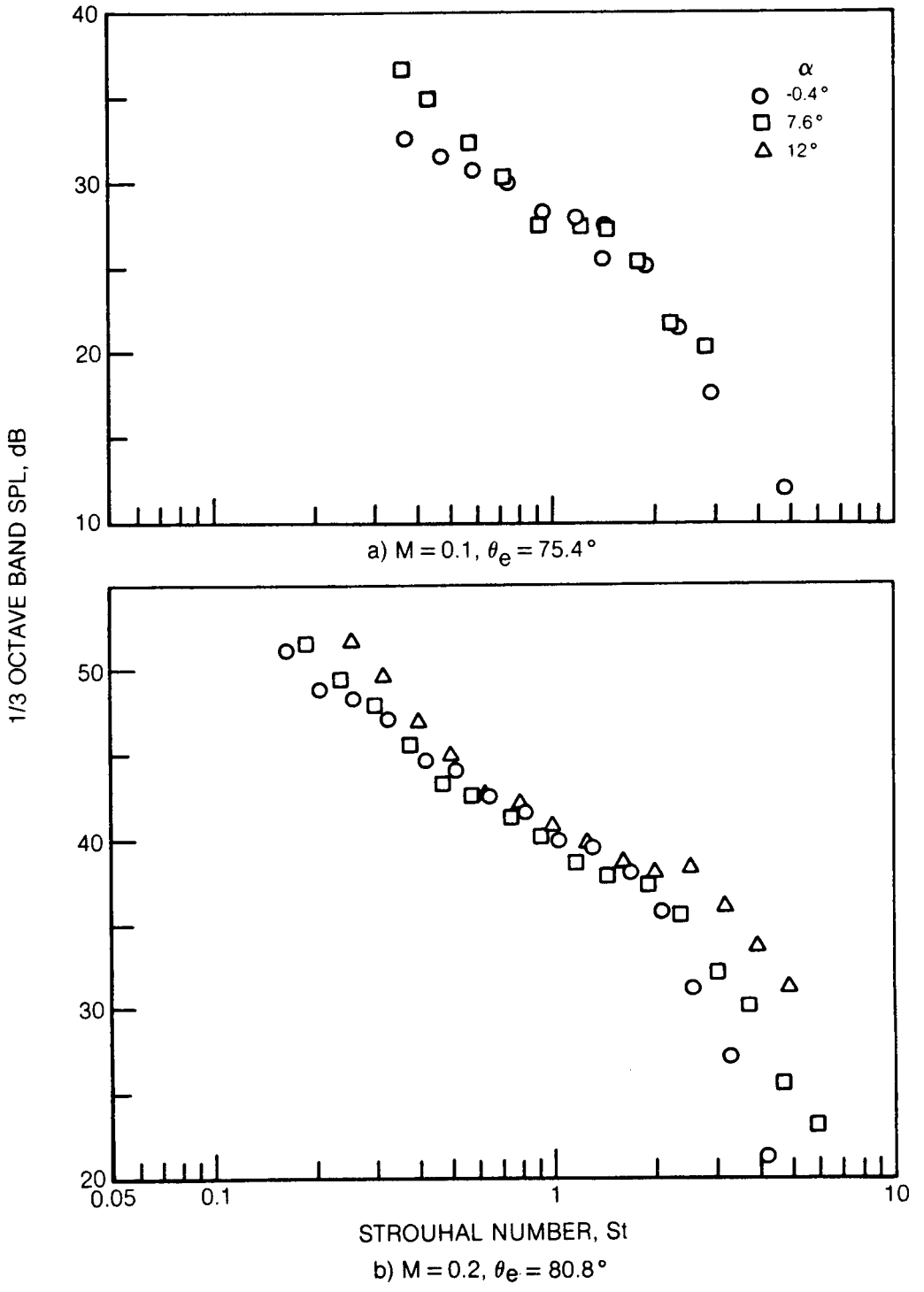

Figure 21 **Effect of Angle of Attack on 1/3 Octave Band Trailing Edge Noise Spectra for Rotor Blade Section at Various Mach Numbers, $\theta_c = 70°$**

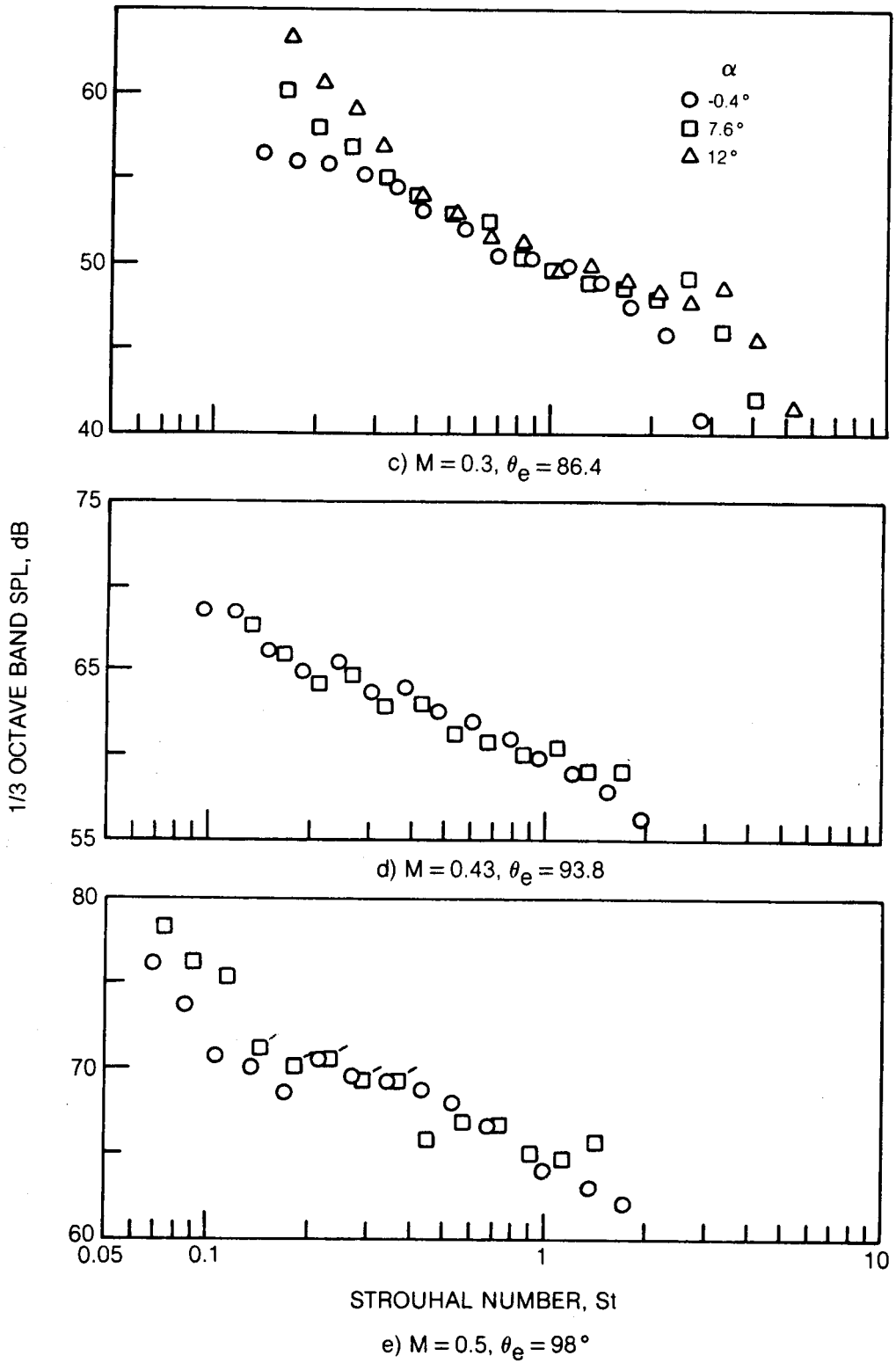

Figure 21 — Concluded

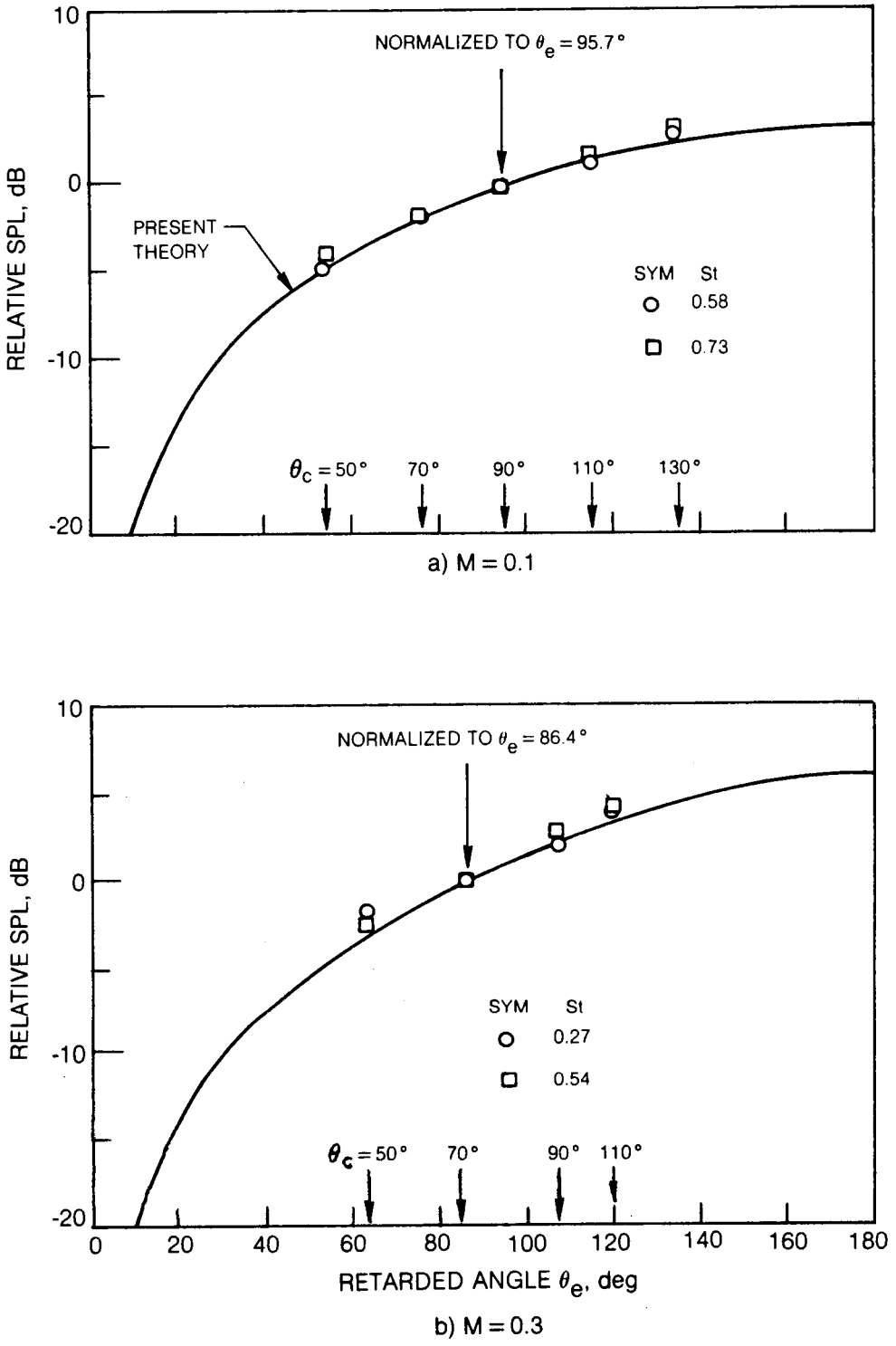

Figure 22 **Comparison of Measured and Theoretical Source Directivity as a Function of Mach Number for Rotor Blade Section, $\alpha = -0.4°$**

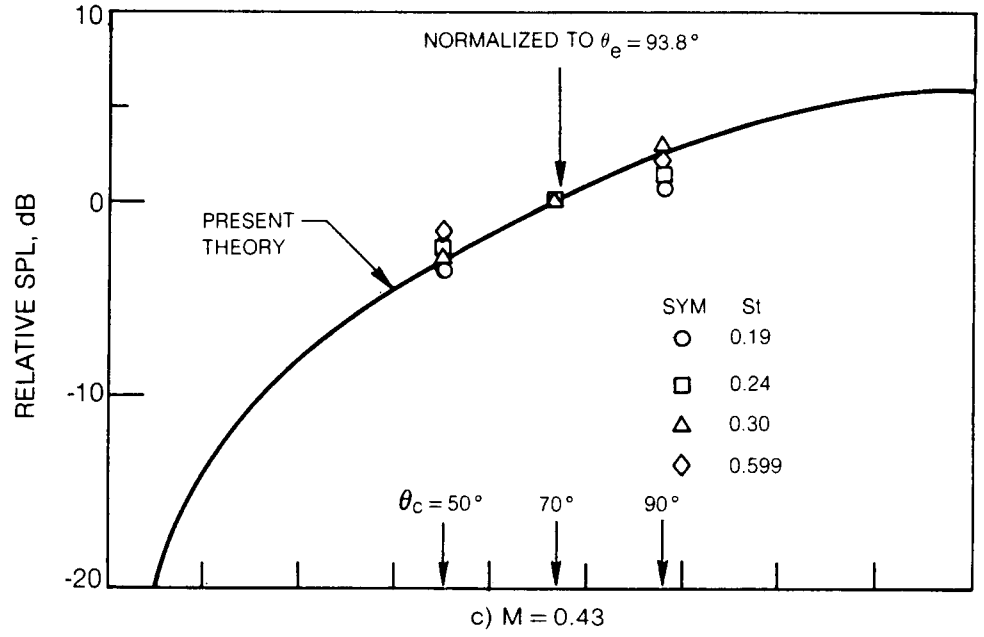

c) M = 0.43

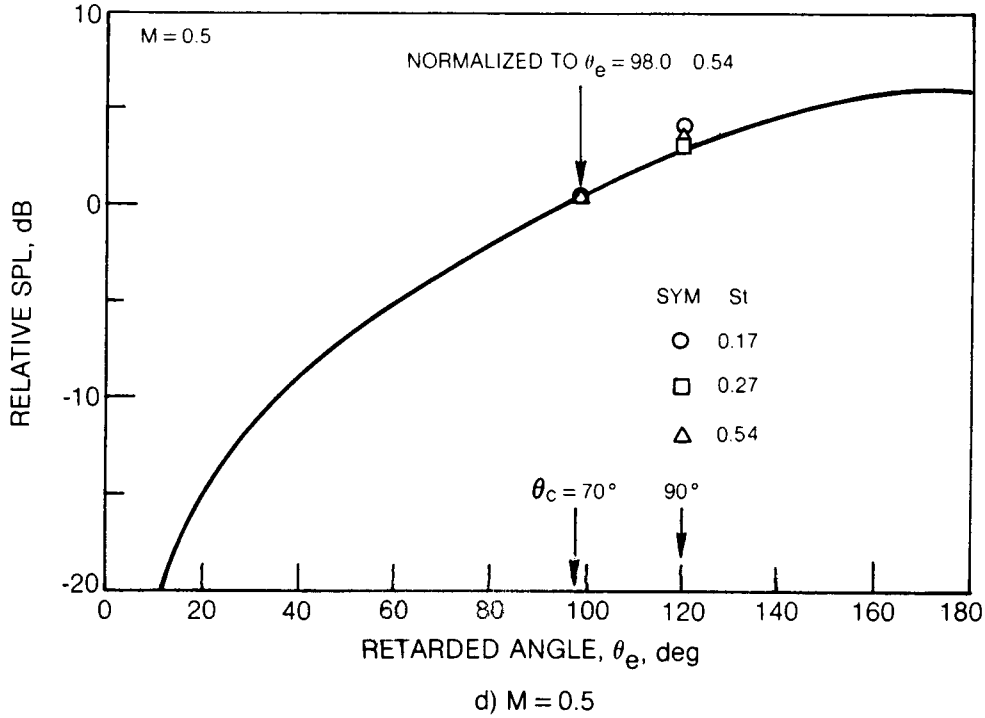

d) M = 0.5

Figure 22 — Concluded

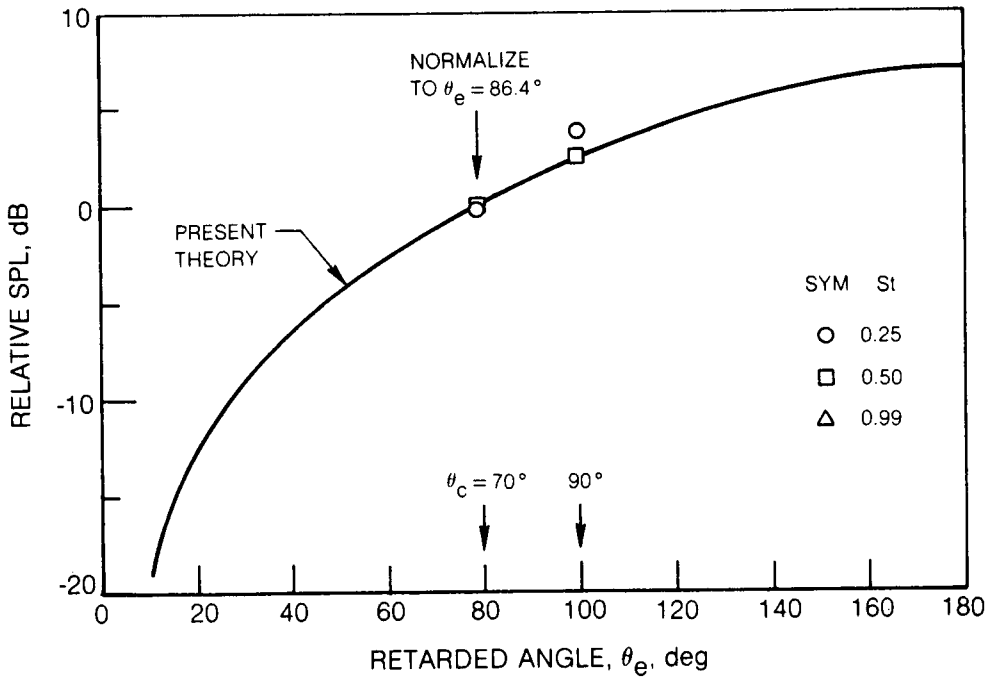

Figure 23 Comparison of Measured and Theoretical Source Directivity for Rotor Blade Section, M = 0.3, $\alpha = 7.6°$

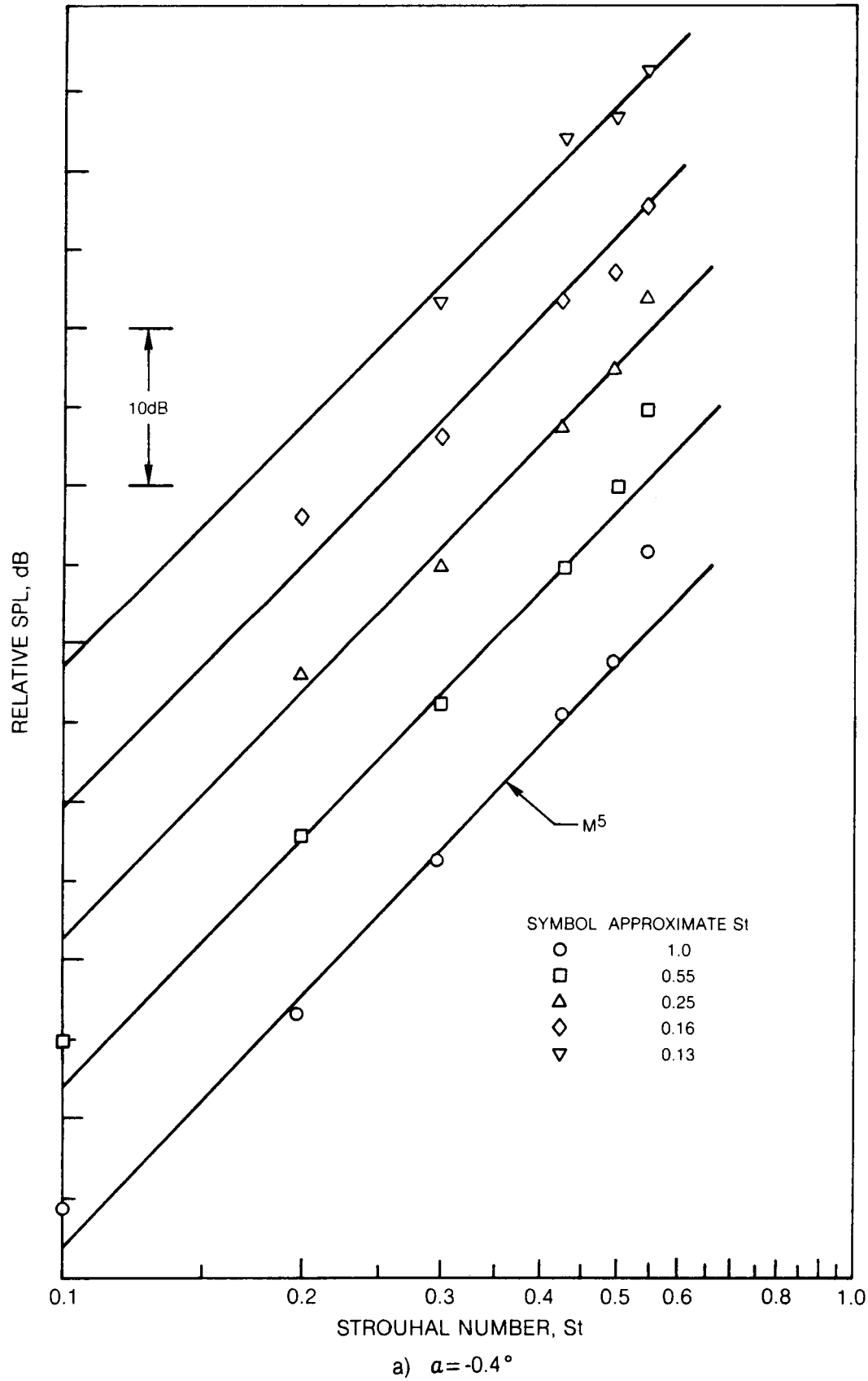

a) $\alpha = -0.4°$

Figure 24 Variation of 1/3 Octave Band Trailing Edge Noise Spectra with Mach Number for Rotor Blade Section, $\theta_e = 98°$

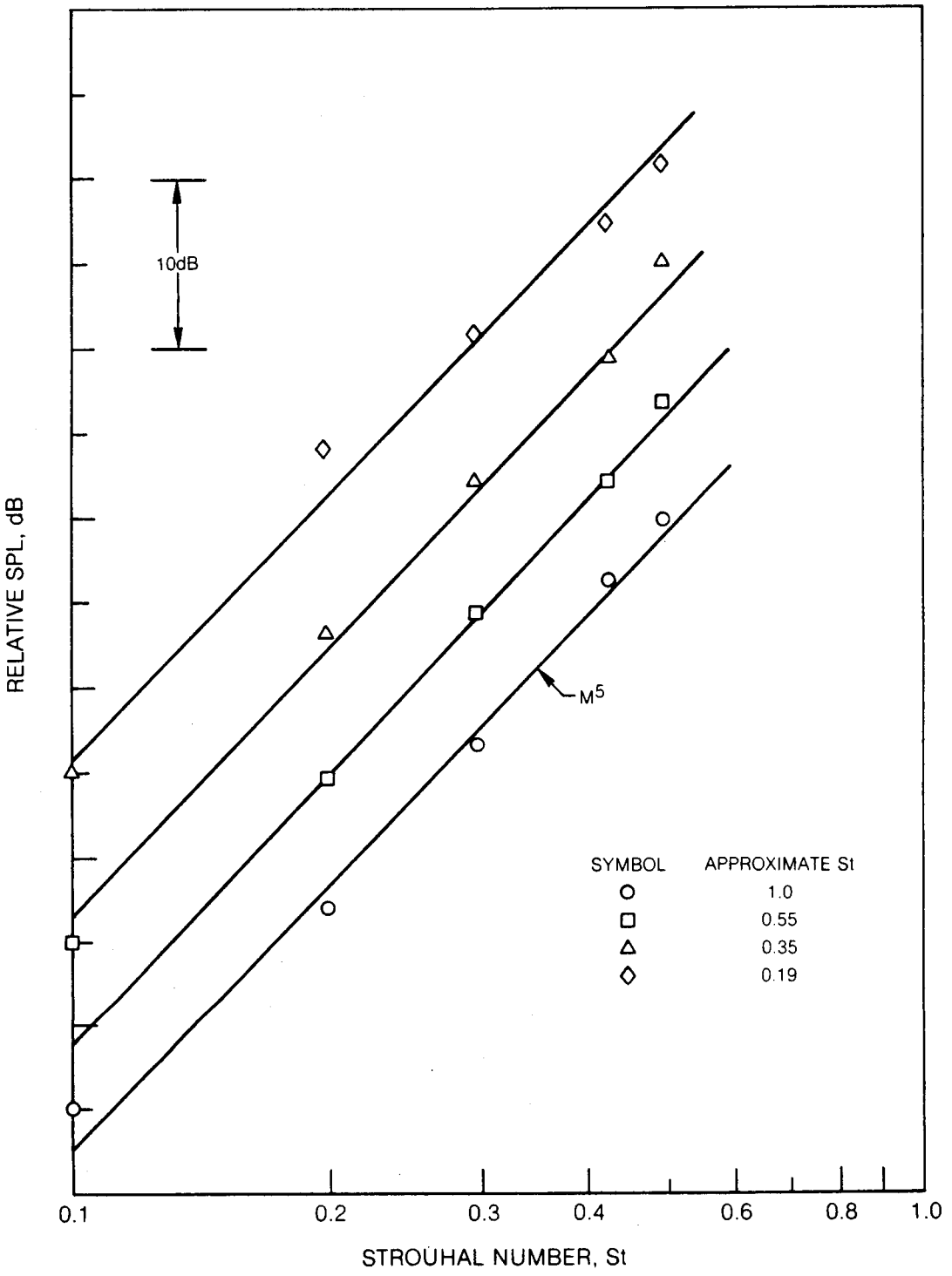

b) $\alpha = 7.6°$

Figure 24 — Concluded

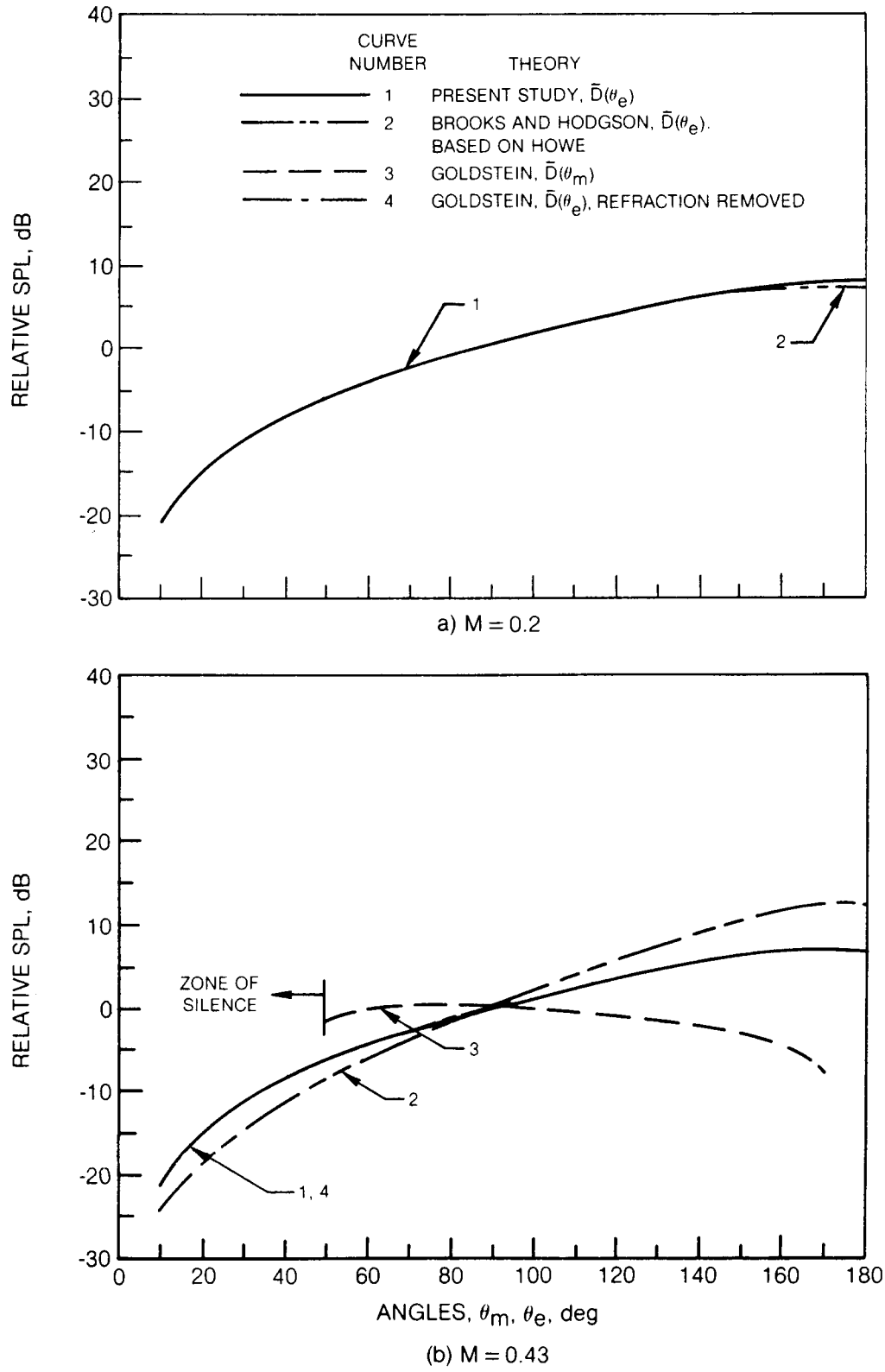

Figure 25 Comparison of Theoretical Trailing Edge Noise Source Directivity Patterns in Measured and Retarded Coordinate Systems

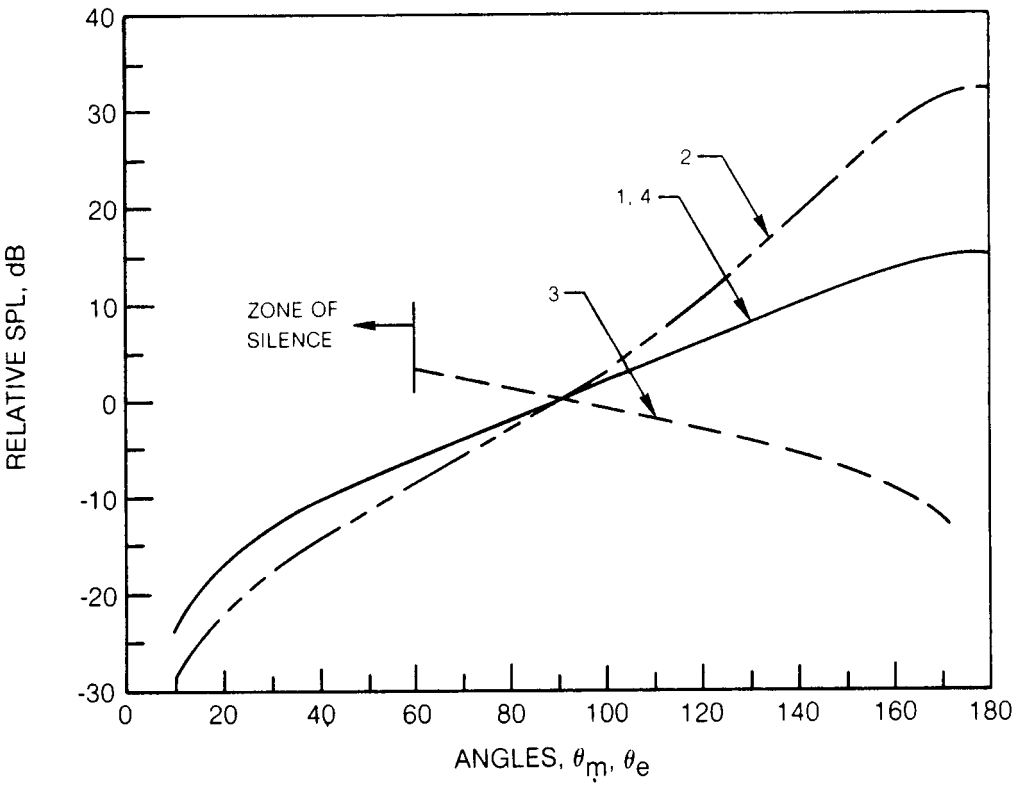

c) M = 0.86

Figure 25 — Concluded

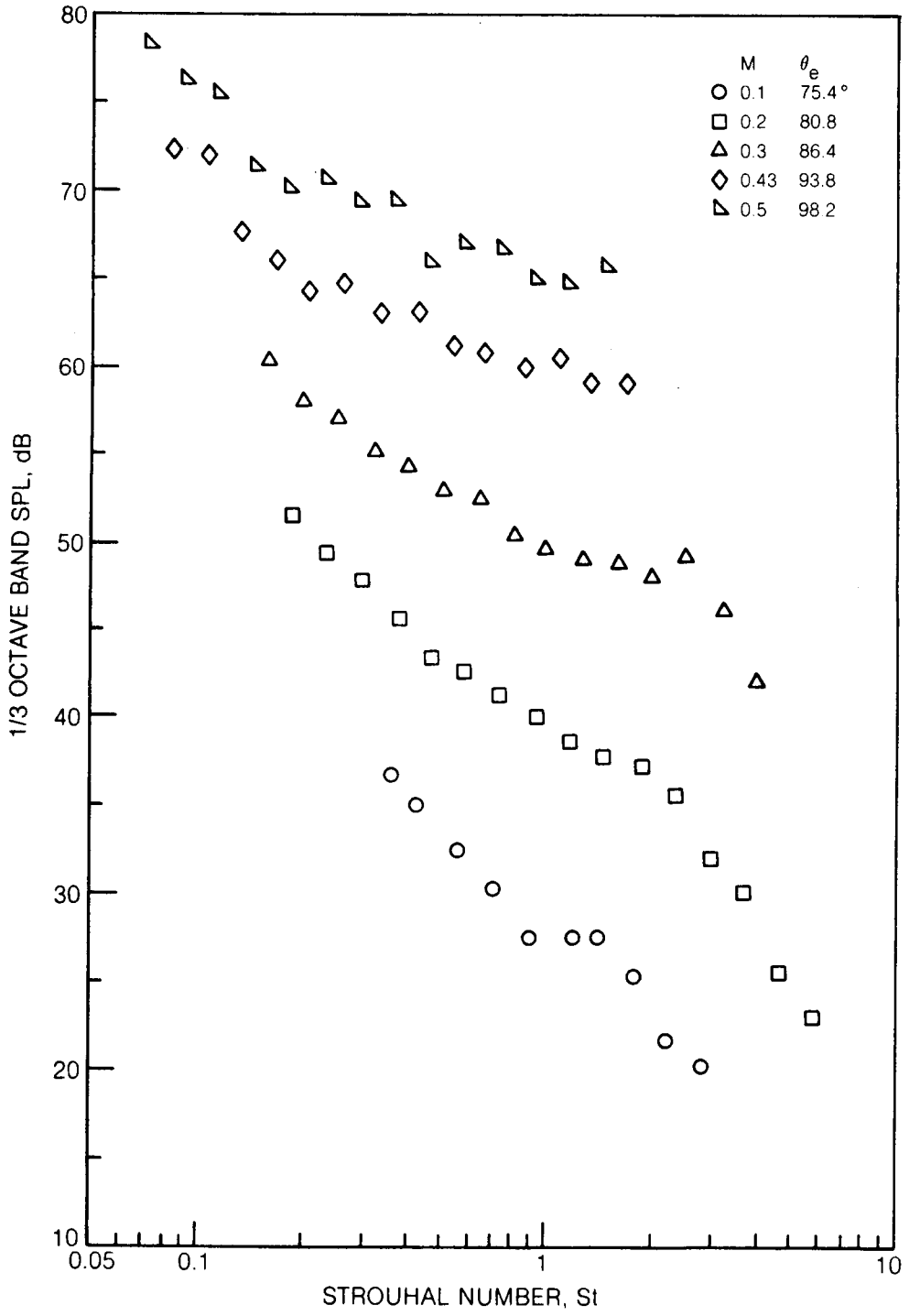

Figure 26 **One Third Octave Band Trailing Edge Noise Spectra for Rotor Blade Section, $\theta_c = 70°$, $\alpha = 7.6°$, $r_e = 3m$**

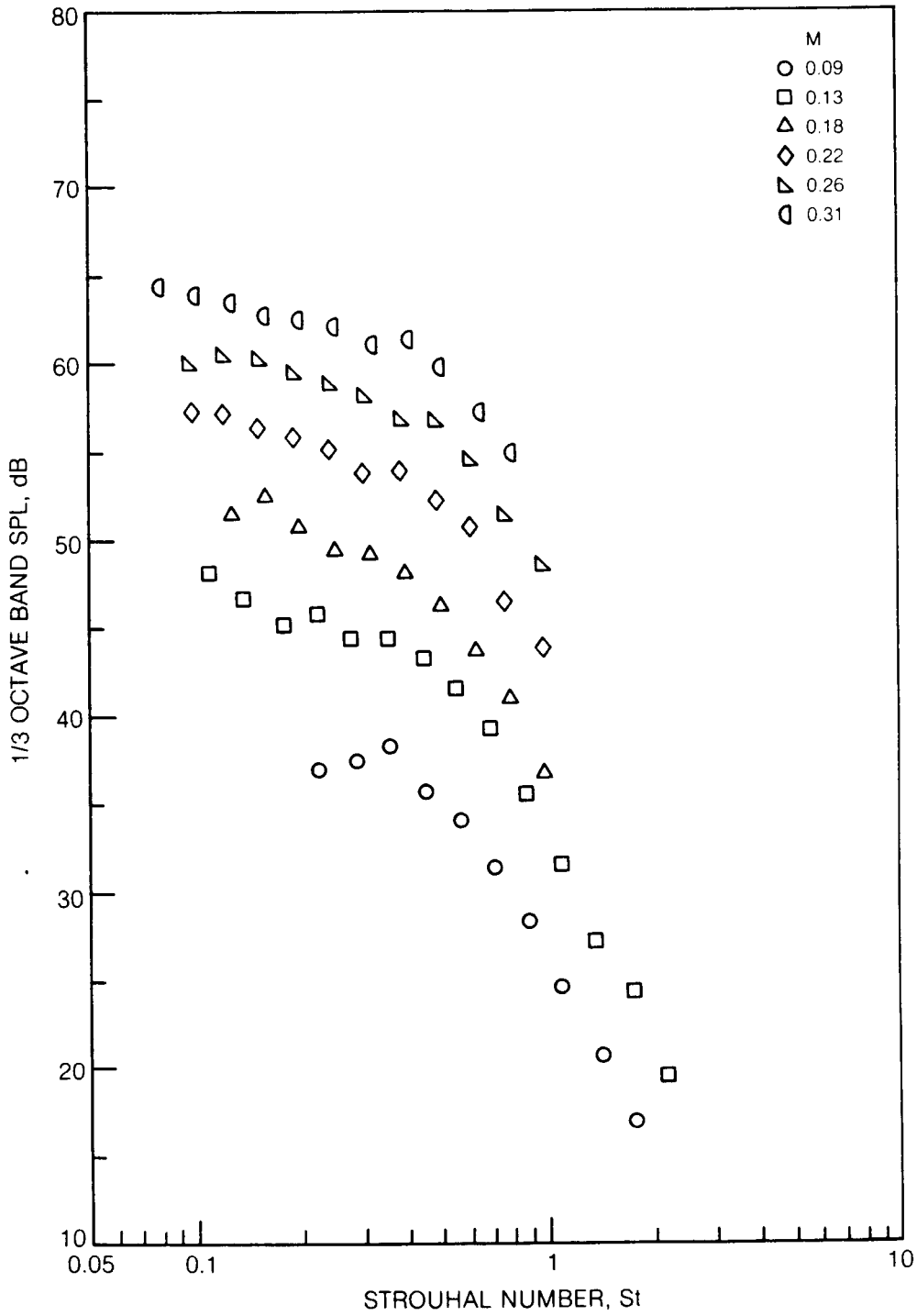

Figure 27 **One Third Octave Band Noise Spectra for NACA 0012 Data Reported by Schlinker, $\theta_e = 90°$, $\alpha = 6°$, $r_e = 2.81m$**

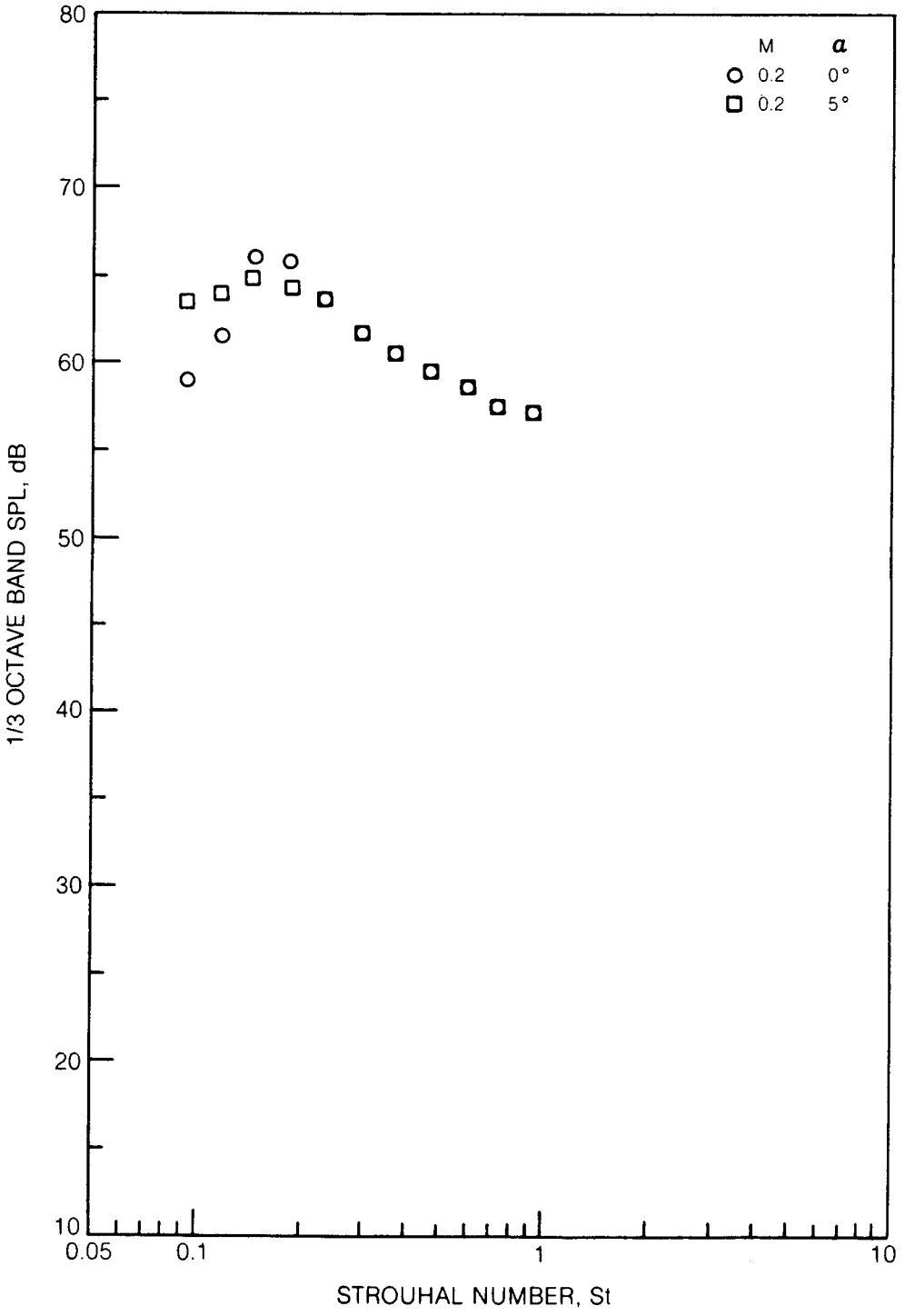

Figure 28 — One Third Octave Band Trailing Edge Noise Spectra for NACA 0012 Data Reported by Brooks, $\theta_e = 90°$, $r_e = 1.22m$

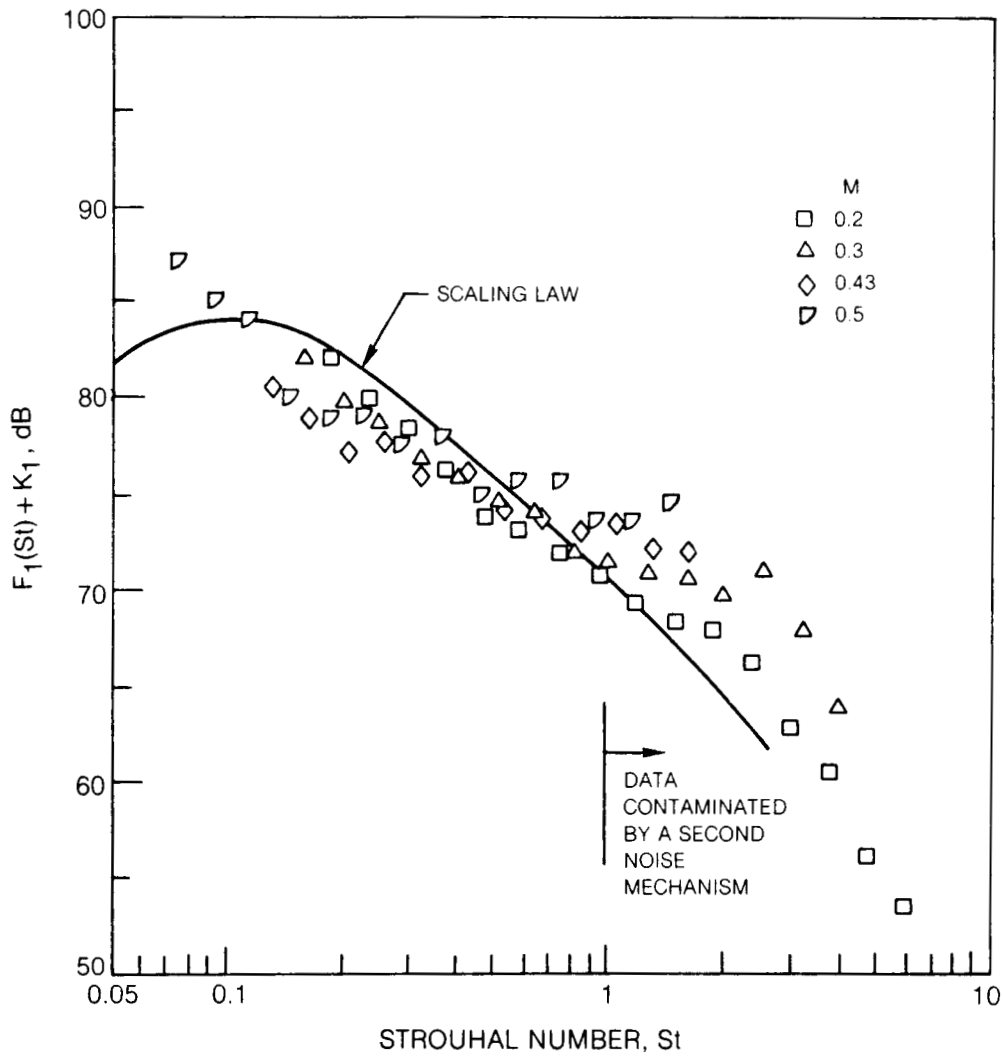

Figure 29 **Normalized 1/3 Octave Band Trailing Edge Noise Spectra for Rotor Blade Section, $\theta_e = 98°$, $\alpha = 7.6°$, $r_e = 3m$**

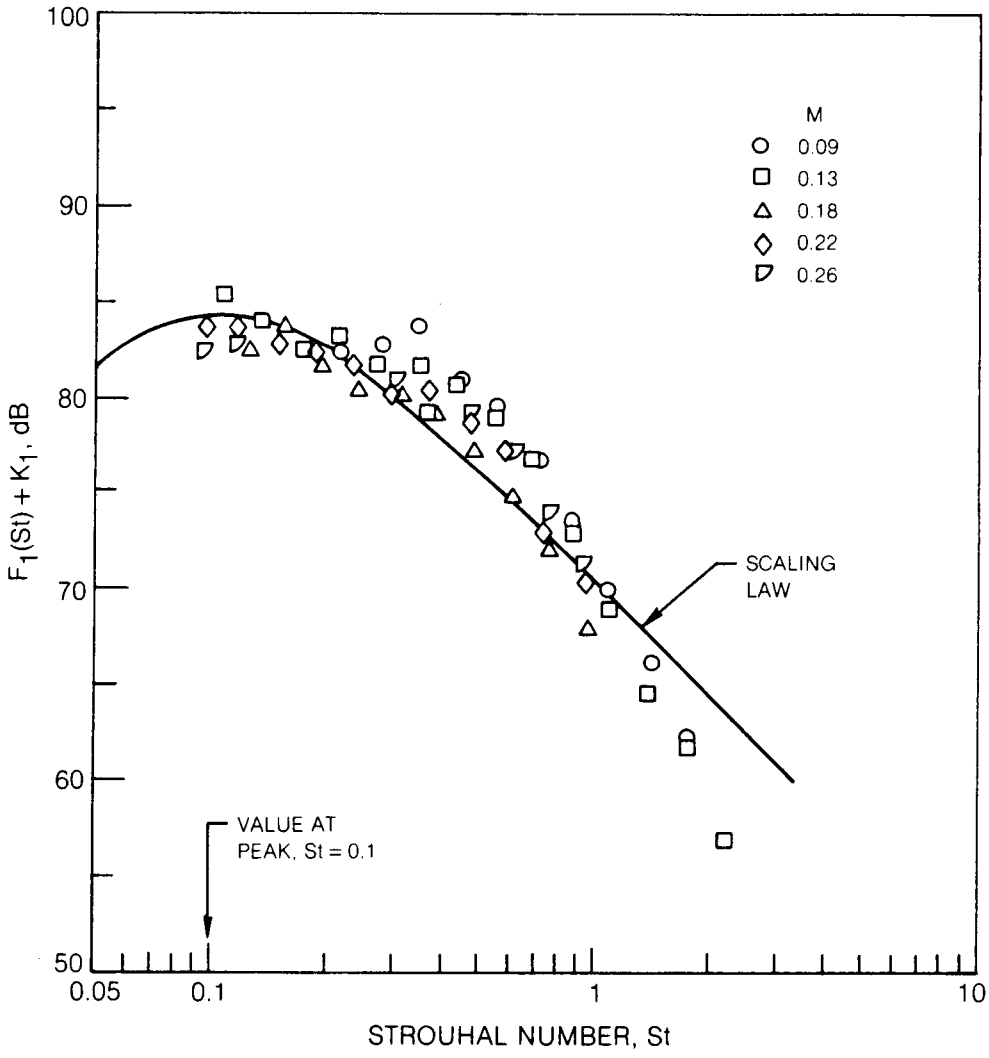

Figure 30 **Normalize 1/3 Octave Band Trailing Edge Noise Spectra for NACA 0012 Airfoil Data Reported by Schlinker, $\theta_e = 90°$, $\alpha = 6°$, $r_e = 2.81$ m**

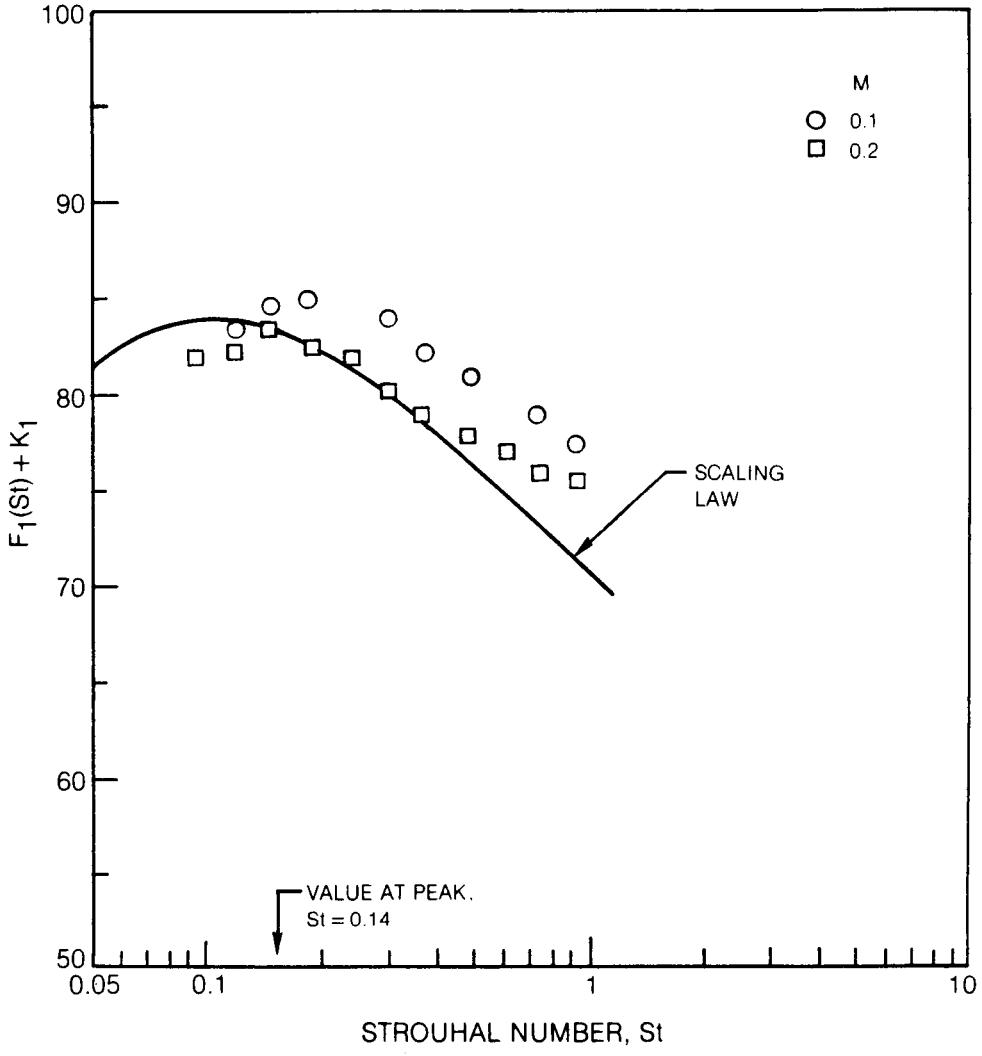

Figure 31 **Normalized 1/3 Octave Band Trailing Edge Noise Spectra for NACA 0012 Data reported by Brooks, $\theta_e = 90°$, $\alpha = 5°$, $r_e = 1.22$ m**

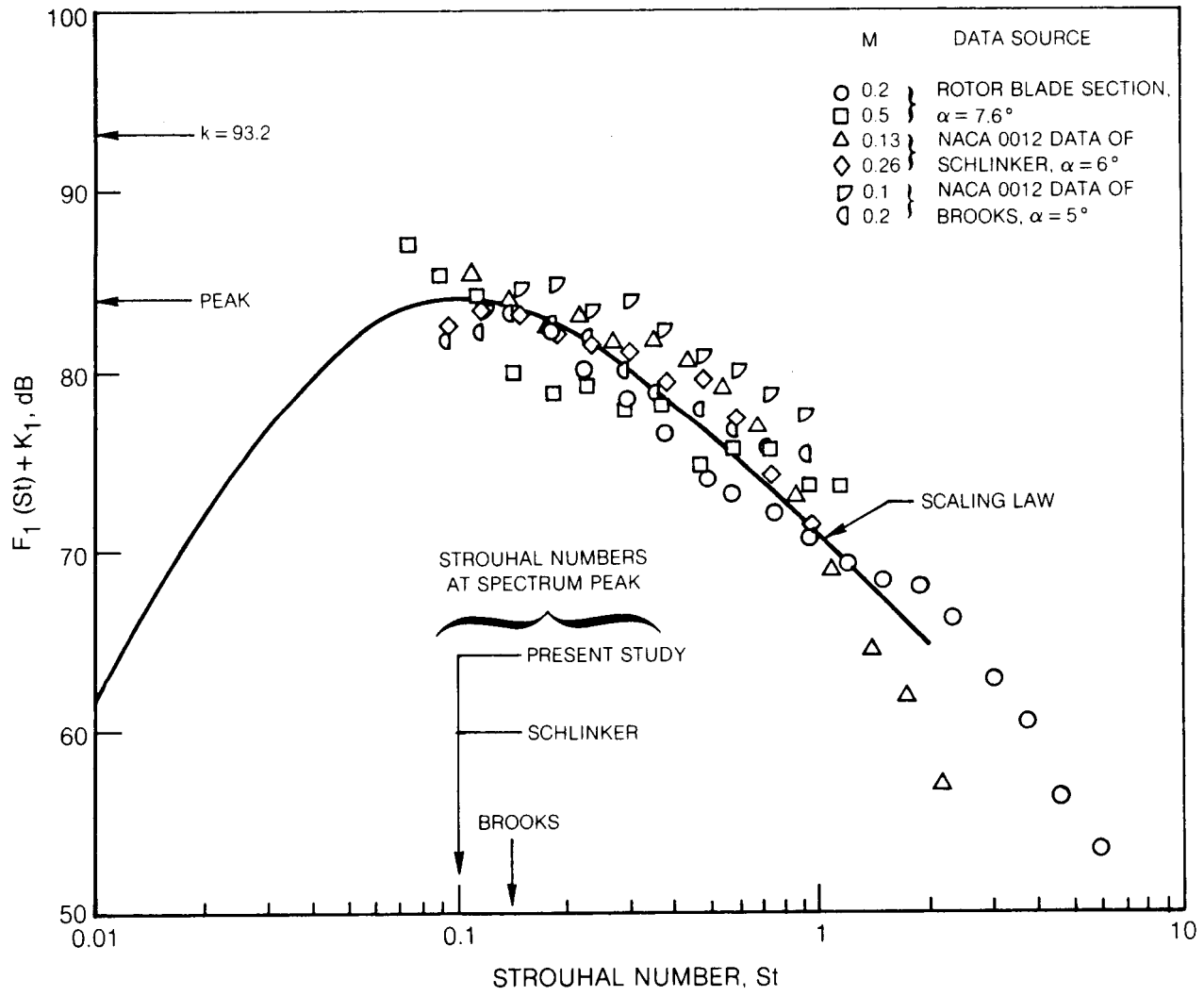

Figure 32 Comparison of Normalized 1/3 Octave Band Trailing Edge Noise Spectra Measured by Various Investigators, $\theta_e = 90°$

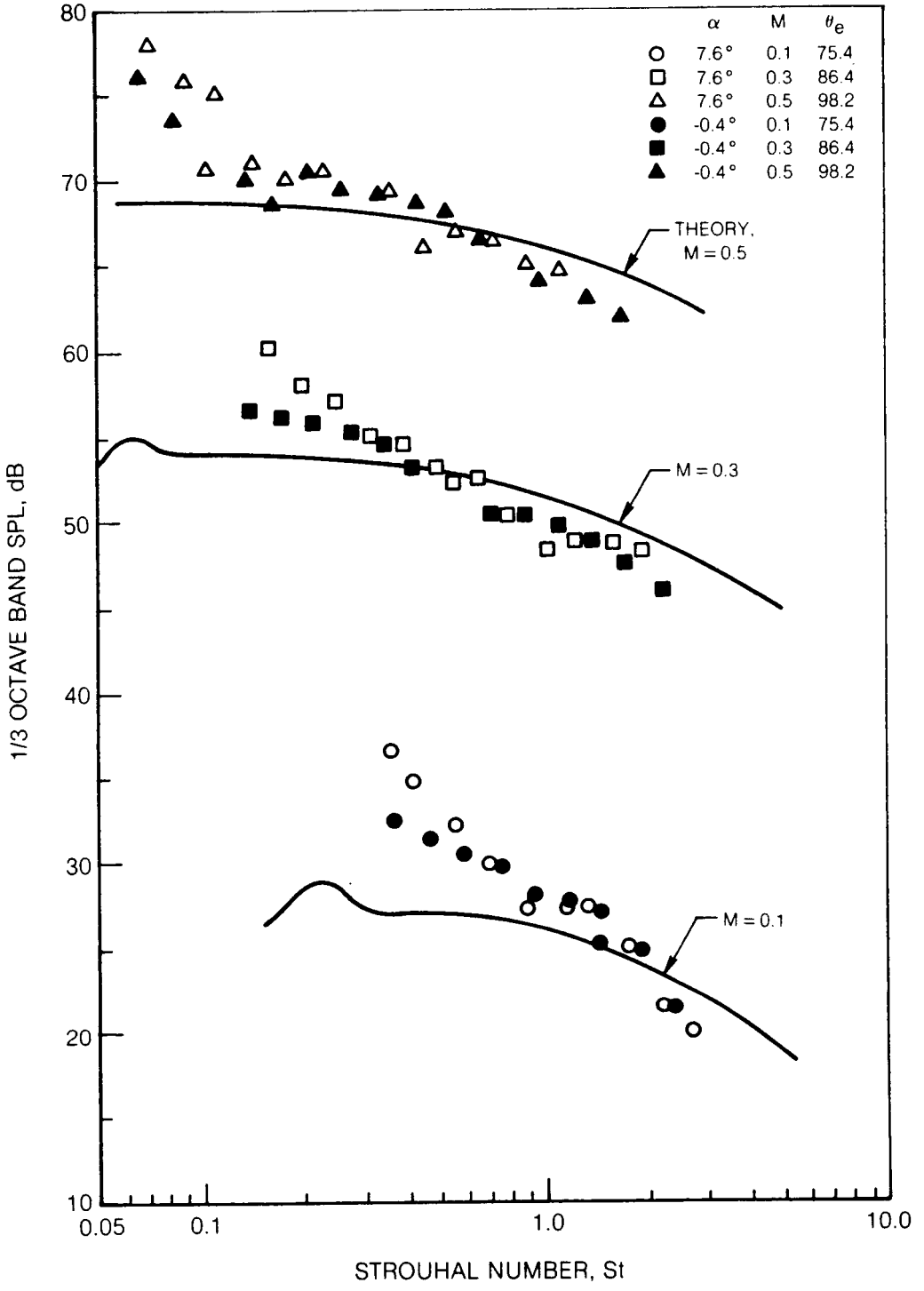

a) THEORY USING FLAT PLATE SURFACE PRESSURE SPECTRUM

Figure 33 **Comparison of Measured and Theoretical 1/3 Octave Band Noise Spectra for Rotor Blade Section, $\theta_c = 70°$, $\alpha = 7.6°$, $r_e = 3$ m**

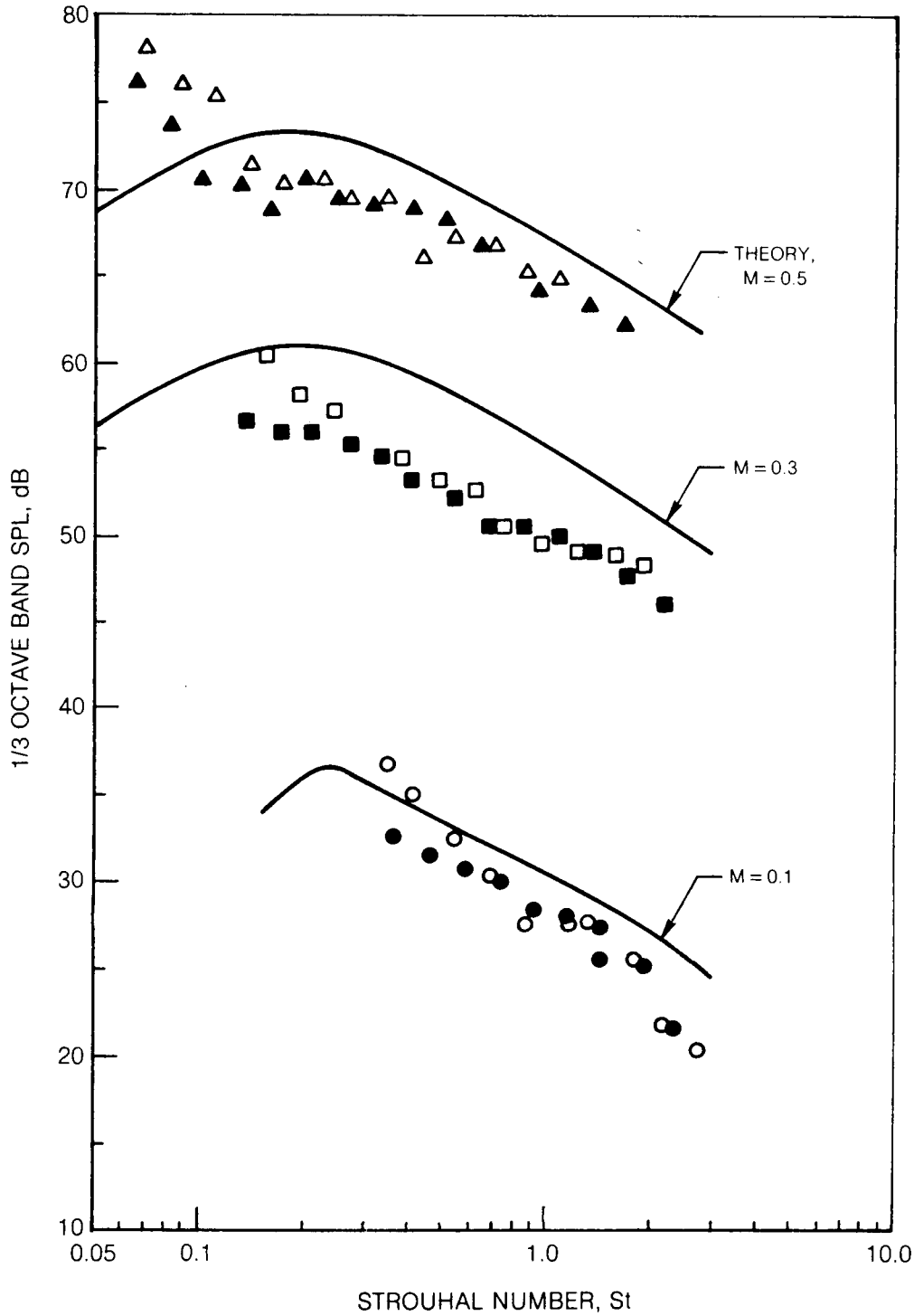

b) THEORY USING AIRFOIL SURFACE PRESSURE SPECTRUM

Figure 33 — Concluded

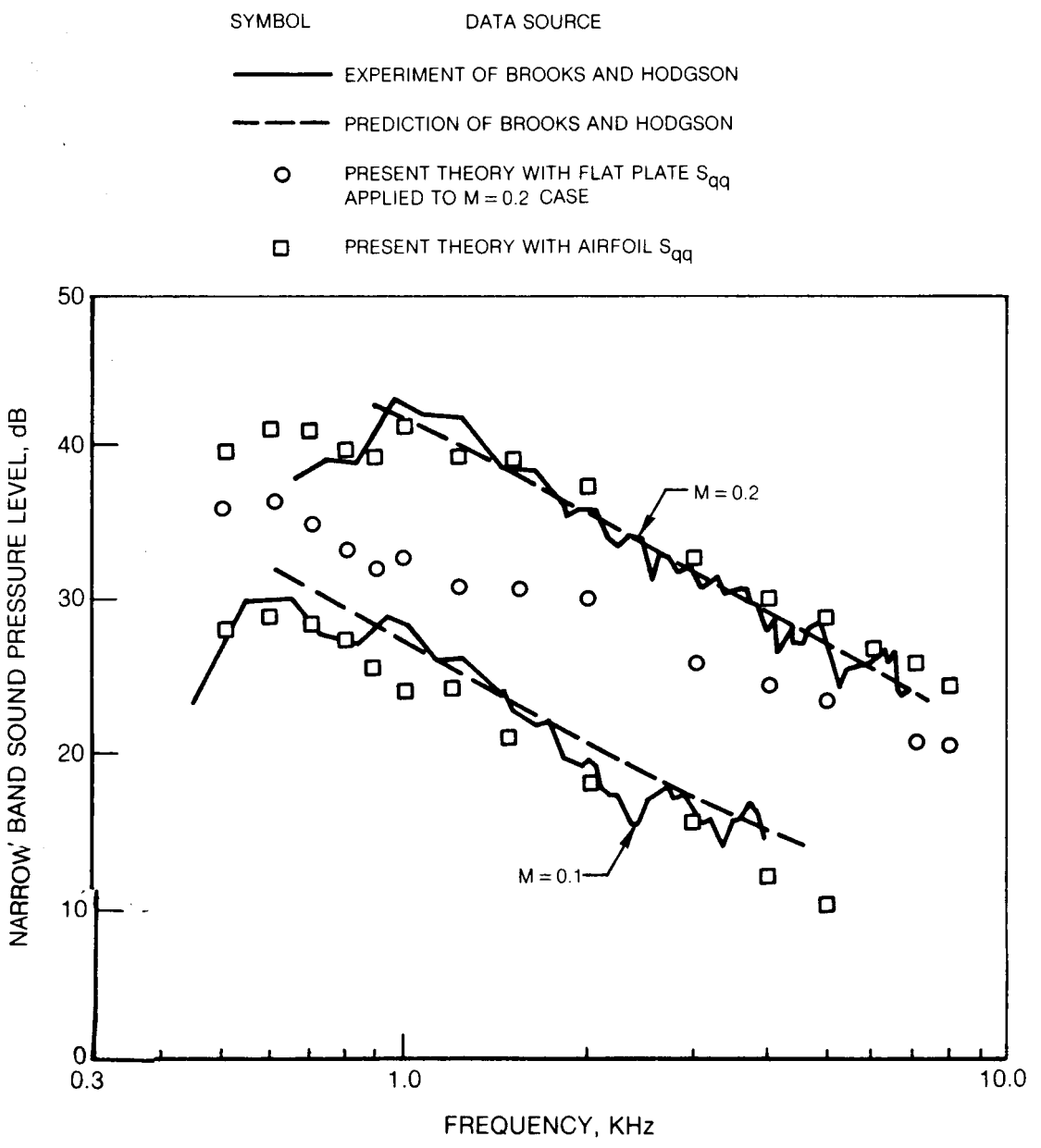

Figure 34 **Comparison of Present Theory with Results of Brooks and Hodgson, $\theta_e = 90°$, $\alpha = 0°$, $r_e = 1.22$ m, Bandwidth: 1 Hz**

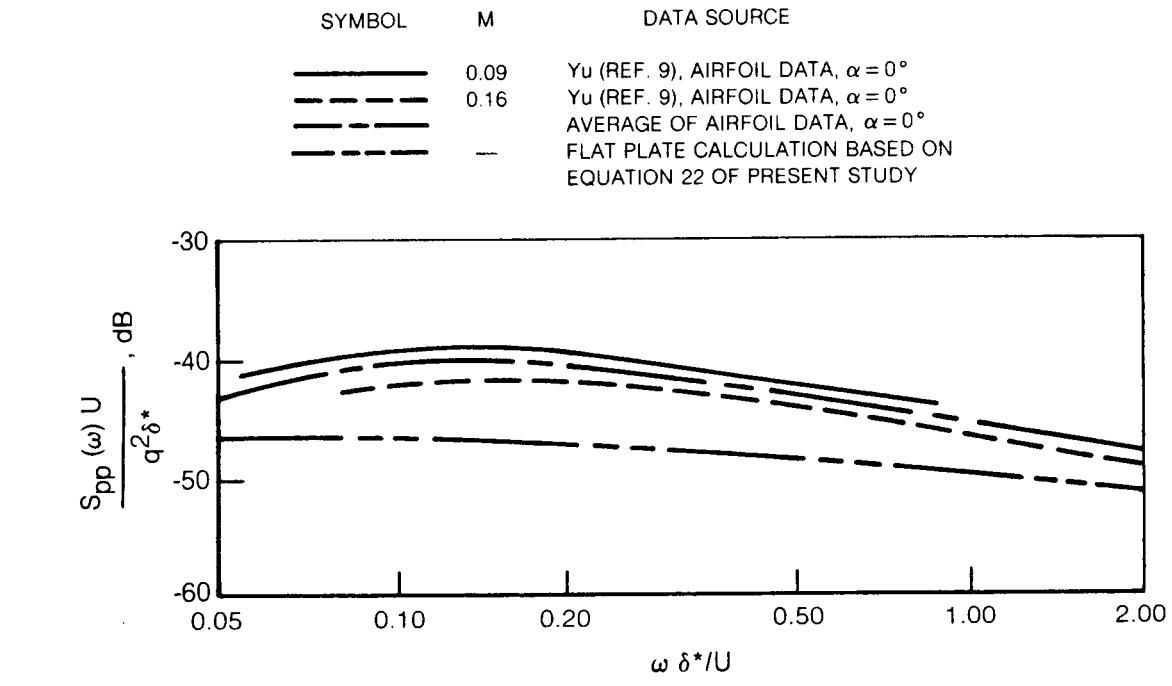

a) AIRFOIL AND FLAT PLATE SPECTRA

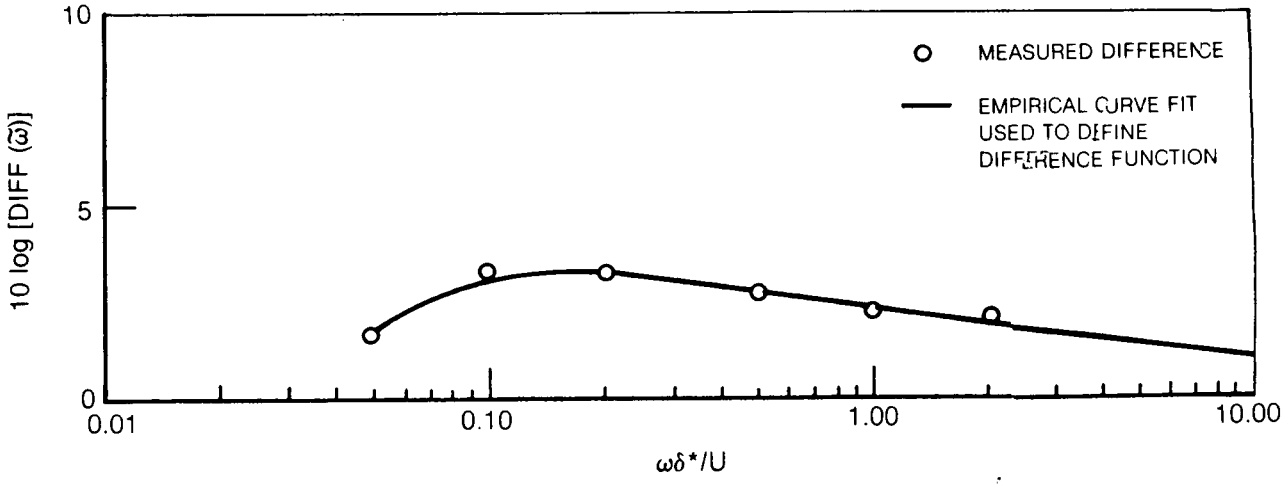

b) DIFFERENCE BETWEEN AIRFOIL AND FLAT PLATE SPECTRUM LEVELS

Figure 35 Comparison of Airfoil and Flat Plate Normalized Surface Pressure Spectra, Bandwidth, 1 Hz

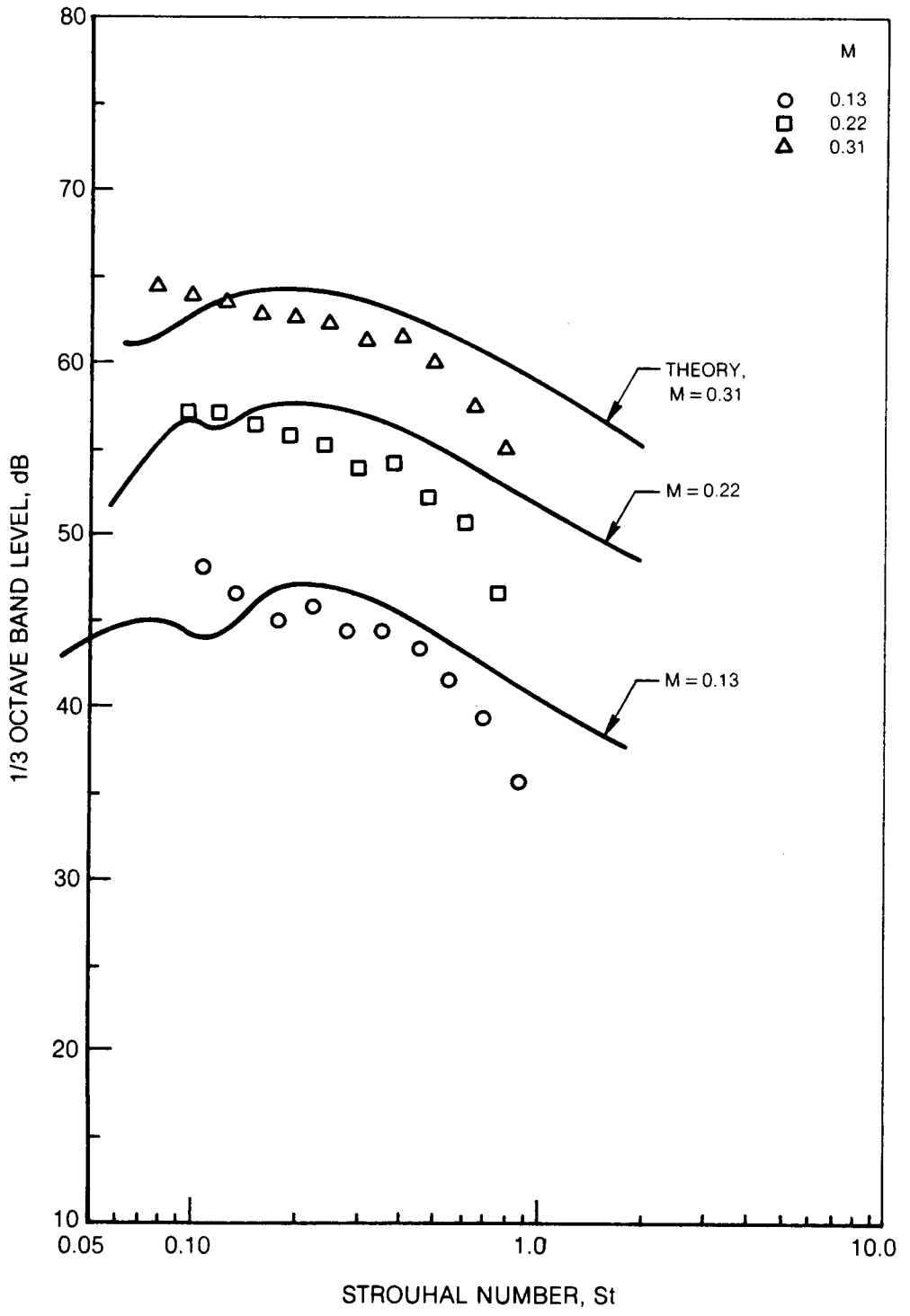

Figure 36 Comparison of Measured and Present Theoretical Prediction for NACA 0012 Data Reported by Schlinker, $\theta_e = 90°$, $\alpha = 6°$, $r_e = 2.81$ m

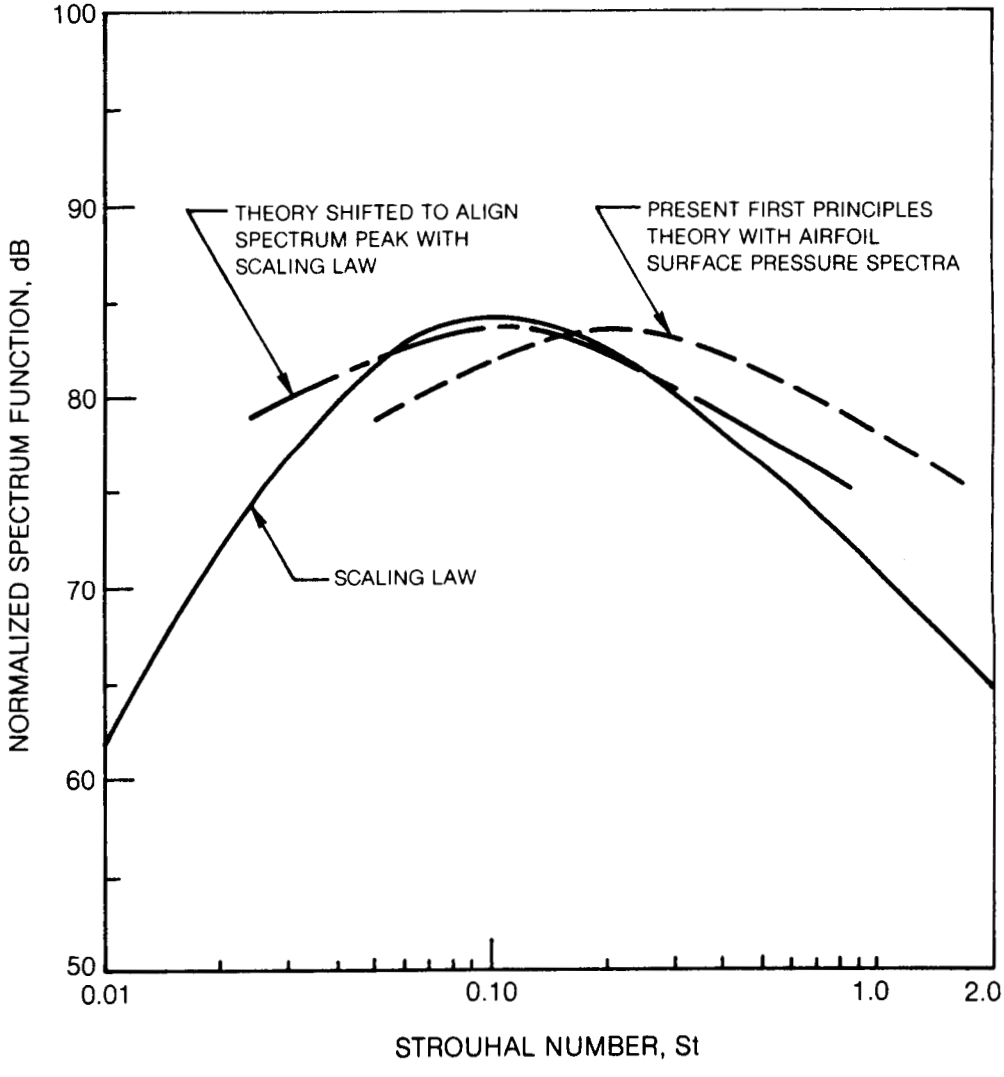

Figure 37 **Comparison of Normalized 1/3 Octave Band Spectrum Functions for First Principles Theory and the Scaling Law, $\theta_e = 90°$**

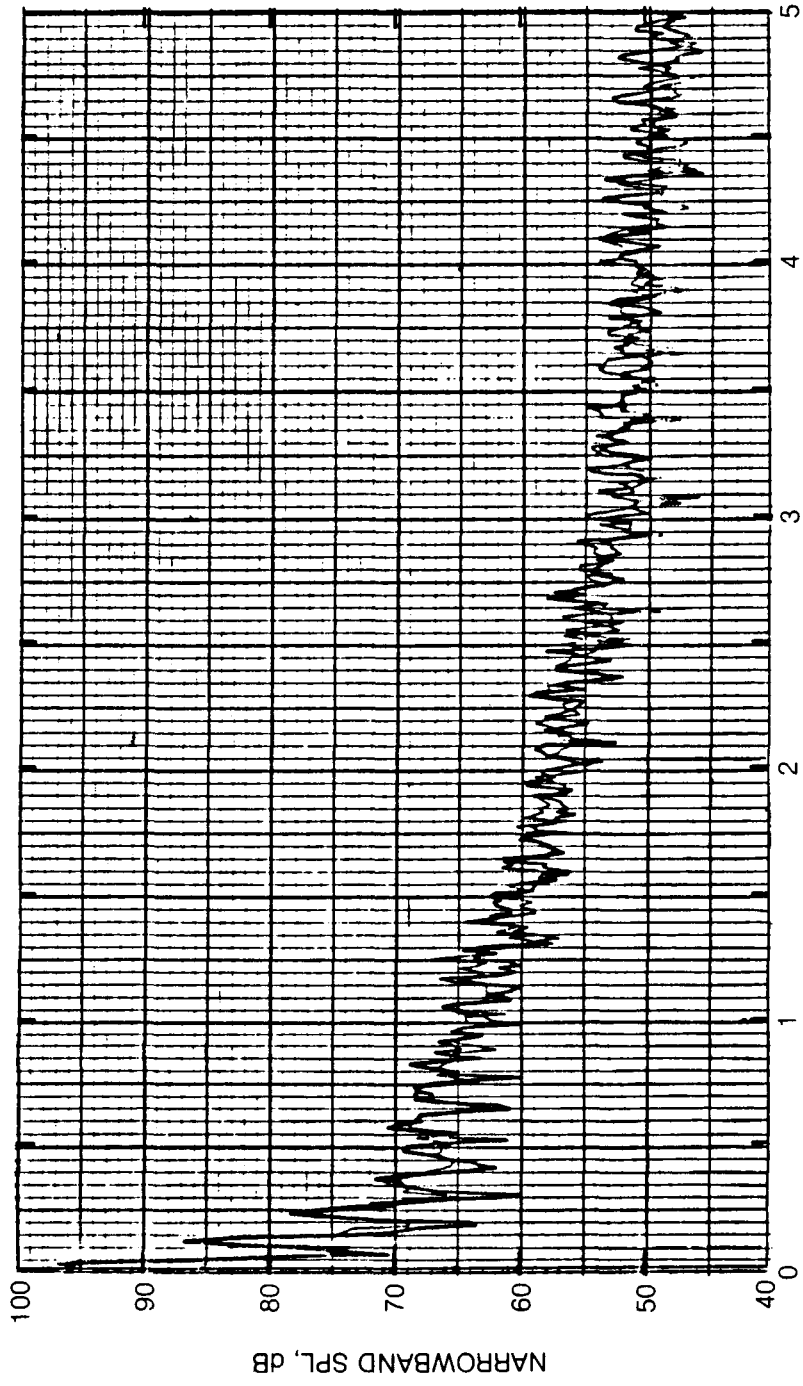

Figure 38 Narrowband Noise Spectrum Measured During Flyover at 72 m/sec, Bandwidth 12.5 Hz

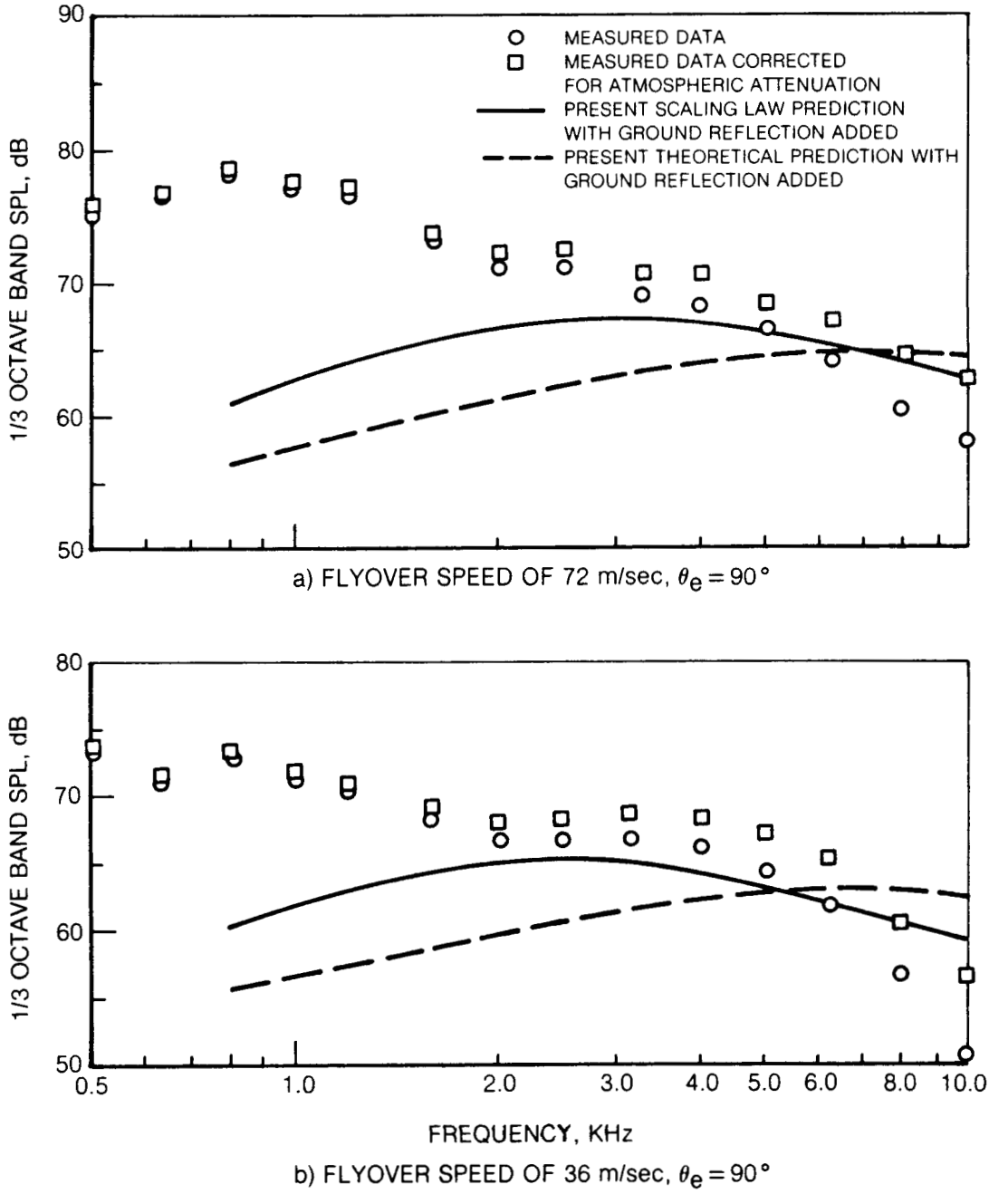

Figure 39 Comparison of Measured 1/3 Octave Band Helicopter Flyover Noise Spectrum and Predicted Trailing Edge Noise Spectrum

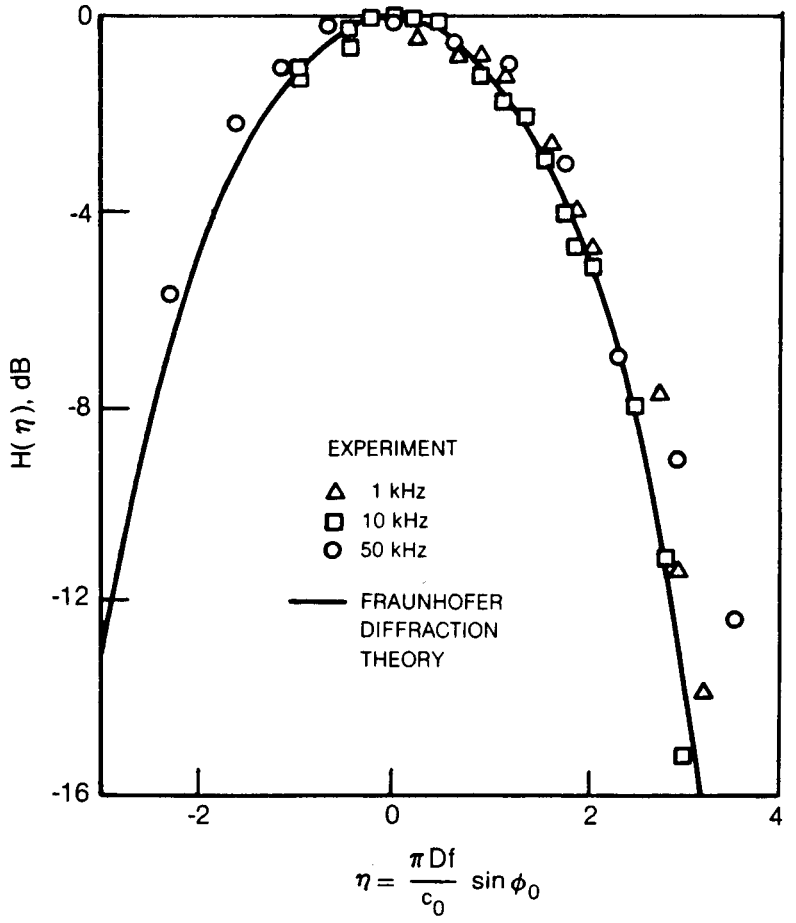

Figure 40 Diffraction Pattern of the Directional Microphone System for a Point Source of Sound at M = 0, R = 2.8m

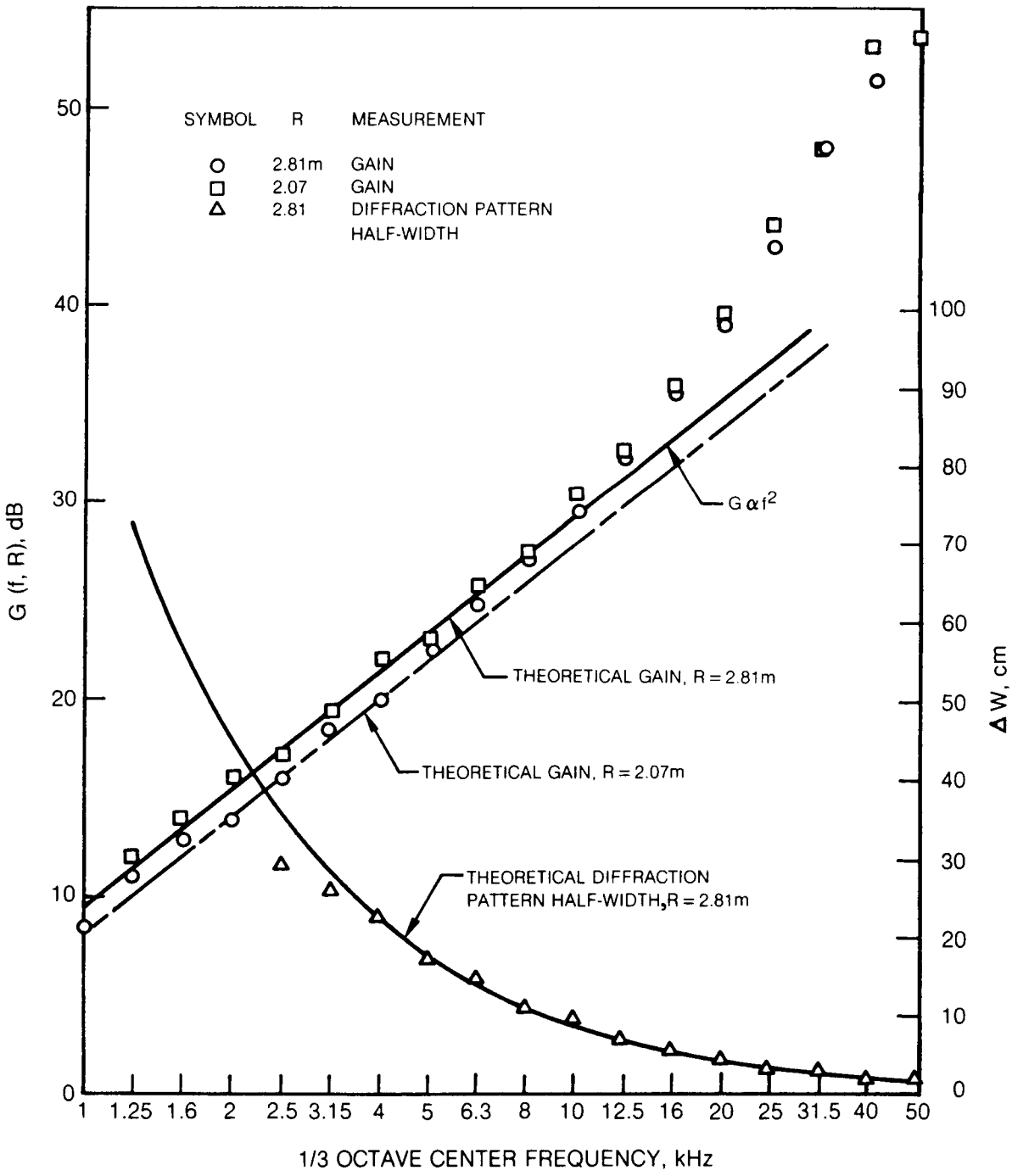

Figure 41 Gain and Diffraction Pattern Half-width of Directional Microphone System for a Point Source of Sound at M = 0

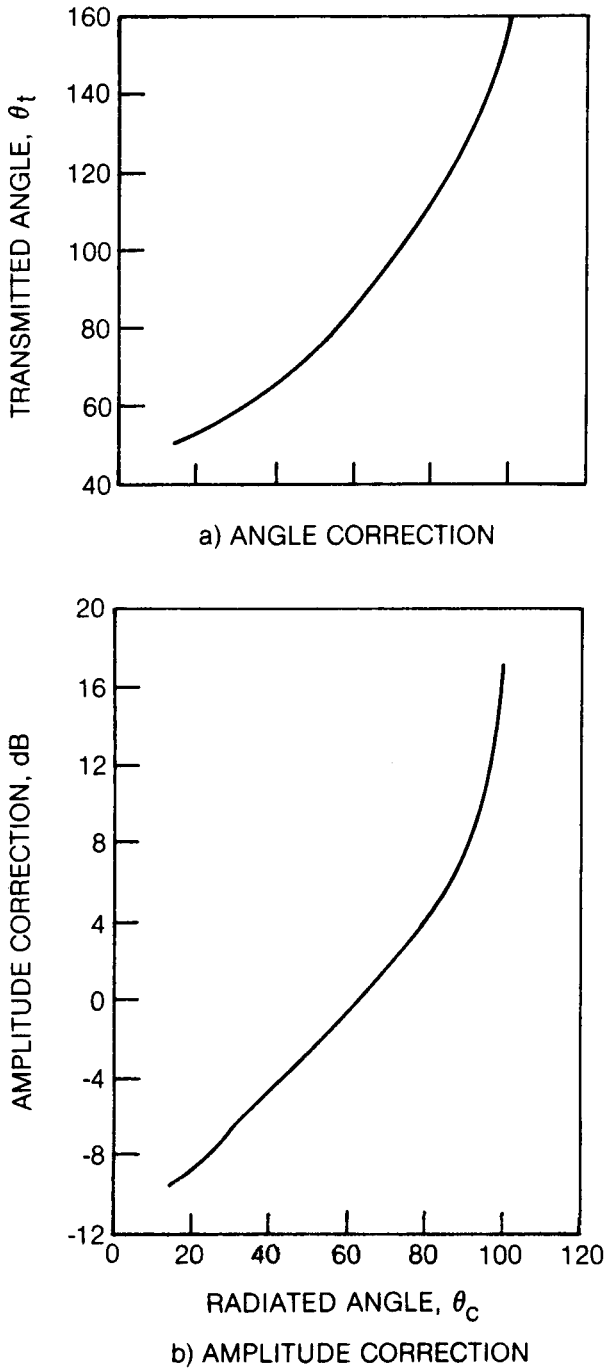

Figure 42 Refraction Angle and Amplitude Corrections, M = 0.5, Sideline Geometry, $h/y_1 = 0.14$

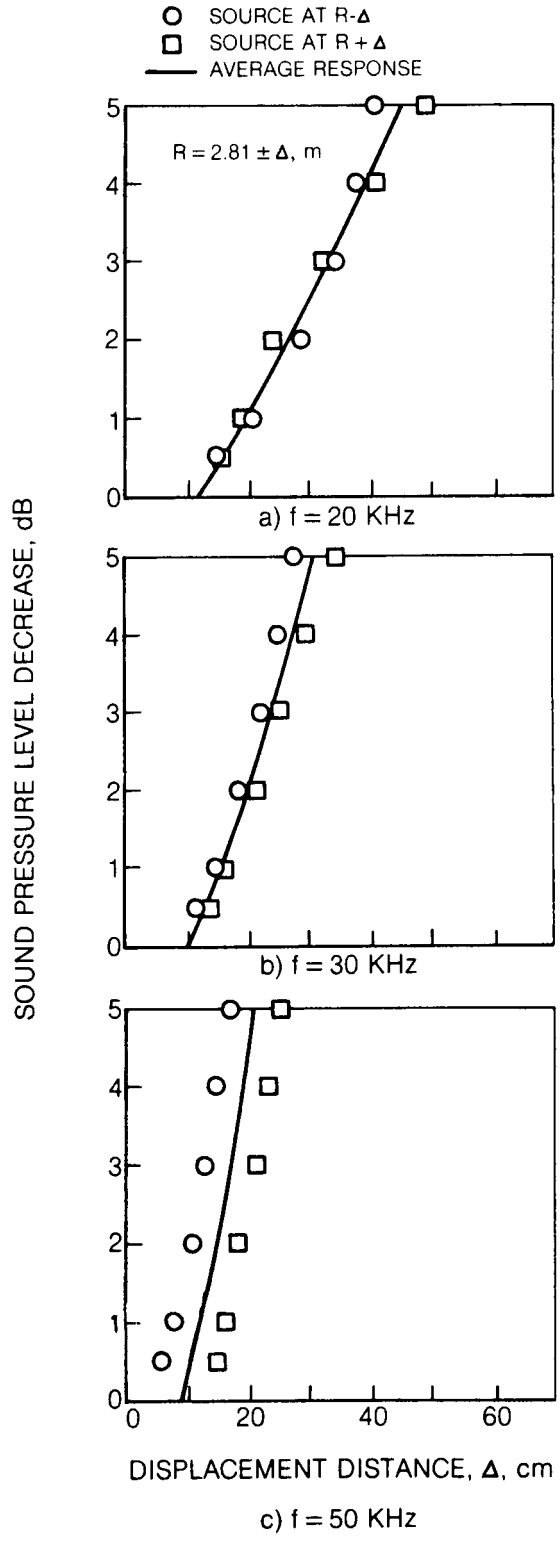

Figure 43 Directional Microphone Depth of Field Response to A Point Source of Sound at M = 0

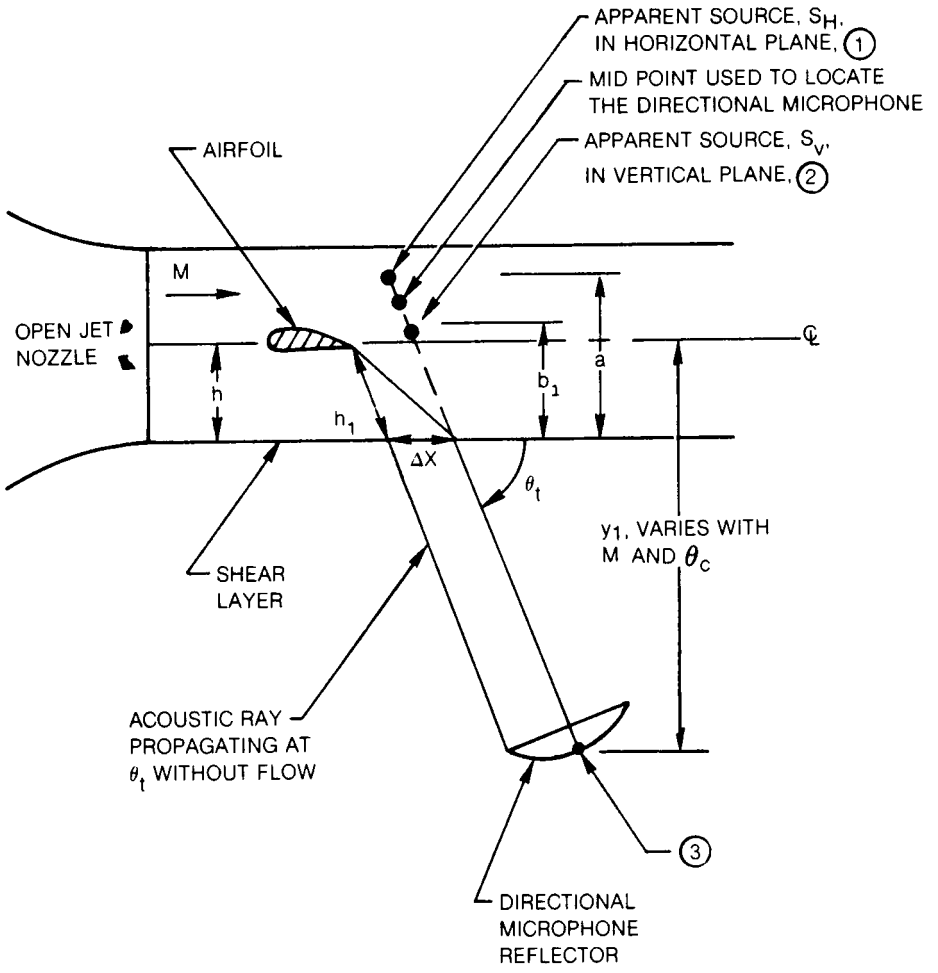

$$\Delta R = R_{1,3} - R_{2,3}$$

$$R_{MID} = \frac{R_{1,3} + R_{2,3}}{2} = \begin{cases} 2.81\ m \\ OR \\ 2.07\ m \end{cases}$$

Figure 44 Locating the Directional Microphone Reflector to Account for the Apparent Source Position

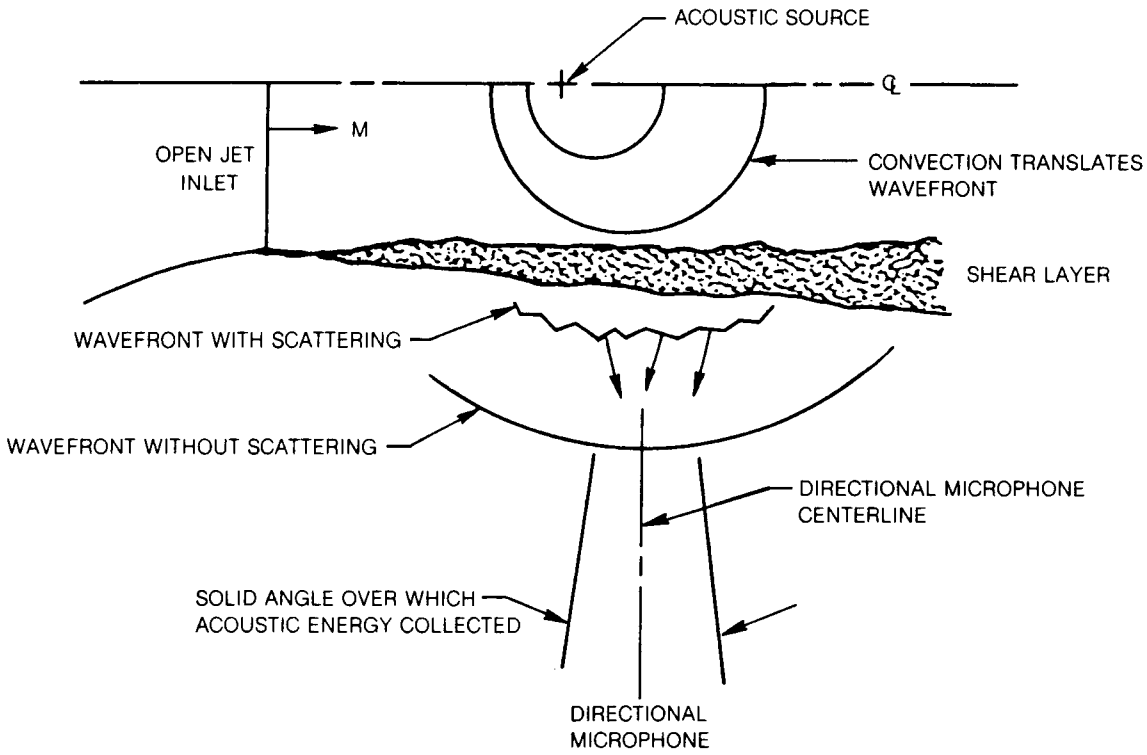

Figure 45 Physics of Scattering

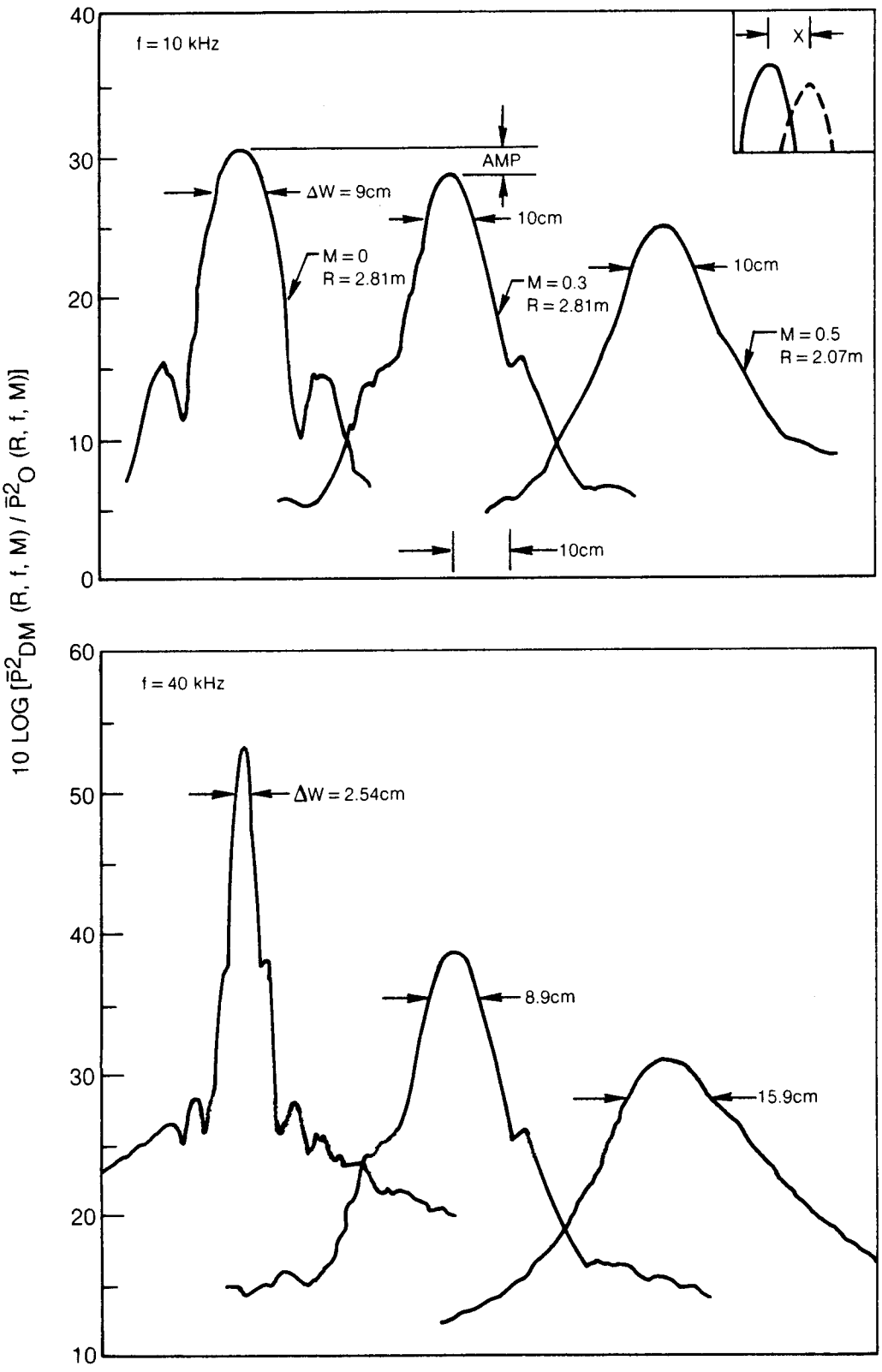

Figure 46 Variation of Acoustic Source Diffraction Pattern with Open Jet Mach Number, $\theta_c = 90°$

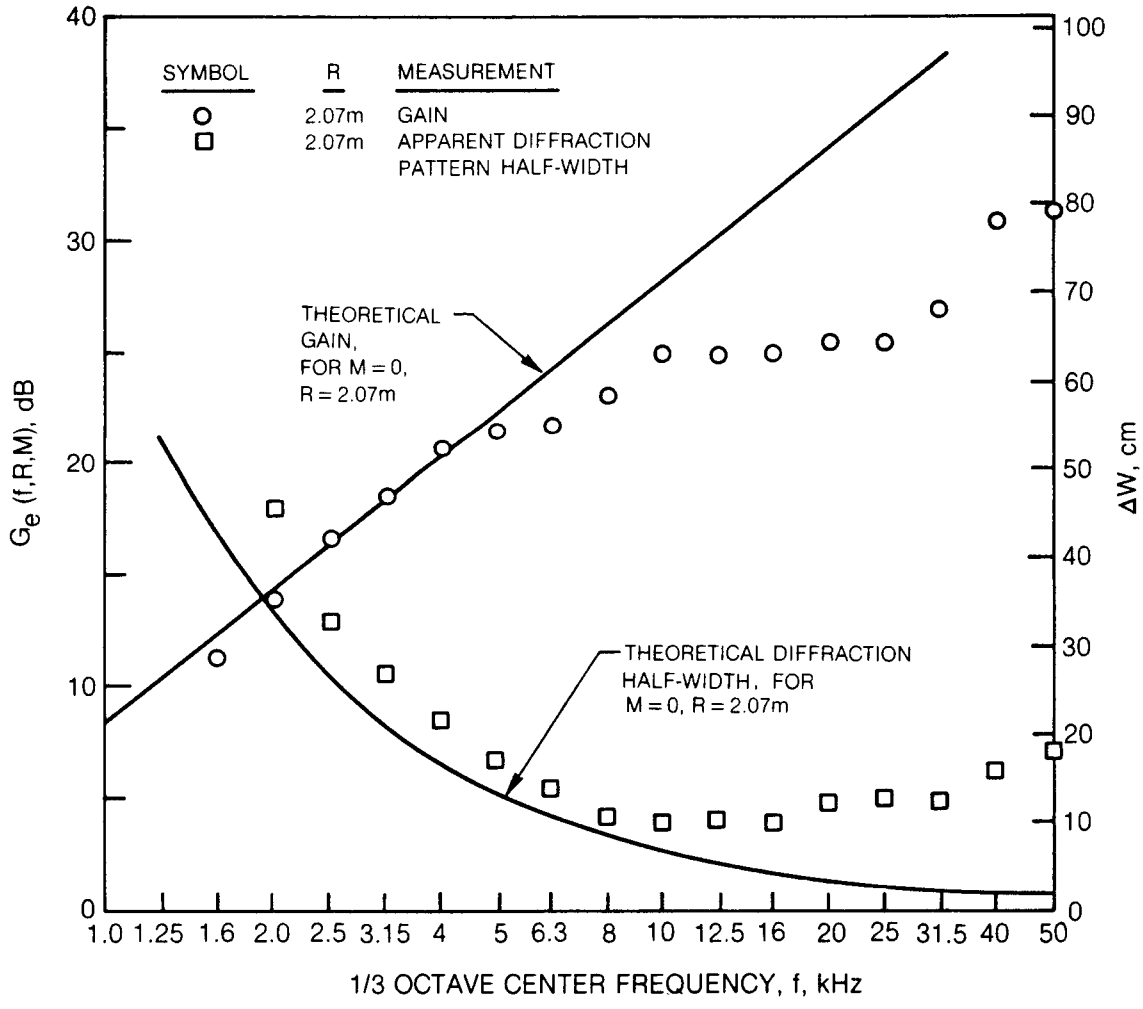

Figure 47 Gain and Apparent Diffraction Pattern Half-width of Directional Microphone System, M = 0.5, $\theta_c = 90°$

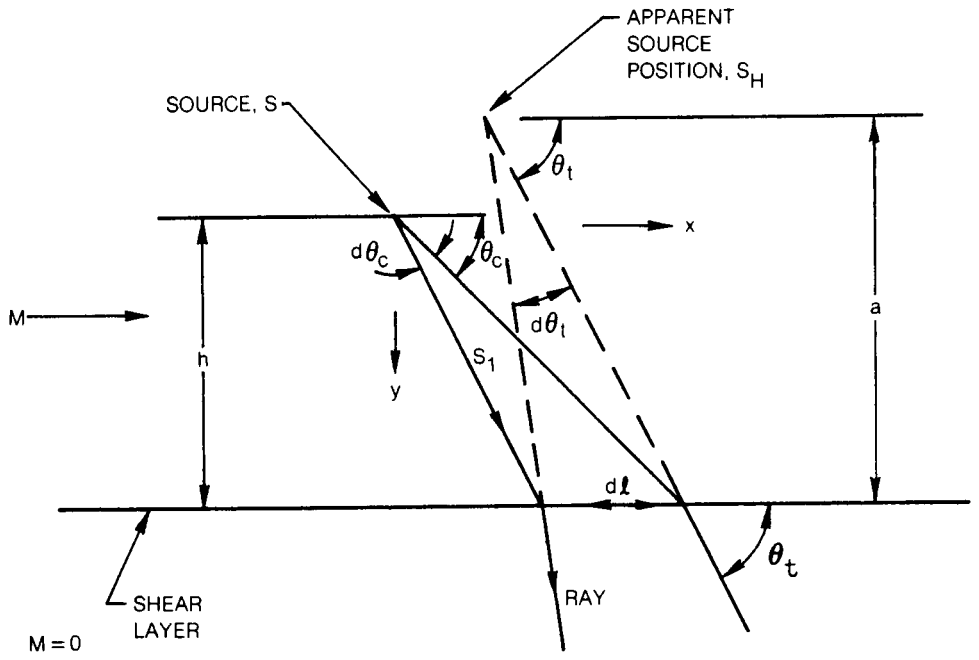

a) APPARENT SOURCE POSITION IN THE HORIZONTAL PLANE CONTAINING THE SHEAR LAYER NORMAL AND THE FLOW VECTOR

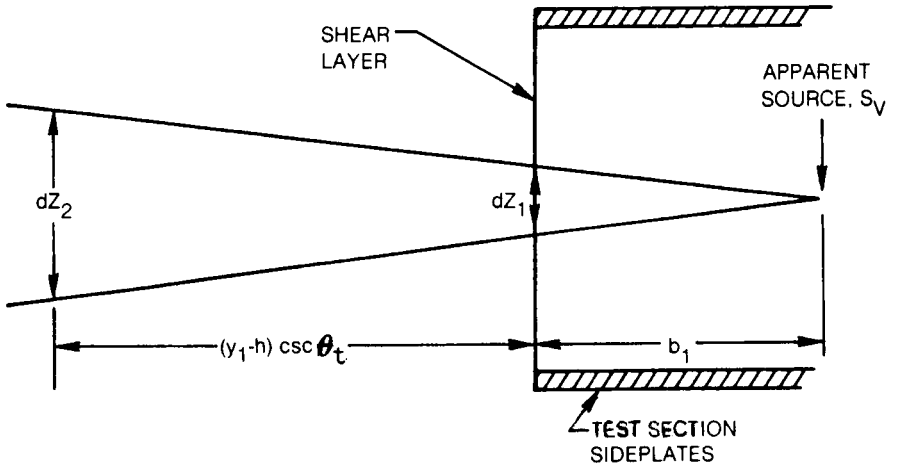

b) APPARENT SOURCE POSITION IN THE PLANE NORMAL TO THE X-Y PLANE AND AT AN ANGLE θ_t WITH THE SHEAR LAYER

Figure 48 Coordinates Defining Apparent Source Position

1. Report No.	2. Government Accession No.	3. Recipient's Catalog No.
NASA CR-3470		

4. Title and Subtitle	5. Report Date
HELICOPTER ROTOR TRAILING EDGE NOISE	November 1981
	6. Performing Organization Code

7. Author(s)	8. Performing Organization Report No.
Robert H. Schlinker and Roy K. Amiet	
	10. Work Unit No.

9. Performing Organization Name and Address	11. Contract or Grant No.
United Technologies Research Center East Hartford, CT 06108	NAS1-15730
	13. Type of Report and Period Covered
12. Sponsoring Agency Name and Address	Contractor Report
National Aeronautics and Space Administration Washington, D.C. 20546	14. Sponsoring Agency Code

15. Supplementary Notes

Langley Technical Monitor: Thomas F. Brooks
Final Report

16. Abstract An experimental and analytical study was conducted to assess the importance of trailing edge noise as a helicopter rotor broadband noise source. To isolate the noise mechanism a two-dimensional section of a helicopter main rotor blade was tested in an acoustic wind tunnel at close to full-scale Reynolds numbers to ensure realistic airfoil boundary layers. Boundary layer data and acoustic data were obtained for use in developing an acoustic scaling law and testing a first principles trailing edge noise theory.

Results obtained from the isolated airfoil study were extended to the rotating frame coordinate system to develop a helicopter rotor trailing edge noise prediction. Comparisons of the calculated noise levels with helicopter flyover spectra demonstrated that trailing edge noise contributes significantly to the total helicopter noise spectrum at high frequencies. This noise mechanism is expected to control the minimum rotor noise.

In the case of noise radiation from a local blade segment, the acoustic directivity pattern is predicted by the first principles trailing edge noise theory. Noise dependence on local section Mach number varies as Mach number to the fifth power. Directivity is independent of angle of attack and Strouhal number. Acoustic spectra are predicted by a scaling law which includes Mach number, boundary layer thickness and observer position. Spectrum shape and sound pressure level are also predicted by the first principles theory but the analysis does not predict the Strouhal value identifying the spectrum peak. Accurate predictions require using measured surface pressure data obtained near the airfoil trailing edge.

17. Key Words (Suggested by Author(s))	18. Distribution Statement
Helicopter Rotor Noise Trailing Edge Noise Boundary Layer Noise Rotor Noise Blade Noise	Noise Unclassified - Unlimited Subject Category 71

19. Security Classif. (of this report)	20. Security Classif. (of this page)	21. No. of Pages	22. Price
Unclassified	Unclassified	148	A07

For sale by the National Technical Information Service, Springfield, Virginia 22161

NASA-Langley, 1981